Observational Studies for Dynamical and Collisional Evolutions of Small Solar System Bodies

Terai, Tsuyoshi

(Degree)
博士（理学）

(Date of Degree)
2011-03-25

(Date of Publication)
2011-09-30

(Resource Type)
doctoral thesis

(Report Number)
甲5180

(URL)
https://hdl.handle.net/20.500.14094/D1005180

Doctoral Dissertation

Observational Studies for Dynamical and Collisional Evolutions of Small Solar System Bodies

January 2011

Graduate School of Science, Kobe University

Tsuyoshi TERAI

ABSTRACT

Small bodies in the Solar system are survivors from the planetary formation phase. However, they are not absolutely primordial objects but experienced some degree of dynamical, collisional, and compositional evolutions. Our interests are the origins and evolutions of the small bodies. They give us meaningful informations to understand the history of our Solar system. This thesis consists of two parts.

In Part I, we investigated the size distribution of main-belt asteroids (MBAs) with high-inclination to explore asteroid collisional evolution under hypervelocity collisions of around 10 km s^{-1}. We performed a wide-field survey for high-inclination sub-km MBAs using the 8.2-m Subaru Telescope with the Subaru Prime Focus Camera (Suprime-Cam). Suprime-Cam archival data were also used. A total of 616 MBA candidates were detected in an area of 9.0 deg^2 with a limiting magnitude of 24.0 mag in the SDSS r filter. Most of candidate diameters were estimated to be smaller than 1 km.

We found a scarcity of sub-km MBAs with high inclination. Cumulative size distributions (CSDs) were constructed using Subaru data and published asteroid catalogs. The power-law indexes of the CSDs were 2.17 $\pm$ 0.02 for low-inclination ($< 15°$) MBAs and 2.02 $\pm$ 0.03 for high-inclination ($> 15°$) MBAs in the 0.7–50 km diameter range. The high-inclination MBAs had a shallower CSD. We also found that the CSD of S-like MBAs had a small slope with high inclination, whereas the slope did not vary with inclination in the C-like group. The most probable cause of the shallow CSD of the high-inclination S-like MBAs is the large power-law index in the diameter–impact strength curve in hypervelocity collisions. The collisional evolution of MBAs may have advanced with oligopolistic survival during the dynamical excitation phase in the final stage of planet formation.

In Part II, we investigated the dynamical and surface evolutions of irregular satellites of Uranus. We performed wide-field photometric observations

for Uranian irregular satellites using the 8.2-m Subaru Telescope with the Suprime-Cam. The collected data contained seven irregular satellites: Caliban, Sycorax, Prospero, Setebos, Stephano, Trinculo, and Francisco. As the result of data reduction with the color and airmass corrections, the significant brightness variations were confirmed for four objects. We carried out the period analyses and found the periods of brightness variations (corresponding to a half of the rotation period) 5.4 hr or 7.0 hr for Caliban, 3.5 hr for Sycorax, 4.6 hr or 5.9 hr for Prospero, and 2–15 hr for Stephano. Their rotational period-diameter distribution is consistent with that of asteroids and trans-Neptunian objects (TNOs).

Sycorax and Prospero showed clear lightcurves in all of the observation nights enough to measure the slopes of the lightcurves around 1° phase angle. The surge slopes were determined as 0.03 mag deg^{-1} for Sycorax and 0.14 ± 0.03 mag deg^{-1} for Prospero. It is interesting that they have distinct difference of surge slope, indicating heterogeneity of surface properties between them. We also obtained the data of the surge slope and $B-V$ color for TNOs, Centaurs, Jovian Trojans (JTs), asteroids, and regular satellites.

Comparison of the surge slope distributions between the irregular satellites and the other populations indicates that Sycorax's surge is similar to those of Centaurs, JTs, and regular satellites. It also agreed with that of high-inclination (larger than 15°) Centaurs. Prospero has a surge slope consistent with low-inclination Centaurs and high-inclination TNOs. The results indicate that Sycorax was a captured body from the local planetesimals, while Prospero was derived from the region interior to Uranus's orbit, probably the Jupiter–Saturn zone.

Contents

Part I

A WIDE-FIELD SURVEY FOR SMALL MAIN-BELT ASTEROIDS WITH HIGH INCLINATION

1 Introduction

Our solar system is constructed from a protoplanetary disk consisting of nebular gas and dust particles. The dust particles aggregated and grew to km-size or larger bodies called planetesimals. The formation of the terrestrial planets resulted from accretion of mostly rocky planetesimals, whereas the giant planets were formed from icy planetesimals outside the snow line at 2.7 AU (Hayashi, 1981). The small solar system bodies (SSSBs) are remnants of planetesimals which did not merge to form planets or were not ejected from the solar system. They include a variety of meaningful information about the processes of planet formation. But all of the SSSBs are not truly primitive. Their orbit, size, structure, and composition suffered some alteration. Investigation of the SSSB evolution reveals the planetesimal growth.

The largest group of the SSSB populations is main-belt asteroids (MBAs) located in heliocentric distance of 2.1–3.3 AU. The number of known MBAs is more than 500,000[1], enabling statistical studies through the orbital, size, and taxonomic distributions.

The origin of almost all MBAs is likely to be collisional fractions of rocky planetesimals in the inside region of the Jupiter orbit, though a portion of MBAs could be delivered trans-Neptunian objects (Levison et al., 2009)

The collisional history of MBAs is a critical clue to estimate the initial size distribution of planetesimals in the inner solar system and to trace how terrestrial planets have grown. In addition, it gives a constraint the formation timescale of giant planets because the collisionally-fragmentation evolution of planetesimals was triggered by the Jupiter formation (Bottke et al., 2005a,b).

1.1 Collisional Evolution of Main-belt Asteroids

The size distribution of MBAs is the most fundamental information to investigate their collisional evolution. Several extensive asteroid survey with optical telescopes, such as Palomar-Leiden Surveys (PLS; van Houten et al.,

[1]IAU Minor Planet Center ⟨http://minorplanetcenter.org/iau/mpc.html⟩

1984), Spacewatch Survey (Jedicke & Metcalfe, 1996), and Sloan Digital Sky Survey (SDSS; Ivezić et al., 2001), provided the MBA size distributions down to a few km in diameter. For large asteroids down to $\sim$ 30 km, the size distribution was precisely obtained from the IRAS (Infrared Astronomical Satellite) data (Cellino et al., 1991). On the other hand, the shape of size distribution for small asteroids in $\sim$ 1 km diameter or less was estimated by the survey observations with the SDSS (Ivezić et al., 2001), Hubble Space Telescope (HST; Evans et al., 1998), the 3.6-m Canada-France-Hawaii Telescope (CFHT; Wiegert et al., 2007), the 3.8-m Mayall Telescope in the Sub-Kilometer Asteroid Diameter Survey (SKADS; Gladman et al., 2009), and the 8.2-m Subaru Telescope in the Subaru Main-Belt Asteroids Survey (SMBAS; Yoshida et al., 2003; Yoshida & Nakamura, 2007).

Dohnanyi (1969) showed the collisional evolution model with asteroids population in collisional equilibrium that all bodies have the same collisional response parameters. It results the steady-state size distribution expressed by a power-law equation

$$\mathrm{d}N = BD^{-3.5}\mathrm{d}D, \tag{1.1}$$

where D is the diameter, N is the number of bodies, and B is a constant. But the average power-law index of the MBA size distribution derived from the previous observations is shallower than the above equation. Furthermore, the size distribution is not a single power-law but it has a 'wavy' structure with two bumps near $D \sim 100$ km and $D \sim 5$ km. The numerical simulations in Davis (1994) showed that the shape and slope of the MBA size distribution is determined from a scaling law of asteroid strength. The strength is defined by threshold energy per unit mass required catastrophic disruption. It increases with asteroid size for bodies larger than $D \sim 100$ m in the gravity scaled regime. In contrast, it decreases with size for small bodies in the strength scaled regime. These relationships of the size-dependent strength causes the shallow and wavy size distribution of MBAs. This means that the scaling law of the asteroid strength is a critical factor for collisional evolution of planetesimals/asteroids.

Several models for collisional and orbital evolutions of MBAs suggest a dynamical excitation event at the final stage of the planet formation (Petit et al., 2002). This event produced several features seen in the current main belt, such as a high eccentricity/inclination asteroid population and the radial mixing of taxonomic classes. The dynamical excitation also ejected most asteroids out of the main belt, depleting more than 99% of the primordial mass (Bottke et al., 2005b). The relative velocities among asteroids were elevated during this phase. In the main belt, asteroid collisions mostly occurred at higher velocities than the present average velocity of $\sim$4 km s^{-1} (Vedder et al., 1998). The relative velocity between a body in the remnant main belt population and one in the ejected population from the main belt zone exceeded 10 km s^{-1} (Bottke et al., 2005b). However, the fragment size distribution and ejecta velocities of such high-velocity collisions are still unclear; reproduction by laboratory experiments is difficult.

In our approach to this problem, we focus on MBAs with high inclination. The mean relative velocity of highly-inclined MBAs can be as large as $\sim$10 km s^{-1} (Gil-Hutton, 2006). Comparing the size distributions between low-inclination (low-i) and high-inclination (high-i) MBAs could provide meaningful insight into disruptions at high velocity. For investigating high-i MBAs, several published asteroid catalogs are available, but their detection limits are no smaller than kilometer size. We performed observations for sub-km high-i MBAs to obtain their size distribution.

2 Observations

2.1 Strategies

The inclination distribution of the known MBA population drops steeply at $i \sim 15°$, where i is the inclination. The scarcity of high-i MBAs is due not only to the small numbers but also to an observational bias. Most previous MBA surveys have searched intensively around the ecliptic, but high-i MBAs only pass through the ecliptic plane briefly, spending most of their time in high ecliptic latitudes. High-i bodies are more likely to be found at $\beta_{\rm h} \sim i$ where $\beta_{\rm h}$ is the heliocentric ecliptic latitude than at low ecliptic latitudes ($\beta_{\rm h} < i$). We surveyed high ecliptic latitudes to detect high-i MBAs.

Ivezić et al. (2001) showed that the surface density of asteroids in $\beta \sim \pm 20°$ is only $\sim$10 % of that in $\beta \sim 0°$, where β is the geocentric ecliptic latitude (a factor of 1.5–2 smaller than $\beta_{\rm h}$ at opposition for MBAs). To find a number of high-i MBAs, a wide-field survey is indispensable. We performed a wide-field survey for faint MBAs using data derived from the 8.2-m Subaru Telescope. In addition, efficient observation is necessary to collect large amounts of data within a limited amount of time. We adopted a less usual procedure, observing each field only two times with an interval of about 20 minutes. Terai et al. (2007) developed a new reduction technique to find asteroids efficiently in such two-visit observation data sets.

2.2 Observations

Observations were conducted on June 3 2008 (UT) with the Subaru Telescope at the summit of Mauna Kea in Hawaii. We used the Subaru Prime Focus Camera (Suprime-Cam), a mosaic camera of ten CCD chips. It covers a $34' \times 27'$ field-of-view with a pixel scale of $0.20''$ and has a high sensitivity of $R_c = 25.6$ mag in 5-minutes integration for a point source (Miyazaki et al., 2002). The observational fields are near R.A.(J2000) = $16^{\rm h}59^{\rm m}$, Dec.(J2000) = $+02°26'$ corresponding to $\beta \sim 25°$ at opposition. We selected 22 fields with no bright stars, two of which were located on the Sloan Digital Sky Sur-

vey (SDSS) fields. Several stars cataloged in the SDSS database[2] were used for photometric calibration. All data were acquired with the SDSS r-band filter (Fukugita et al., 1996). The exposure time was 4 minutes. Each field was taken twice with an interval of about 20 minutes. The total observed area of the sky was $\sim$5.6 deg^2 in 4 hours. The typical seeing size was 0.6 arcsec. The detection limit range was $r = 23.8$–24.2 mag for moving objects whose motion corresponded to MBAs (see Section 4.2). We used data with a limiting magnitude of $r = 24.0$ mag. The available data includes 14 fields, 3.6 deg^2 (Table 1.1).

2.3 Archival Data

We also used archival Suprime-Cam data obtained from the Subaru-Mitaka-Okayama-Kiso Archive, SMOKA[3] (Baba et al., 2002), consisting of R_c-band data with a detection limit of $R_c \geq 23.8$ mag for moving objects (Section 4.2). The selected data were taken where the ecliptic latitudes with respect to opposition were within $\pm 15°$, allowing reasonably accurate orbital estimations from the short arcs. We avoided star crowding regions around the galactic plane. Each field was taken at least twice, at intervals of 5 minutes to 1 hour. We searched a total of 28 fields (Table 1.2).

[2]Sloan Digital Sky Survey⟨http://www.sdss.org/⟩.
[3]The SMOKA is operated by the Astronomy Data Center, NAOJ.

3 Data Reduction

The images were processed chip-by-chip using IRAF produced by the National Optical Astronomy Observatories (NOAO). The raw data were reduced with standard processes consisting of bias subtraction, flat-fielding, sky subtraction, distortion correction, and positional correction. We also used SDFRED, the software package for Suprime-Cam data reduction (Yagi et al. 2002, Ouchi et al. 2004) to subtract the sky background and correct for geometric distortion.

Detecting a moving object from two-visit data is a three-step procedure: (i) masking fixed stars and galaxies in the field, (ii) detecting the remaining sources from the processed images, and (iii) removing non-object sources such as cosmic rays. First, the fixed objects were masked with the image-processing technique developed by Terai et al. (2007). Two types of composite images were made from raw images: one excluding smaller values of each pixel ("OR" image) and one excluding larger values of each pixel ("AND" image). The OR image included all objects in either of the raw images, whereas the AND image consisted of only fixed objects. The AND image was used to make a mask image whose pixel values were replaced with 0 for light sources and 1 for background. This was multiplied by the OR image to mask the fixed objects such as stars and galaxies. A moving object was recognized as a pair of light sources in the final processed image (see Figure 1.1).

The residual sources were detected with the SExtractor software (Bertin & Arnouts, 1996). The detection threshold was set to 2σ, where σ is the root-mean-square value of the background. But a large number of false sources were also identified. Most were discriminated using criteria such a sharpness of the point spread function (PSF), velocity of motion, and direction of motion. An object pair that fulfils all of these criteria is considered a moving object candidate. Finally, each candidate was inspected visually to determine whether or not it was in fact a moving object.

4 Results

4.1 Detection

We searched for moving objects in our observation data of 14 fields and the archival data of 28 fields. In the total area of 9.0 deg^2, 656 moving objects were detected. The apparent motion of each object was measured from the shift in position between two images. Figure 1.2 shows the apparent motion distribution of the detected objects. Most of the objects have motion of ∼30–40 arcsec hr^{-1} along the ecliptic longitude, corresponding to MBAs. The smallest motion rate was 3 arcsec hr^{-1}, equivalent to a trans-Neptunian object, and the largest was 107 arcsec hr^{-1}. Highly inclined asteroids exhibited large motions in both the ecliptic longitude and latitude.

4.2 Photometry

The flux of each moving object was measured from the total intensity of pixels within a non-circular aperture. We used a capsule-shaped aperture given by a trail of a circle with the triple-FWHM (full width at half maximum) diameter in length of the motion during the exposure time. The apparent magnitude of an asteroid was estimated from the mean flux in the two images. Flux calibration was conducted using several stars listed in the SDSS database for our observation r-band data and in the Landolt standard stars for the archival R_c-band data. The limiting magnitude for moving objects was evaluated by artificial trails added to the raw images. They were made by imbricate pseudo point sources with the same FWHM of stars in the image. We used 100 artificial trails with brightness steps of 0.1 mag. We regarded the brightness corresponding to detection probability of 80 % as the limiting magnitude, which for our observational data was $r = 24.0$ mag. This was transformed to 23.8 mag for the R_c-band (Fukugita et al., 1996). We used the archival data when its limiting magnitude was larger than $R_c = 23.8$ mag. Within the limiting magnitude, the photometric error was less than 0.1 mag.

4.3 Orbital Estimations

To determine the orbit of an asteroid, we need at least three observations at different epochs. In this study, we could not obtain precise orbits for the detected moving objects because we observed a field only twice in a short arc of several dozen minutes. Instead, we assumed a circular orbit. This enabled us to estimate the semi-major axis and inclination of a moving object from its sky motion (Bowell et al. 1990, Nakamura & Yoshida 2002). These elements were calculated using the equations for geocentric motion rate of a moving object presented by Jedicke (1996) with an eccentricity of zero. An object was excluded as an inaccurate orbit if its inclination was calculated to be larger than 40° (9 objects).

We examined the estimation accuracy using the Monte Carlo simulations in Nakamura and Yoshida (2002). We generated 10,000 pseudo-MBAs with randomly distributed orbital elements. The ranges of their semi-major axes (a), eccentricities (e), and inclinations (i) were a =2.1–3.3 AU, e =0.0–0.4, and i =0°–30°, respectively. The eccentricity of each orbit was given with a probability based on the actual eccentricity distribution of known MBAs. The true anomaly was set with a probability following Kepler's second law. The apparent velocity of motion was calculated for a hypothetical observation field from the formulae in Jedicke (1996). Then, we estimated the semi-major axis and inclination assuming a circular orbit from the velocity of motion.

The accuracy of each element was represented by the standard deviations of differences between the estimated value and the given value. If the separation from opposition in ecliptic longitude was less than 15°, the semi-major axis error was ∼0.1–0.15 AU for a semi-major axis range of 2.5–3.3 AU. The error was larger than 0.15 AU for semi-major axes between 2.0–2.5 AU. The inclination accuracy depends strongly on inclination. Nakamura and Yoshida (2002) mentioned the degradation in inclination accuracy for $i > 10°$ (the random error of inclination is more than 5°). However, accuracy is improved in high ecliptic latitudes. The inclination error is 3°–4° at $\beta \sim 25°$ where most high-i MBAs were detected. This is small enough to obtain precise size

distributions for low-i and high-i MBAs.

The semi-major axis distribution of the detected moving objects is shown in Figure 1.3(a). The distribution is concentrated between 2.0−3.3 AU, similar to what is known for in the main belt. We regarded 616 objects within this zone as the MBA sample. The semi-major axis distribution of the sample with $a > 2.5$ AU was similar to the actual population, which had a local minimum at 2.8 AU and an outer edge at 3.3 AU, corresponding to the 5:2 and 2:1 mean-motion resonances (MMR) with Jupiter, respectively. In contrast, the distribution in $a < 2.5$ AU did not appear to replicate the known distribution well.

The inclination distribution is shown in Figure 1.3(b). The two local peaks at ∼10° and ∼16° are quite different from the known distribution in the main belt. This is because many of the surveyed fields are situated at geocentric ecliptic latitudes (β) of 11°, 17°, and 25°, corresponding to $\beta_{\rm h} \sim$ 7°, 11°, and 16°, respectively. This means that the highest probability MBA detections occur at inclinations of around 7°, 11°, and 16° (see Section 2.1).

The distribution of semi-major axis vs. inclination is plotted in Figure 1.4. Most bodies were located between the secular resonance ν_6 and the 2:1 MMR, which agrees with the distribution of known MBAs.

4.4 Diameter Estimations

The absolute magnitude of an asteroid is defined as the brightness observed at a hypothetical location of $r = 1$ AU and $\Delta = 1$ AU with the Sun, the asteroid, and Earth in a straight line. It is given by

$$H = m - 5\log(r \cdot \Delta) - P(\alpha), \tag{1.2}$$

where H is the absolute magnitude and m is the apparent magnitude in a given wavelength band. The apparent magnitude is reduced by the phase angle α, the Sun-asteroid-Earth angle following the phase function given by

$$P(\alpha) = (1 - G)\Phi_1(\alpha) + G\Phi_2(\alpha), \tag{1.3}$$

where G represents the gradient of the phase function (Bowell et al., 1989). We used $G = 0.15$, which is generally used for asteroids with unknown taxonomic types. $\Phi_1(\alpha)$ and $\Phi_2(\alpha)$ are given by

$$\Phi_i = \left[-A_i \left(\tan \frac{1}{2}\alpha \right)^{B_i} \right] \quad (i = 1, 2)\,, \tag{1.4}$$

where $A_1 = 3.33$, $A_2 = 1.87$, $B_1 = 0.63$, and $B_2 = 1.22$ (Bowell et al., 1989). Although these are V-band values, we applied them to r- and R_c-band data.

The relationship between absolute magnitude and diameter (D) is described by

$$H = m_\odot - 5 \log \frac{\sqrt{p} D/2}{(1 \text{ AU})}, \tag{1.5}$$

where $m_\odot$ is the apparent magnitude of the Sun, -27.29 mag in the R_c-band (Drilling & Landolt, 2000). This corresponds to -27.07 mag in the r-band, derived from the color transformation equations in Fukugita et al. (1996). Albedo is represented by p, which cannot be determined in this survey. Therefore, we used typical albedo values.

Asteroids have different albedos among the taxonomic groups. In photometric observation studies, asteroids are divided into two major groups, S-like and C-like asteroids (Yoshida & Nakamura, 2007). We estimated the mean albedos of S-like and C-like MBAs from the albedo catalog presented by the IRAS Minor Planet Survey and Supplemental IRAS Minor Planet Survey[4] (IMPS and SIMPS, respectively; Tedesco et al. 2002). The cataloged asteroids were classified into S-like and C-like groups according to the spectral database presented by the second phase of the Small Main-belt Asteroid Spectroscopic Survey[5] (SMASSII; Bus and Binzel 2002) and the Small

[4]Tedesco, E. F., P. V. Noah, M. Noah, and S. D. Price. IRAS Minor Planet Survey. IRAS-A-FPA-3-RDR-IMPS-V6.0. NASA Planetary Data System, 2004. ⟨http://sbn.psi.edu/pds/resource/imps.html⟩.

[5]Bus, S. and Binzel, R. P., Small Main-belt Asteroid Spectroscopic Survey, Phase II. EAR-A-I0028-4-SBN0001/SMASSII-V1.0. NASA Planetary Data System,2003. ⟨http://sbn.psi.edu/pds/resource/smass2.html⟩.

Solar System Objects Spectroscopic Survey[6] (S^3OS^2; Lazarro et al. 2004). The S-like asteroids include the S-complex and the minor classes including Ld-, D-, T-, V-, and O-types. The C-like asteroids consist of the C- and X-complexes. The mean value is $p_s = 0.19 \pm 0.09$ in the S-like asteroids (353 objects) and $p_c = 0.08 \pm 0.07$ in the C-like asteroids (649 objects).

The population ratio of S-like to C-like asteroids varies with heliocentric distance. Yoshida and Nakamura (2007) showed that the ratio for asteroids of $D > 0.6$ km are 1:1 in the inner belt (2.0–2.6 AU), 1:2.3 in the middle belt (2.6–3.0 AU), and 1:4 in the outer belt (3.0–3.5 AU). We estimated the mean albedo in each of the three zones from the population ratio and mean albedos of the S-like and C-like MBAs. We adopted the mean albedos as $(p_s+p_c)/(1+1) = 0.14$ for $2.0 < a < 2.6$ AU, $(p_s+2.3p_c)/(1+2.3) = 0.11$ for $2.6 < a < 3.0$ AU, and $(p_s+4p_c)/(1+4) = 0.10$ for $3.0 < a < 3.3$ AU. Although, as discussed in Section 5.2.2, the population of S-like MBAs is small in high inclination, the difference is negligible with respect to mean albedos. The absolute magnitude is converted to diameter using these albedo values and Eq. 1.5.

Figure 1.5 shows the diameter distribution for the detected MBAs. Most of the bodies were smaller than 1 km in diameter. Considering the photometric error of ∼0.1 mag and semi-major axis error of ∼0.1 AU, the inaccuracy of diameter estimation is about 15%. When the error on the albedo (∼0.06) is included, the added inaccuracy is 15%.

[6]Lazzaro, D., Angeli, C. A., Carvano, J. M., Mothe-Diniz, T., Duffard, R., and Florczak, M., Small Solar System Objects Spectroscopic Survey V1.0. EAR-A-I0052-8-S3OS2-V1.0. NASA Planetary Data System, 2006. ⟨http://sbn.psi.edu/pds/resource/s3os2.html⟩.

5 Discussion

5.1 Size Distributions

5.1.1 Size distribution of small MBAs

The detected MBA sample included some observational bias, which had to be removed. The most remarkable bias was a decrease in detection probabilities for faint objects. The limiting magnitude (24.0 mag in the r-band or 23.8 mag in the R_c-band) corresponded to $D = 0.7$ km at a semi-major axis of 3.3 AU with a typical phase angle of 25° and a typical albedo of 0.1. We regarded asteroids with $D > 0.7$ km as the sample for estimating size distribution.

In addition, we excluded asteroids with $a < 2.5$ AU for two reasons. First, this zone contains only a small population of high-i MBAs and S-like asteroids are abundant in this region, unlike in the outer zone. If these asteroids were included in the sample, the fraction of S-like asteroids would differ significantly from the low-i to high-i MBAs. S-like and C-like asteroid size distributions are supposed to differ (Ivezić et al. 2001, Yoshida & Nakamura 2007, Wiegert et al. 2007). An excess of S-like population in the low-i MBAs could cause a bias in comparing size distributions between low-i and high-i MBAs. This bias is discussed again in Section 5.2.2. Second, the estimated semi-major axis for an asteroid with $a < 2.5$ AU has a large error (>0.15 AU). Ultimately, 178 asteroids with $D > 0.7$ km were selected in $a = 2.5$–3.3 AU. The relationship between the sub-km asteroid population and inclination was examined with this unbiased sample.

Figure 1.6 shows the fractions of the sub-km asteroids for each inclination bin of 5°. The fractions are almost constant (∼0.4) between 0° and 15°, and significantly decrease beyond 15°. We found a population deficiency of sub-km MBAs with $i > 15°$.

Figure 1.7 shows the cumulative size distributions (CSDs) for the low-i sample with $i < 15°$ and high-i sample with $i > 15°$. Bin size is $\Delta \log D$[km] = 0.05, indicating the uncertainty of the diameter estimation. The CSD is

described by the power-law equation as

$$N(> D) \propto D^{-b}, \tag{1.6}$$

where $N(> D)$ is the cumulative number of asteroids larger than a diameter D and b is the power-law index of the CSD. The single power law was fit to each CSD with 0.7 km $< D <$ 2 km by the least squares method. The best-fit indexes of the CSDs were $b = 1.79 \pm 0.05$ for the low-i MBAs and $b = 1.62 \pm 0.07$ for the high-i MBAs.

We performed statistical tests to compare the two regressions. The regression lines are described by $y = y_0 - bx$, where $x = \log D$, $y = \log N(> D)$, and $y_0 = \log N(> 1\text{km})$. First, an F-test was used to check whether the two populations possessed homogeneous variances around the regression lines. We defined the null hypothesis as H_0: $\sigma_1^2 = \sigma_2^2$, against the alternate hypothesis as H_1: $\sigma_1^2 \neq \sigma_2^2$, where σ^2 is a residual variance and the suffix 1 and 2 stand for the low-i and high-i MBAs, respectively. The computed F-value was $\sigma_2^2/\sigma_1^2 = 2.00$ ($\sigma_1^2 < \sigma_2^2$). It is less than the critical value $F_{0.05}$=3.18. The test accepted that σ_1^2 and σ_2^2 were equal with the 0.05 level of significance.

Next, we performed a t-test with H_0: b_1=b_2 against H_1: $b_1 > b_2$. Let the population regression coefficient for b be normally distributed with mean b_i and variance $V_i\sigma_i^2$ where $V_i = 1/\Sigma(x - \overline{x}_i)^2$ and $\overline{x}_i$ is the mean of x_i (i=1,2). In the case of equal variances, we use the criterion

$$t = \frac{b_1 - b_2}{\sqrt{\frac{(\Sigma_1+\Sigma_2)(V_1+V_2)}{f_1+f_2}}}, \tag{1.7}$$

where Σ_1 and Σ_2 are sums of squares from the regression lines, derived from $\Sigma_i = \Sigma[y - (y_0 - b_i x)]^2$ (i=1,2), and f_1 and f_2 are degrees of freedom (Welch, 1938). The t-value for this test was calculated to be t=1.99. It is greater than the critical value $t_{0.05}$=1.76 with 14 degree of freedom. We rejected the null hypothesis and accepted $b_1 > b_2$ at the 0.05 level of significance. In conclusion, for asteroids of at least 1 km in diameter, the high-i MBAs had a shallower CSD than the low-i MBAs at the 95% confidence level.

5.1.2 Size distribution of large MBAs

We used the published asteroid catalogs to obtain the size distribution of MBAs larger than those detected in the Subaru data. The CSDs for $D > 10$ km were constructed using the Asteroid Orbital Elements Database (ASTORB)[7] distributed by Lowell Observatory (Bowell, 2001). In addition, the SDSS Moving Object Catalog[8] (SDSS MOC; Ivezić et al. 2002) was used for diameter in the 2–10 km range to link the CSDs based on the Subaru and ASTORB data.

The ASTORB lists the orbital parameters and absolute magnitudes of more than 457,000 MBAs. We regarded 453,439 asteroids as MBAs for which the semi-major axis was between 2.1 AU and 3.3 AU, the perihelion was larger than 1.66 AU, and the aphelion was smaller than 4.61 AU (Bottke et al., 2002). The diameter and albedo of 2228 MBAs were measured by IRAS observations in the IMPS/SIMPS surveys (Tedesco et al., 2002). They cover almost all MBAs with $D > 35$ km. For MBAs of unknown albedo, the mean albedos deduced in Section 4.4 were used to estimate diameters. Figure 1.8(a) shows the absolute magnitude distribution and CSD of the MBAs in the ASTORB. Although the detection limit was never determined because the asteroids were found by several surveys with various limiting magnitudes, it appears to be a little under 10 km in diameter as seen in the absolute magnitude distribution.

For km-size asteroids, the SDSS MOC was employed. This lists the astrometric and photometric data for moving objects brighter than 21.5 mag in the r-band. The fourth released version of SDSS MOC consists of 470,000 moving objects observed up to March 2007. The orbital elements of most SDSS MOC asteroids have not been determined. The semi-major axis and inclination of each moving object in the SDSS MOC were estimated from apparent motions assuming a circular orbit, as in the analysis of the Subaru data (see Section 4.3). For estimation accuracy, we used only objects with a

[7] ⟨http://www.naic.edu/~nolan/astorb.html⟩.
[8] ⟨http://www.astro.washington.edu/users/ivezic/sdssmoc/sdssmoc.html⟩.

phase angle smaller than 15°. A total of 130,000 objects located in 2.0–3.3 AU in the semi-major axis were defined as MBAs.

The diameter and albedo of each SDSS MOC asteroid are also unknown. The apparent magnitudes of the moving objects were measured almost simultaneously in five bands (u, g, r, i, and z). Ivezić et al. (2001) defined a color index a^* using $g-r$ and $r-i$ colors as

$$a^* \equiv 0.89(g-r) + 0.45(r-i) - 0.57 \tag{1.8}$$

to divide asteroids into two major groups, "red" asteroids with $a^* > 0$ and "blue" asteroids with $a^* < 0$. We considered the "red" and "blue" asteroids as S-like and C-like asteroids, respectively. The diameter was obtained in the manner discussed in Section 4.4. The albedo was given as 0.19 for S-like asteroids and 0.08 for C-like asteroids. Figure 1.8(b) shows the absolute magnitude distribution and CSD in the SDSS MOC. According to the absolute magnitude distribution, the detection limit was $H_r \sim 16.5$ mag, which corresponds to $D \sim 2$ km at the outer edge of the main belt with the albedo of C-like asteroids.

5.1.3 Combined CSDs

Finally, we constructed the continuous CSDs using the ASTORB for $D >$ 10 km, the SDSS MOC for 2 km $< D <$ 10 km, and Subaru data for 0.7 km $< D <$ 2 km. We used the only asteroids with $a = 2.5$–3.3 AU to set the same sample condition as the analysis of the Subaru data in Section 5.1.1. The CSDs from the SDSS MOC were scaled to the cumulative number of the ASTORB sample at $D = 10$ km. The CSD curves derived from the ASTORB and SDSS MOC connected smoothly in both the low-i and high-i samples. Likewise, the CSDs from the Subaru data were scaled to the cumulative number of the SDSS MOC sample at $D = 2$ km.

Figure 1.9 shows the combined CSDs of low-i ($i < 15°$) and high-i ($i >$ 15°) MBAs. The CSD slopes of the asteroids from 0.7 km to 50 km in diameter were $b = 2.17 \pm 0.02$ for low-i MBAs and $b = 2.02 \pm 0.03$ for high-i

MBAs, respectively. The high-i MBAs had a shallower CSD than the low-i MBAs, at least down to $D = 0.7$ km. The difference in b was not caused by the wavy patterns seen in Figure 1.9. For confirmation we adjusted the high-i CSD to the low-i CSD at $D = 50$ km, and its power-law index was transformed to the same value as the low-i CSD (see Fig 1.10). The adjusted CSD of high-i MBAs agreed well with the low-i CSD over all sizes. To state the significance of this result, we performed a t-test (see Section 5.1.1) with the null hypothesis H_0: a regression line of the CSD difference, $y = y_0 - bx$ where $y = \log N_1(> D) - \log N_2(> D)$, is not significant ($b = 0$) and the alternative hypothesis H_1: the regression line is significant ($b > 0$). The t-value is $b/\sqrt{\Sigma V f^{-1}} = 16.2$, much greater than $t_{0.01}$ (2.43). It rejected the null hypothesis at the 99% confidence level. This test indicated that the overall high-i CSD was definitely shallower than the low-i CSD.

5.2 Differences in the CSD Slopes

5.2.1 Collision velocities

Collisional fragmentation is characterized by impact strength, $Q^*_{\rm D}$. $Q^*_{\rm D}$ is the critical specific energy to fragment the target and disperse half of its mass. It depends on asteroid size, generally expressed as

$$Q^*_{\rm D} \propto D^s. \tag{1.9}$$

The $Q^*_{\rm D}$ curve has two different power laws with opposite signs. For small bodies, $Q^*_{\rm D}$ decreases with increasing diameter ($s < 0$), in what is called the strength-scaled regime. In contrast, strength increases with increasing diameter ($s > 0$) for large bodies, in what is called the gravity-scaled regime. The two slopes join at the transition diameter (D_t) of 0.1–1 km (Durda et al., 1998). O'Brien and Greenberg (2003) showed that the power-law index of the CSD with $D > D_t$ is determined by the power-law index of the $Q^*_{\rm D}$ curve in the gravity-scaled regime, $s_{\rm g}$. According to the collisional steady-state

scenario, this relationship is described by

$$b = \frac{5}{2 + s_{\rm g}/3}. \tag{1.10}$$

In the present study, the overall CSD slope of high-i MBAs ($b = 2.02$) was smaller than that of low-i MBAs ($b = 2.17$), corresponding to $s_{\rm g} = 0.91$ and $s_{\rm g} = 1.43$, respectively. The most remarkable difference between the low-i and high-i MBAs was collision velocity. The mean relative velocity among MBAs, most of which are low-i bodies, is 3.8 km s^{-1} (Vedder et al., 1998). In contrast, high-i MBAs often collide at high velocities, around 10 km s^{-1} (Gil-Hutton, 2006). We propose that these hypervelocity collisions have a large $s_{\rm g}$.

However, such $s_{\rm g}$ has not been determined through previous impact experiments nor through numerical simulations. Benz and Asphaug (1999) performed impact simulations for basalt at two different collision velocities, 3 km s^{-1} and 5 km s^{-1}, and found that $s_{\rm g}$ did not vary between the two velocities. However, Jutzi et al. (2010), using impact simulations, reported that the $s_{\rm g}$ of basalt targets for 5 km s^{-1} ($s_{\rm g} = 1.29$) was smaller than that for 3 km s^{-1} ($s_{\rm g} = 1.33$). These values correspond to $b = 2.06$ and $b = 2.05$, respectively. This difference is too small to be recognized through observations. Their results showed that $s_{\rm g}$ does not depend strongly on collisional velocity enough to shift b. But the relationship between the $Q^*_{\rm D}$ curve and collision velocity, especially in the hypervelocity collisions around 10 km s^{-1}, is still uncertain. Our study might present evidence for an increase in $s_{\rm g}$ in hypervelocity collisions around 10 km s^{-1}.

5.2.2 Taxonomic distribution

Examined qualitatively, it is possible that the different spatial distributions between taxonomic groups caused the discrepancy in the CSD slopes between low-i and high-i MBAs. The population ratio of S-like to C-like asteroids is not uniform with inclination. Mothé-Diniz et al. (2003) showed that a smaller fraction of S-complex MBAs with $D > 7$ km appears in the

high eccentricity/inclination regime. Meanwhile, several observations have indicated different CSD slopes for different taxonomic groups, mostly in low inclination (Ivezić et al. 2001, Yoshida & Nakamura 2007, Wiegert et al. 2007). This difference in abundance between the taxonomic groups could induce an apparent decrease in the CSD slope in high inclination.

We checked this effect using the SDSS MOC data. The SDSS asteroids were separated into S-like and C-like groups by a^* color defined in Eq. 1.8. The low-i MBAs included 6585 S-like asteroids and 9746 C-like asteroids. The high-i MBAs include 1139 S-like asteroids and 2019 C-like asteroids. The CSDs of the low-i and high-i MBAs (2.5 AU $< a <$ 3.3 AU) were constructed in each group. The power-laws for these CSDs were approximated for the 2–10 km in diameter range. Among the S-like asteroids, the slope, named $b_{\rm s}$, was 2.66 $\pm$ 0.04 for low-i MBAs and 2.26 $\pm$ 0.03 for high-i MBAs. Among the C-like asteroids, the slope, named $b_{\rm c}$, was 2.41 $\pm$ 0.02 for low-i MBAs and 2.36 $\pm$ 0.05 for high-i MBAs. The $b_{\rm s}$ value was significantly smaller in high inclination, while $b_{\rm c}$ was similar for low-i and high-i MBAs.

We evaluated the contribution of the S-like MBAs to the decrease in b of high-i MBAs. Model CSDs were compounded from artificial power-law CSDs of S-like and C-like MBAs based on a population model. The model was characterized by a population ratio of S-like MBAs to C-like MBAs and their CSD slopes (Table 1.3). We compared indexes of fitted power laws to the model CSDs with those of the observed CSDs using two models. In model 1, we explored the possibility that the small $b_{\rm s}$ of high-i S-like MBAs was a major factor in the small b of total high-i MBAs. The population ratio of S-like asteroids was set to the same value as the SDSS MOC data, 0.67 (6585/9746) for low-i MBAs and 0.56 (1139/2019) for high-i MBAs. The $b_{\rm s}$ and $b_{\rm c}$ values for high-i MBAs were set to match the low-i MBAs ($b_{\rm s}$=2.66, $b_{\rm c}$=2.41). The model CSDs showed $b = 2.50$ for low-i MBAs and $b = 2.49$ for high-i MBAs. The CSD slope of high-i MBAs was not as small as that of the observed CSD. Consequently, these results show that a small (compound) slope b in the high-i MBAs requires a smaller S-type slope $b_{\rm s}$

for that region. In model 2, we examined the possibility that the small S-like/C-like population ratio of high-i MBAs caused the small b. The test was performed assuming that high-i MBAs have the same population ratio as low-i MBAs. The CSD power-law indexes were set to match the SDSS MOC data, ($b_{\rm s}$, $b_{\rm c}$) = (2.66, 2.41) for low-i MBAs and ($b_{\rm s}$, $b_{\rm c}$) = (2.26, 2.36) for high-i MBAs. The best-fit power-law indexes of the compounded CSDs were $b = 2.50$ for low-i MBAs and $b = 2.32$ for high-i MBAs. The both of b values agreed with the observed CSDs. This indicates that the scarcity of S-like asteroids with high inclination had little influence on the CSD slope. We conclude that the shallow CSD of the high-i MBAs was due to the small CSD slope of S-like MBAs with high inclination.

We suggest that $s_{\rm g}$ values for high-velocity collisions (around 10 km s^{-1}) of S-like asteroids are large, while $s_{\rm g}$ values for similar C-like asteroids are not. One possible cause is the variation in porosities between S-like and C-like asteroids. C-type asteroids have porosities of 35–60%, whereas S-type asteroids have porosities of around 30% (Britt et al., 2002). Jutzi et al. (2010) showed through impact simulations that $s_{\rm g}$ is constant (1.22) between collision velocities of 3 km s^{-1} and 5 km s^{-1} for porous targets (pumice). On the other hand, the $s_{\rm g}$ values for 5 km s^{-1} collisions (1.29) is smaller than 3 km s^{-1} collisions (1.36) for the non-porous targets (basalt). Porosity may have a resistance effect to $s_{\rm g}$ variation with collision velocity.

Note that these considerations include uncertainty. The wavy structure of the CSD may differ between S-like and C-like MBAs. Estimating the CSD slopes from a narrow size range is not appropriate for comparing the overall slope b. Indeed, previous surveys have presented a variety of results. Ivezić et al. (2001) showed $b = 3.00 \pm 0.05$ for both groups with $D \geq \sim$5 km, and $b = 1.20 \pm 0.05$ for S-like asteroids and $b = 1.40 \pm 0.05$ for C-like asteroids with $D \leq \sim$5 km. Yoshida and Nakamura (2007) showed $b = 2.44 \pm 0.09$ for S-like asteroids with 1 km $< D <$ 3 km and $b = 1.29 \pm 0.02$ with 0.3 km $< D <$ 1 km, and a single slope $b = 1.33 \pm 0.03$ for C-like asteroids with 0.6 km $< D <$ 7 km. The difference in CSD between the S-like and C-like

asteroids is still unclear.

5.2.3 Dynamical removal

Dynamical processes, as well as collisional processes, affect the shape of the CSD. O'Brien and Greenberg (2005) showed via numerical simulations that the CSD slope of MBAs is reduced from ∼20 km in diameter through the action of the Yarkovsky effect and resonances. The Yarkovsky effect causes a drift in the semi-major axis, the rate of change of which increases with decreasing size down to 0.01 km in diameter. Asteroids caught in a strong resonance are removed from the main belt. Smaller asteroids are removed more quickly from the main belt. Although the Yarkovsky effect is independent of inclination, several secular resonances appear at high inclination. Within the heliocentric distance of 2.5–3.3 AU, none of these resonances appear at $i < 15°$. In contrast, the strong secular resonances of ν_5, ν_6, and ν_{16} lie in $i > 15°$ (Knezević et al., 1991). High-i asteroids in this zone are subject to removal. These secular resonances together with the Yarkovsky effect could cause significant losses of high-i MBAs, possibly enough to diminish the CSD slope. This action increases the difference in b between the low-i and high-i MBAs at small sizes ($D \leq$∼20 km). However, as shown in Figure 1.10, the difference in b is almost constant as the diameter decreases from $D \sim 50$ km. This is inconsistent with the above expectation. Hence, dynamical removal does not decrease b in high inclination.

6 Conclusion

We performed wide-field observations of high-i MBAs of sub-km diameter using the 8.2 m Subaru Telescope. The CSDs of low-i and high-i MBAs were constructed using the Subaru data and the ASTORB and SDSS MOC catalogs. A summary of our main conclusions follows.

(1) A smaller fraction of small asteroids (0.7 km $< D <$ 1 km) appear in high inclination. The power-law index of the CSD for the 0.7–2 km diameter range is 1.79 $\pm$ 0.05 for low-i MBAs ($i < 15°$) and 1.62 $\pm$ 0.07 for high-i ($i > 15°$) MBAs. The sub-km asteroids at $i > 15°$ have a lower index than the low-i sample at the 95% confidence level based in a statistical t-test.

(2) The single power-law slope of the combined CSD for diameter in the 0.7–50 km range is 2.17 $\pm$ 0.02 for the low-i MBAs and 2.02 $\pm$ 0.03 for the high-i MBAs. The high-i CSD is shallower than the low-i CSD for the entire size range at the 99% confidence level. This is not caused by the difference in the wavy pattern of the CSDs.

(3) The CSD of S-like asteroids has a small slope in high inclination, whereas that of C-like asteroids shows little variation in slope with inclination. Through modeling we showed that the shallow CSD of the high-i MBAs is not caused by the spatial distribution of the taxonomic groups, but by the shallow CSD of the S-like MBAs with high inclination.

(4) The difference in slope of CSDs between the low-i and high-i MBAs is constant across $D \sim 10$ km. The shallow CSD of the high-i MBAs is not the result of dynamical removal due to the Yarkovsky effect and the secular resonances.

We suggest that the small b of S-like MBAs with high inclination is due to a collisional effect. The possible explanation is that the $Q^*_{\rm D}$ curve has a large gravity-scaled regime $s_{\rm g}$ slope under hypervelocity collisions (around 10 km s^{-1}). Asteroid collisions often occurred with such high velocities in the dynamical excitation phase in the final stage of planet formation. We suppose that during this phase, MBAs experienced oligopolistic collisional evolution; small bodies were more easily disrupted relative to large bodies

than at present. This indication claims that the current evolutionary models for MBAs should be modified.

Part II
PHOTOMETRIC OBSERVATIONS IN THE IRREGULAR SATELLITES OF URANUS

1 INTRODUCTION

1.1 Irregular Satellites

Recently a number of satellites were discovered in the giant planet systems. To date, it is known that there are 63 satellites around Jupiter, 62 satellites around Saturn, 27 satellites around Uranus, and 13 satellites around Neptune. The orbital parameters of these satellites have been already determined.

The satellites are divided into two groups by characteristics of the orbital elements (Stevenson et al., 1986). The satellites nearby the host planets have nearly circular and prograde orbits very close to the equatorial plane of the planets. They are called *regular* satellites. The other satellites, called *irregular* satellites, have large semi-major axes with eccentric and highly inclined (with respect to the ecliptic plane) orbits, most of which are even retrograde.

The satellites are definitely classified based on the ratio of a semi-major axis to a radius of the planets' Hill spheres. The Hill sphere is the region in which the planet is superior to the Sun for the gravitational attraction toward the satellites. The radius of the Hill sphere is written by

$$r_{\rm H} \sim a_{\rm p} \left(\frac{\mu}{3} \right)^{1/3}, \tag{2.1}$$

where a_p is the orbital semi-major axis of the planet and μ is the mass fraction of the planet to the Sun. $r_{\rm H}$ values are 0.35–0.77 AU for the giant planets (Table 2.1). The regular satellites have a semi-major axis less than 0.05 $r_{\rm H}$. In contrast, irregular satellites have a semi-major axis larger than 0.05 $r_{\rm H}$ and are found up to 0.65 $r_{\rm H}$.

Regular satellites are tightly bound to the host planet. They have orbits with low eccentricities ($\sim$0.01), low inclinations (mostly $<1^\circ$), and prograde

revolutions. It is generally believed that regular satellites were formed within a circumplanetary disk around the planets (Mosqueira & Estrada, 2003).

While regular satellites of giant planets were first discovered in 1610 by Galileo, the studies for irregular satellites started in the 20th century. Because most of them are small (i.e. faint), they are difficult to be found. Since large-aperture telescopes and wide-field CCD instruments were introduced for observations, the number of discovered irregular satellites have dramatically increased only recently. Today 55 Jovian, 14 Satunian, 9 Uranian, and 7 Neptunian irregular satellites are known (Table 2.1). It is also known that the irregular satellite populations dominate the satellite systems of the giant planets, except for Uranus. We note that the sparseness of irregular satellites of Uranus and Neptune is possibly due to the observational bias that satellites around a distant planet are difficult to be found (Figure 2.1). In fact, the distance-corrected size distributions are indistinguishable among the giant planets (Figure 2.2). Further irregular satellites must be found especially around Uranus and Neptune in the future.

1.2 Origin of Irregular Satellites

Irregular satellites have unusual orbits with high eccentricities, high inclinations, and mostly retrograde orbits (Figure 2.3). They were unlikely formed in a circumplanetary disk. Instead, it is suggested that they were external-origin bodies captured from heliocentric orbits by the host planet. However, the capture of a heliocentric body is not easy. The orbital energy must be dissipated enough to transfer to a stable planetcentric orbit. Such a drastic event can never happen in the present Solar system (Heppenheimer&Porco, 1977). Therefore, irregular satellites must have been captured into their current orbits in the early Solar system.

This idea is supported by a planetary migration hypothesis, called *Nice* model. According this model, the giant planets were located in the closer region to the Sun, from $\sim$5.5 AU to $\sim$14 AU immediately after the planet

formation. At that time, a disk of planetesimals existed beyond the orbits of the giant planets up to ∼34 AU. The migration of the giant planets occurred due to their interaction with the planetesimals disk. Jupiter moved slightly inward, while Saturn, Uranus, and Neptune drifted outward (Tsiganis et al., 2005). When Jupiter and Saturn crossed their 1:2 (ratio of orbital periods) mean-motion resonance, a great dynamical instability was induced into the planetesimal disk and the most of planetesimals around the giant planets were scattered out of the planetary region (Gomes, 2005). A small fraction of the residuals have survived as the small Solar system bodies. Numerical simulations indicated that the dynamical structure of trans-Neptunian objects (TNOs) was caused by the outward migrations of Uranus and Neptune (Levison et al., 2008). A portion of the residual planetesimals was captured by Lagrange points (L4 and L5) of the giant planets such as Jupiter and Neptune as Trojan objects (Morbidelli et al., 2005; Tsiganis et al., 2005). Irregular satellites were likely to be captured by the giant planets during this phase.

However, the mechanism of the capture is still unknown. Several scenarios have been suggested to explain the capture of irregular satellites such as

- During or immediately after growth of the core, the giant planets possess a bloated atmosphere hundreds of times larger than the current planet size. If a small body passing through this atmosphere loses enough orbital energy due to gas drag, it can be captured (Pollack et al., 1979; Astakhov et al., 2003).

- After formation of the planet's core, it pulls in a plenty of gas and the planet mass rapidly grows. A nearby small body can be trapped by the suddenly-expanded Hill sphere of the planet (Heppenheimer&Porco, 1977; Viera Neto & Winter, 2001).

- If two bodies encounter a giant planet, the either could be captured due to the gravitational interactions (Colombo & Franklin, 1971).

As well as the capture mechanism, the sources of the irregular satellites are also unidentified. There are three prime candidates: the local regions, trans-Neptunian belt, and asteroid main belt. Local bodies to the planet are the easiest to be captured because of the small relative velocities. TNOs are another plausible source of the irregular satellites. Morbidelli et al. (2005) argued that the Trojan asteroids of Jupiter could have formed in the trans-Neptunian region and then been captured during the planetary migration event, indicating that the TNOs, Jupiter Trojans, and irregular satellites have the same origin. In addition, asteroids in 2–5 AU from the Sun could be transported near both Jupiter and Saturn (Higuchi et al., 2010).

For any sources, the origin of irregular satellites is important. If the source regions were local to the planet, irregular satellites were survivors of primordial planetesimals in a sparse region at present before the Neptune's orbit. If the source regions were non-local, irregular satellites can be a valuable indicator for investigating the extensive dynamical evolution over the Solar system.

1.3 Surface Properties of Small Bodies

One of the most available approaches for exploring the origin of irregular satellites is a comparison of surface properties between irregular satellites and other small bodies. Surface properties include compositions, structure (monolith/gravels/regolith), surface roughness, density, porosity, strength, and thermal inertia. Because most irregular satellites are faint, it is difficult to carry out spectroscopic and polarimetric observations. The optical imaging observation with a large-aperture telescope is suitable for exploring the origins and evolutions of the irregular satellites. The physical data obtained from optical imaging are colors and phase curves.

Colors of small bodies give information on the surface composition. Asteroids (rocky bodies) have several taxonomic classes such as S-, C-, E-, M-, and P-types characterized by silicaceous materials (e.g. olivine and pyroxene),

carbonaceous hydrated materials, enstatite, Fe-Ni metal, and anhydrous silicates, respectively (Gaffy, 1993). These are classified by the color/spectrum and albedo. Distant icy bodies, such as TNOs and Centaurs, are also known to have a diversity of color properties.

The surface colors of small bodies are characterized by the following two effects. One is the absorption features of the specific mineral or molecular species. For example, olivine has a broad absorption band around 1 μm which is the most pronounced factor factor to specify the color of S-type asteroids. The other is the surface reddening effect due to the solar ultraviolet photons and solar wind particles, called space weathering. The fact that TNOs mostly show red colors is explained by the presence of CH_4 ice which is converted into red organic molecules through the effect.

The both of asteroids and icy bodies have a variety of surface colors. It indicates that they have multiple types of composition and/or experienced a varying degree of surface modification. However, it is not absolutely that a same color between small-body populations signifies common surface composition. This is because some different materials have a similar spectrum, e.g. E-, M-, and P-type asteroids, collectively called as X-type. It is insufficient to identify the similarity of the surface compositions only by the colors.

Another observable amount available for comparison of surface properties between the irregular satellites and other small bodies includes a phase curve. It is a brightness variation as a function of a Sun–object–observer angle, called phase angle. It is widely known that the brightness of small bodies increases with approaching to the opposition where the object locates at zero phase angle. This effect, called *opposition surge*, is generally observed in asteroids, distant icy bodies, regular satellites, and Saturn's ring (e.g. Muinonen et al., 2002; Schaefer et al., 2009; Mishchenko et al., 1993). Particularly, drastic magnitude increases at small phase angles ($<\sim 5^\circ$) were detected in various bodies.

The two physical mechanisms of the opposition surge are usually considered: shadow hiding and coherent backscattering. The shadow hiding

is induced by the rough interface between the regolith and the free space and by the internal geometric structure. The interfacial shadowing depends mainly on surface roughness, while the internal shadowing depends mainly on the volume density of scattering medium. Meanwhile, the coherent backscattering is caused by constructive interference of multiple scattered light (Muinonen et al., 2002). It depends on parameters of the multiple scattering efficiency; particle size (the ratio of particle radius to the wavelength), distance between the particles (packing structure), and the optical constants of the material. Therefore, the shape of the opposition surge is varied by the surface composition and the granular structure. These dependences were confirmed in the laboratory experiments (e.g. Nelson et al., 2000).

The notable significance is that there is a strong correlation between the surge and albedo; the high-surge objects have low albedo (e.g. Belskaya & Shevchenko, 2000). The shadow hiding effect is dominant on the surge in such objects because it arises from the reflected light, not multiple scattering. It means that the phase curve close to the opposition includes information of albedo, which cannot be obtained by only the color data. In this study, we used the phase curve to investigate the origin of the irregular satellites.

1.4 Motivation of This Study

Several previous observations measured the colors of irregular satellites (e.g. Grav et al., 2003). Figure 2.4 shows the color-color ($B-V$ vs. $V-R$) diagram including the irregular satellites of the four giant planets and TNOs (KBOs). The colors of the irregular satellite vary from neutral (Sun-colored; $B-V=0.65$ mag) to moderately red ($B-V\sim0.9$). It means that the color distributions are different between the irregular satellites and TNOs.

In contrast, the phase curves of irregular satellites have never been observed, except for Nereid, the largest irregular satellite of Neptune (Schaefer et al., 2008). In this study, we measured phase curves of the irregular satellites to explore the origins and dynamical evolution processes of the irregular

satellites of Uranus. The Uranian irregulars are intriguing objects because they are located at the intermediate region between Jupiter's orbit and trans-Neptunian regions. They are suitable for investigating the orbital evolution of planetesimals which gives meaningful clues to the planetary migration processes (e.g. Tsiganis et al., 2005).

We performed three-night photometric observations for irregular satellites of Uranus at different phase angles. We compared the surge properties between irregular satellites and other small body populations and discussed the source region of the Uranian irregular satellites.

2 OBSERVATIONS

Observations were conducted on September 1, 2, and 29, 2008, using the Suprime-Cam (Miyazaki et al., 2002) mounted on the 8.2-m Subaru Telescope. The Suprime-Cam consists of ten fully-depleted-type 2048×4096 CCDs manufactured by Hamamatsu Photonics KK, which are arranged in a 5×2 pattern with interchip gaps of 14″–16″. The field of view is $34' \times 27'$ with a pixel scale of 0″.20. Each Image was obtained with a 240-sec exposure using the VR-band filter. The center wavelength and FWHM of the VR filter are 0.6 μm and 0.2 μm, respectively (Figure 2.5), which provides a factor of two increase in throughput with a small increase in the sky background compared to a standard R-band filter (Jewitt et al., 1996). A typical sky motions of the Uranus and its satellites are ∼5–6 arcsec hr^{-1}. The satellites appear as point light sources in the exposure time.

The observed areas were around the Uranus at the center of ($\alpha_{\rm J2000.0}$, $\delta_{\rm J2000.0}$) = ($23^{\rm h}28^{\rm m}.7$, $-4°00'$) on Sep. 1, ($23^{\rm h}28^{\rm m}.5$, $-4°02'$) on Sep. 2, and ($23^{\rm h}24^{\rm m}.6$, $-4°27'$) on Sep. 29, seen in Figure 2.6. The typical seeing was 0″.70 in the first night, 0″.65 in the second night, and 0″.60 in the last night (Figure 2.7). Uranus was located at the interchip gap among the chip 2 (fio), 5 (satsuki), 7 (clarisse), and 9 (san) in each night (Figure 2.8, 2.9). The phase angles between the Sun and observer from Uranus were ∼0.6° in the first and second nights and ∼0.8° in the last night. The field covers all the area within 0.24 $r_{\rm H}$ and reaches up to 0.44 $r_{\rm H}$.

Images were obtained with 69 shots during 5.6 hours in the first night, 68 shots during 5.5 hours in the second night, and 59 shots during 6 hours in the last nights. The field of view was moved for each frame to track Uranus. Several Landolt standard stars (Landolt, 1992) were used for photometric calibration and airmass correction (Table 2.4). Three fields where they are located were taken at the beginning and/or ending of the observation in each night (Table 2.5).

3 ANALYSIS

3.1 Data Reduction

All the images were processed by standard reduction procedures: bias subtraction, flat fielding, and background correction basically using IRAF. A sequence of the processes were carried out for each chip. The bias frames were created by averaging 5–10 images taken with 0-sec exposures. The flat-field frames were created by taking the median of 10–12 images taken with 2–120-sec exposures of the evening twilight. The background gradient was corrected by the following procedures: (i) the frame was divided into 72 grids and a mode value was measured in each grid (ii) a count value of every pixel was replaced into a mode value in the grid (iii) a pseudo sky frame was created from a fitted three-dimensional spline function to the above image using the `IMSURFIT` task in IRAF and was subtracted from the original image. The processed image is shown in Figure 2.10. Lastly, the frame coordinates were matched for all images obtained in a night.

3.2 Identification of Satellites

The positions of known satellites at the observations are inquire through the HORIZONS System[1] produced by the Jet Propulsion Laboratory, NASA (Table 2.6). All the regular satellites were too nearby Uranus to be identified. Seven irregular satellites were located in the observed field: XVI Caliban, XVII Sycorax, XVIII Prospero, XIX Setebos, XX Stephano, XXI Trinculo, and XXII Francisco (Figure 2.8, 2.9). All of them were detected from the data for the first night (Figure 2.11). Trinculo and Francisco are too faint ($R\sim$25.4 mag and $R\sim$25.0 mag, respectively; Sheppard et al. 2005) to detect

[1] ⟨http://ssd.jpl.nasa.gov/horizons.cgi⟩.

from the data for the second night. Caliban, Stephano, and Francisco are too close to Uranus to detect from the data for the last night.

3.3 Photometry

3.3.1 Relative Photometry

The brightness variations of the detected irregular satellites were measured by relative photometry. Trinculo and Francisco were excluded because they are too faint to obtain accurate lightcurves. Non-saturated stars (R=19–21 mag) listed in the USNO catalog[2] were used as reference stars. Because the correlation between the atmospheric extinction and airmass depends on wavelength, we used only stars with the difference of $V-R$ colors within ± 0.05 mag from each satellite. The V–R colors of the satellites were derived from Grav et al. (2004) (Table 2.3). The colors of the reference stars were converted from the USNO B–R using a correlation of $(V-R) = 0.04(B-V)^2 + 0.38(B-V) + 0.03$ for main sequence stars (Figure 2.12) derived from Drilling & Landolt (2000). We also confirmed whether it was not galaxy or non-object. 10–20 reference stars were used for each satellite.

Aperture photometry was performed using the `QPHOT` task in IRAF. For relative photometry, the object flux was measured with an aperture of 1.0-arcsec radius for all of the satellites and reference stars. It was because an aperture with radius of around 1.5 FWHM ($\sim 0''.6$–$0''.7$) provided a high signal-to-noise ratio (SNR) with small contamination from background sources (Grav et al., 2003).

[2]USNOFS Image and Catalogue Archive operated by the United States Naval Observatory, Flagstaff Station ⟨http://www.nofs.navy.mil/data/fchpix/⟩.

3.3.2 Calibration

The temporal brightness variation of a satellite at the V-band was estimated from

$$V(t) = V_{\rm ref} - 2.5 \log \left(\frac{I_{\rm obj}(t)}{I_{\rm ref}(t)} \right). \tag{2.2}$$

$I_{\rm obj}/I_{\rm ref}$ indicates a flux ratio between the satellite and the sum of the reference stars obtained by relative photometry. The typical value of the ratio was $\sim 5 \times 10^{-3}$, i.e. the contribution of reference stars to photometric uncertainty was less than 10%. $V_{\rm ref}$ shows total V magnitude of the reference stars given by

$$V_{\rm ref} = V_{0,\rm c}(1) - c \cdot (\text{airmass} - 1) - 2.5 \log I_{\rm ref,abs} \tag{2.3}$$

$I_{\rm ref,abs}$ is total flux of the reference stars measured by absolute photometry with radius of $2''.4$. $V_{0,\rm c}(1)$ is the zero point V magnitude derived from the V–R color at the minimum atmospheric extinction, that is airmass=1. c is the coefficient of atmospheric extinction.

Absolute photometry for the Landolt standard stars provides its zero point magnitude

$$V_0(t) = V_{\rm std} + 2.5 \log I(t), \tag{2.4}$$

where $V_{\rm std}$ is the magnitude of a standard star and I is the measured flux. We used all the Landolt stars (4–6 objects) located in a field of view, i.e. with a same airmass (Table 2.4). Figure 2.13 shows the correlations between $V - R$ color and V_0 for the Landolt stars. The extinction coefficient c was estimated by fitting Eq. 2.3 using a least-square method (LSM). The differences of V_0 among the lines were made by different atmospheric extinction. The V_0 value at the V–R color of a satellite on the fitted line gives $V_{0,\rm c}(A)$ at airmass of A. Figure 2.14 shows the correlations between airmass and $V_{0,\rm c}(A)$. They well approximated by linear lines fitted with LSM except for the data in Sep. 29. $V_{0,\rm c}(1)$ and c were derived from the value at airmass=1 and the slope of these lines, respectively. Because the range of airmass of the standard stars was too small to determine an approximated line in the data in Sep. 29, its $V_{0,\rm c}(1)$ and c were estimated from the reference stars used

for relative photometry instead of the standard stars. Figure 2.15 shows the correlations between airmass and $V_{0,c}(A)$ derived from the total flux of the reference stars for Sycorax ($0.58<V-R<0.68$), Prospero ($0.34<V-R<0.44$), and Setebos ($0.30<V-R<0.40$). $V_{0,c}(1)$ and c were determined by the fitted linear lines with LSM. Table 2.7 shows $V_{0,c}(1)$ and c of each satellite.

4 RESULTS

4.1 Light Curves

The brightness of the satellites were derived from Eq. 2.2 with airmass corrections in Eq. 2.3. Figures 2.16–2.20 show light curves for Caliban, Sycorax, Prospero, Setebos, and Stephano. The photometric errors were estimated from the equations presented by Newberry (1991) as

$$\sigma(m) \approx \frac{1.0857}{\sqrt{C/g + n\sigma_{\rm bg}^2(1 + n/n_{\rm bg})}}, \tag{2.5}$$

where C is measured flux of the object, g is a gain factor with an unit of electrons ADU^{-1}, $\sigma_{\rm bg}^2$ is the variance of the sky background, n is the area of the aperture in square pixels, and $n_{\rm bg}$ is the number of the background pixels. The SNRs were ∼70 for Caliban, ∼270 for Sycorax, ∼30 for Prospero and Setebos, ∼10 for Stephano (no large differences among the date). Maris et al. (2007) measured brightness variations of the Uranian satellites using the 8.2-m ESO Very Large Telescope (VLT) with SNRs of ∼120 for Sycorax, ∼10 for Prospero and Setebos, and ∼5 for Stephano. Our photometric observations reached 2–3 times better SNR than them.

The brightness variations in the lightcurves were never due to the photometric errors. We performed statistical tests to check randomness of the brightness variations of the satellites. We used the Wald-Wolfowitz runs test (Wald & Wolfowitz, 1940) against the null hypothesis H_0 that a series of the photometric data was random. The rejection of H_0 indicates that the data set has a regularity. We defined the number of observation points with the brightness larger than the mean as n_1 and defined the number of the other points as n_2. The number of runs, uninterrupted sequences of data points that are either all above or below the mean, was denoted by r. The test

statistic is written by

$$z = \frac{r - \left(\frac{2n_1n_2}{n_1+n_2} + 1\right)}{\sqrt{\frac{2n_1n_2(2n_1n_2 - n_1 - n_2)}{(n_1+n_2)^2(n_1+n_2-1)}}}, \tag{2.6}$$

which is asymptotically normally distributed. In case of $|z| \geq z_0$ with a significance of 0.05 (z_0=1.96), the null hypothesis is rejected at 95% confidence level. The results of the run test are shown in Table 2.8. Caliban, Sycorax, and Prospero were indicated to have directional magnitude variations with a high level of confidence. Stephano was also shown to have nonrandom fluctuations in the first-night data. In contrast, the brightness variations of Setebos were significantly caused by random errors. Those root-mean-square of the variations were 0.06 mag, 0.04 mag, and 0.05 mag for the data at Sep 1, 2, and 29, respectively. The upper limits of the amplitude of Setebos's lightcurve is ∼0.05 mag across the observations. This is not consistent with ∼0.19-mag amplitude of the magnitude variations with 4.4-hr period for Setebos indicated in Maris et al. (2007).

4.2 Periodic Analysis

A non-spherical and surface-uniform body exhibits double-peak periodic variation of magnitude due to the rotation. We performed periodic analyses to determine rotational period and amplitude of the observed lightcurves for Caliban, Sycorax, Prospero, and Stephano. We used the data obtained in Sep. 1 and Sep. 2 for the first analysis. The change in brightness due to phase angle was assumed to be negligible. Unfortunately, the data sequences were too sparse to describe the overall shape of the lightcurves during a rotational period. We searched for the periodicities with an assumption that the magnitude variations were represented as sinusoidal curves

$$V(t) = A\cos\left(\frac{2\pi}{P}(t-\tau) + \phi\right) + V_0, \tag{2.7}$$

where $V(t)$ is the measured magnitude, V_0 is the basement magnitude, A is the amplitude, P is the period of magnitude variations, ϕ is the phase, and τ is an epoch. We ignored non-uniform amplitudes and albedo inhomogeneity. Note that P means a half of the rotational period.

We used the spectral analysis method, called as the Lomb-Scargle periodogram (Lomb, 1976; Scargle, 1982; Maris et al., 2007). The period is found by the discrete Fourier transform in this analysis. It is suitable for lightcurve data obtained by unequally-spaced observations. For this method, Eq. 2.7 is expressed as

$$V(t) = A_{\rm c} \cos\omega(t-\tau) + A_{\rm s} \sin\omega(t-\tau) + V_0, \tag{2.8}$$

where $\omega = 2\pi/P$, $A_{\rm c}$ and $A_{\rm s}$ are amplitudes of the co-sinusoidal and sinusoidal components. A and ϕ are written by $A_{\rm c}$ and $A_{\rm s}$ as $A = \sqrt{A_{\rm c}^2 + A_{\rm s}^2}$ and $\phi = \tan^{-1}(A_{\rm c}/A_{\rm s})$. The arbitrary constant τ is given by

$$\tan(2\omega\tau) = \frac{\sum w_j \sin(2\omega t_j)}{\sum w_j \cos(2\omega t_j)}, \tag{2.9}$$

where $w_j \propto 1/\sigma_j^2$ (σ_j: photometric error). The best-fit $A_{\rm c}$ and $A_{\rm s}$ which minimize χ^2 of the weighted fitting residual

$$\chi^2(\omega) = \sum w_j (A_{\rm c} \cos\omega(t_j-\tau) + A_{\rm s} \sin\omega(t_j-\tau) + V_0 - V(t_j))^2 \tag{2.10}$$

are given at $\partial\chi^2/\partial A_{\rm c} = 0$ and $\partial\chi^2/\partial A_{\rm s} = 0$ as

$$\begin{aligned} A_{\rm c} &= \frac{\sum w_j V(t_j) \cos\omega(t_j-\tau)}{\sum w_j \cos^2\omega(t_j-\tau)} \\ A_{\rm s} &= \frac{\sum w_j V(t_j) \sin\omega(t_j-\tau)}{\sum w_j \sin^2\omega(t_j-\tau)}. \end{aligned} \tag{2.11}$$

The minimum value of χ^2 is

$$\chi^2_{\rm min}(\omega) = \sum w_j (A_{\rm c} \cos\omega(t_j-\tau) + A_{\rm s} \sin\omega(t_j-\tau) + V_0)^2 - \sum w_j V^2(t_j). \tag{2.12}$$

The periodogram power $z(\omega)$ is defined as

$$\begin{aligned} z(\omega) &= \sum w_j V^2(t_j) - \chi^2_{\min}(\omega) \\ &= \frac{[\sum w_j V(t_j) \cos\omega(t_j-\tau)]^2}{\sum w_j \cos^2\omega(t_j-\tau)} + \frac{[\sum w_j V(t_j) \sin\omega(t_j-\tau)]^2}{\sum w_j \sin^2\omega(t_j-\tau)}. \end{aligned} \quad (2.13)$$

The periodogram computations were carried out with the Cyclocode program developed by Dermawan (2003). The periods of the fitted curve are shown with the powers and significance levels. Holsapple (2007) showed that most asteroids larger than 10 km in diameter have rotation periods from 2 to 100 hr corresponding to P = 1–50 hr. It is consistent with the Uranian irregular satellites with $P\approx$1–6 hr (Maris et al., 2007). We searched the periods from 1 to 50 hr with a step of $\sim 0.1P$. For confirmation we also checked the shorter periods from 0.25 to 1 hr, but no one showed a significant fit for the four satellites.

4.3 Parameter Determination

Figure 2.21 shows the power spectra for the observed satellites. The power means the goodness of the lightcurve fitting. A period with a large power indicates high accuracy of the lightcurve determination. We note that when a period P has a prominent power, periods at $2P$, $3P$, ... also tend to show large powers. For Caliban, Sycorax, and Prospero, the periods with large powers concentrate in 3–10 hr. Setebos has a confusing distribution with two concentrations around 2 hr and 10 hr. We defined periods with powers more than $\sim$90% of the maximum as candidates of the true period. We obtained two periods for Caliban, Sycorax, and Prospero, and four periods for Stephano. The candidates and fitted parameters of each satellite are shown in Table 2.9. The best-fit curves are presented in Figures 2.22–2.25.

We analyzed the data obtained in the last nights to assess the lightcurves. The photometric data were available for Sycorax and Prospero. Lightcurve fitting was conducted for the Sep-29 data using Eq. 2.8 under either of

the candidate periods. The obtained lightcurves as a function of the phase are shown in Figure 2.26 for Sycorax and Figure 2.27 for Prospero. The parameters of the lightcurves are presented in Table 2.10.

Sycorax had two period candidates, but the longer (P = 4.1 hr) was rejected because the goodness of fit was not small (χ^2 = 142) and the amplitude (A = 0.040 mag) disagree with the value derived from the first- and second-night data (A=0.021 mag). In contrast, the lightcurve with P = 3.5 hr showed χ^2 = 73 and A = 0.027 mag, which is consistent with the previous lightcurve with A = 0.022 mag. Though the fitting accuracy was not high because of small amount of the data within a short time compared to the previous data in Sep 1–2, it was useful to evaluate the two periods. We determined that the period of magnitude variation for Sycorax was P = 3.5 hr with amplitude of A = 0.022 mag. The period is consistent with Maris et al. (2007) indicating $P \approx 3.6$ hr. In contrast, both of the two candidates for Prospero showed similar fitness and inconsistent with the amplitudes in our previous observations. We could not ascertain the proper period.

The periods of Caliban and Stephano were also not specified. Maris et al. (2001) indicated that Caliban has 2.66-hr period of brightness variation, but it did not match our photometric data. Maris et al. (2007) suggested that the period of Stephano was $P \approx 2$ hr, but it was uncertain because of sparseness of their data.

The rotational periods, corresponding to twice the periods of the brightness variation P, were shown to be $P \approx$ 11–14 hr for Caliban, P = 7.1 hr for Sycorax, $P \approx$ 9–12 hr for Prospero, and $P \approx$ 4–5 hr or 19–30 hr for Stephano.

We found that the Uranian irregular satellites, whose sizes are 30–150 km in diameter (Sheppard et al., 2005), distribute between 4 hr and 30 hr. It is well consistent with asteroids and TNOs (Figure 2.28).

4.4 Phase Curves

We obtained the photometric data of Sycorax, Prospero, and Setebos in Sep. 1, 2, and 29. The Uranian satellites were located at the phase angle $\alpha \approx 0.6^\circ$ in the first/second nights and $\alpha \approx 0.8^\circ$ in the last night. The difference in phase angle, $\Delta\alpha \approx 0.2^\circ$, allows us to estimate the coefficient of the phase curve V_0 versus α. For Sycorax and Prospero, V_0 was derived from the fitted lightcurve. For Setebos of which lightcurves were not determined due to large photometric error, V_0 was defined as the mean value of observed magnitudes. Unfortunately, however, the standard deviation is too large to precisely determine Setebos's phase curve. The slope of the phase curves is estimated from the difference in V_0 during the one month, ΔV_0. We defined the slope as $S = \Delta V_0 / \Delta\alpha$. V_0, ΔV_0, and S are shown in Table 2.11. Sycorax has small S (0.03 ± 0.01 mag deg^{-1}), while Prospero has relatively large S (0.14 ± 0.03 mag deg^{-1}). Although we obtained only two phase curves, the difference between them was significant. We compared this result with other satellites and icy small bodies in the following section.

5 DISCUSSION

5.1 Surge Slopes of Small-body Populations

The color-surge correlations of TNOs and Centaurs shows that the property of the opposition surge depends on surface compositions (Schaefer et al., 2009). In addition, Schaefer et al. (2009) found that none of these objects with $i < 15^\circ$ had shallow surge, $S < 0.12$ mag deg^{-1}, while most of the surge slopes for objects with $i \geq 15^\circ$ distributed from 0 to 0.15 mag deg^{-1}. This is consistent with the positive correlation between color and inclination (Trujillo & Brown, 2002; Peixinho et al., 2008). The surge slope can be used as another tracer for orbital evolutions of small bodies in the outer Solar system. Radial migration of the small bodies is capable of bringing a dependence of the surface property on heliocentric distance.

The previous studies obtained phase curves of asteroids, JTs, TNOs, Centaurs, and planetary satellites. Belskaya & Shevchenko (2000) showed shapes of the phase curves for 33 asteroids with various taxonomic types. They approximated the curves using two parameters, surge amplitude (a) and linear slope (b), in the large phase angles ($\alpha > 5^\circ$) as

$$V(1;\alpha) = V(1;0) - a/(1+\alpha) + b \times \alpha, \tag{2.14}$$

where $V(1;\alpha)$ is an absolute magnitude at a phase angle of α. They showed that the surge slopes were different among taxonomic classes and had positive correlations with colors.

We estimated the surge slope of each asteroid type at $\alpha \leq 1^\circ$ using the phase parameters a and b obtained by Belskaya & Shevchenko (2000). Though it is known that a phase curve of TNOs appears an exponential (non-linear) surge at phase angle below 0.1° – 0.2° (Belskaya et al., 2003), we ignored this effect because our data were taken at $\alpha > 0.5^\circ$. Because the

increase of magnitude from $\alpha = 1^\circ$ to 0° is represented by $V(1;0) - V(1;1)$, the slope is calculated from $S = a/2 - b$. The mean slopes are $S = 0.143 \pm 0.021$ mag deg^{-1} for 9 S-type asteroids, $S = 0.032 \pm 0.033$ mag deg^{-1} for 10 C-type asteroids.

Schaefer et al. (2010) measured the surge slopes for 9 JTs. The slopes derived from linear-line fitting for $\alpha \leq 2^\circ$ distributed from -0.01 mag deg^{-1} to 0.09 mag deg^{-1} with the mean value of 0.04 mag deg^{-1}. The phase-curve shapes of 52 distant bodies of TNOs, Centaurs, and planetary satellites were given by Schaefer et al. (2009). Here we adopted the definition of Rabinowitz (2007) that TNOs consist of bodies with perihelion $q > 19.2$ AU and semi-major axis $a > 30.1$ AU, while Centaurs consist of bodies with 5.2 AU $< q <$ 19.2 AU. Rabinowitz (2007) determined the phase-curve slopes S_0 at zero phase angle and S_1 at $\alpha = 1^\circ$. We used the latter for comparison with our data. Also, we added the data of surge slopes at $\alpha < 2^\circ$ for two TNOs (1996 GQ21 and 2001 CZ31) measured by Sheppard & Jewitt (2002).

Using these data, we found that $S = 0.16 \pm 0.04$ mag deg^{-1} for small TNOs less than 800 km in diameter, $S = 0.10 \pm 0.05$ mag deg^{-1} for Centaurs, $S = 0.05 \pm 0.04$ mag deg^{-1} for JTs, $S = 0.05 \pm 0.02$ mag deg^{-1} for Jupiter's regular satellites, $S = 0.12 \pm 0.15$ mag deg^{-1} for Saturn's regular satellites, $S = 0.06 \pm 0.02$ mag deg^{-1} for Uranus's regular satellites, and $S = 0.15 \pm 0.03$ mag deg^{-1} for a Neptune's irregular satellite, Nereid. The wide spread for the Satunian satellites is caused by the large slopes of Enceladus ($S = 0.36$ mag deg^{-1}) and Iapetus($S = 0.17$ mag deg^{-1}). The large mean surge of the Satunian satellites compared to the other satellites is also due to these two objects with extremely-steep surges. When the two satellites are excluded, the mean surge slope is S=0.03 mag deg^{-1}. This value is consistent with the other regular satellites.

Figure 2.29 shows the perihelion–surge diagram for TNOs, Centaurs, JTs, and planetary satellites. The Centaurs, JTs, and regular satellites have indistinguishable surge distributions, except a few objects. For the mean surge slope, TNOs are evidently different from the other populations. This char-

acteristic distribution supports the indication given by the color distribution that Centaurs and JTs have a common surface property. Two Centaurs with steep surges ($S \approx 0.18$ mag deg^{-1}) have red surfaces with $B - R > 0.8$ (see Figure 2.30), which show indistinguishable surface properties from TNOs. Additionally, the regular satellites, except for Iapetus with $S \approx 0.17$ mag deg^{-1}, have similar surge properties to Centaurs and JTs.

We found that Sycorax and Prospero have own surge slopes, $S = 0.03$ mag deg^{-1} and $S = 0.14$ mag deg^{-1}, respectively, indicating different surface properties. Sycorax has a surge slope similar to JTs and regular satellites. In contrast, Prospero has a different slope from regular satellites, but similar to TNOs, Nereid, and S-type asteroids.

5.2 Colors of TNOs and Centaurs

Color-color diagrams of TNOs and Centaurs with the optical $BVRI$ bands measured by Doressoundiram (2008) showed that Centaurs have gray colors which are distant from the red colors of most TNOs. According to the color measurements by Tegler et al. (2003), Centaurs have bimodal color distribution, major gray-color ($B - R \approx 1.2$) populations and minor red-color ($B - R \approx 1.8$) populations. TNOs are also divided into two populations, dynamically cold population with small inclination and dynamically hot population with large inclination. The cold objects have red surfaces ($B - R >$ 1.5 mag), while the hot objects have gray surfaces ($B - R < 1.5$ mag).

The distinctive colors among TNOs and Centaurs indicate compositional differences in the surface layers. This fact is a significant evidence that they had own origins and/or experienced separate evolutionary processes. Various materials were detected from surface of small bodies in the outer Solar system, particularly H_2O ice and CH_4 ice. Previous spectroscopic observations for TNOs and Centaurs showed that they were identified four groups: CH_4-dominated, H_2O-ice-dominated, H_2O-ice with methanol-like, and featureless (organic-material-rich or carbon-rich?) objects (Barucci et al., 2008).

The red colors of icy bodies are believed to be induced by irradiation with energetic particles (Moroz et al., 2004). The surface reddening depends on the irradiation time and surface composition. The presence of organic materials accelerates the space weathering. Brunetto & Roush (2008) showed that irradiated CH_4-ice crusts mask the presence of H_2O-ice bands in the spectrum through laboratory experiments. Beyond a heliocentric distance of $\sim$40 AU, CH_4 metamorphoses from condensing in a H_2O-ice rich clathrate to condensing as pure CH_4. The pure CH_4 provides material inducing surface redding, even if there was substantial amount of CH_4 sublimation (Lewis, 1972). Therefore, objects located less than 40 AU from the Sun originally had gray surface due to the depletion of CH_4 before irradiated by sublimation. In contrast, objects beyond the 40 AU conserves CH_4 enough to induce surface reddening by irradiation. This scenario is consistent with the difference of color distributions between TNOs (especially the cold population) and Centaurs with gray color. The Centaurs with red color probably escaped from the outer region beyond 40 AU after long-time irradiation exposure.

5.3 Surge-Color Correlations

Schaefer et al. (2009) showed that the surge slope of TNOs and Centaurs positively correlates with the $B - I$ color. We confirmed the same correlation in the S vs. $B - V$ (Figure 2.30). Surge–color distribution is certainly an indicator for similarity of the surface composition which is basic information to investigate the primordial formation regions. We compared the surge–color distribution of the distant bodies with that of the observed satellites.

The color database for TNOs and Centaurs were published by Hainaut & Delsanti (2002). We obtained $B - V$ colors for 24 objects (Table 2.12). Figure 2.30 shows $B - V$ color versus surge slope of TNOs and Centaurs. Most of the TNOs have red colors and large slopes, while most of the Centaurs have gray colors and small slopes. The distribution between TNOs and Centaurs is significantly distinguished from each other, which indicates that

they have proper surface properties. Each of the two populations appears to have no correlation between color and surge slope. The colors of Sycorax and Prospero were given by Grav et al. (2004) and Maris et al. (2007), which were not consistent with each other. We used the both values for this comparison. Prospero is located around the median center between TNOs and Centaurs. Sycorax also has a similar-intermediate color between them, but it has a surge slope much less than the TNOs. We considered that Sycorax is similar to Centaurs, while Prospero is intermediate between TNOs and Centaurs in terms of the surge and color.

We performed the same comparison for other small-body populations, planetary satellites, JTs, and asteroids. Neese (2004) gives the $B - V$ colors for four Satunian regular satellites (Enceladus, Tethys, Dione, and Rhea), two Uranian regular satellites (Titania and Oberon), and a Neptunian irregular satellite Nereid. We excluded Enceladus from our sample because it has an unusual surge slope. The colors of the asteroids and JTs were obtained from the JPL Small-Body Database Search Engine[3]. The data of $B - V$ colors for 31 asteroids and 9 JTs were collected. Figures 2.31, 2.32, and 2.33 give the $B - V$ color versus surge slope distributions for the satellites, JTs, and asteroids, respectively. We found that Sycorax has a set of the color and surge slope similar to Satunian satellites and JTs. Also, Sycorax has an indistinguishable surge slope from the C-/P-type asteroids though the $B - V$ colors are distant from each other. In contrast, Prospero is located close to Nereid and S-type asteroids in the $B - V$ vs S diagram. The both satellites have different surges and colors from the Uranian regular satellites.

Figure 2.34 shows the surge vs. $B - V$ diagrams including all the sample of small-body populations. TNOs (except 1 object), two Centaurs, and Nereid have red colors enough to be clearly distinguished from the gray-colored bodies ($B - V \sim 0.88$ mag) including the other Centaurs, JTs, and regular satellites. This implies a tendency that the outer bodies with heliocentric distance larger than $\sim$30 AU have red surface while the inner bodies

[3]http://ssd.jpl.nasa.gov/sbdb_query.cgi

have gray surface. This is consistent with the mention in Section 5.2, i.e. distant objects contain sufficient CH_4 to induce surface reddening via the space weathering. The $B - V$ color of a small body is likely to be an indicator of the surface-temperature.

The surge slope possesses a positive correlation with the $B-V$ color that the red population have large S compared to the gray population. However, contrary to the $B - V$ colors, there is an overlapping region of the surge slope between TNOs and the Centaurs in $S = 0.10$–0.15 mag deg^{-1}. We found that a relationship between surge slope and inclination of the TNOs and Centaurs gives an explanation of the overlap of their colors. Figure 2.34 also shows an additional partitioning for TNOs and Centaurs into bodies with lower inclination than 15° and bodies with higher inclination than 15°. All of the low-inclination Centaurs and most of the high-inclination TNOs are located in the overlap region ($S = 0.10$–0.15 mag deg^{-1}), while none of the other TNOs and Centaurs lie in this region. All of the high-inclination Centaurs have surge slopes smaller than low-inclination Centaurs. On the contrary, the surge slopes of the low-inclination TNOs excluding two objects are larger than those of the high-inclination TNOs.

We could classify the small bodies into three categories based on the surge slope:

- Low-surge population with $S < 0.10$ mag deg^{-1} consists of the JTs, regular satellites, and high-inclination Centaurs.
- Mid-surge population with 0.10 mag deg^{-1} $< S < 0.15$ mag deg^{-1} consists of the low-inclination Centaurs and high-inclination TNOs.
- High-surge population with $S > 0.15$ mag deg^{-1} consists of the low-inclination TNOs.

It is notable that Sycorax belongs to the low-surge population, while Prospero is placed in the mid-surge population. If the both satellites were derived from captured Centaurs, it is most likely that Prospero was originated from

low-inclination Centaurs and Sycorax was originated from high-inclination Centaurs.

5.4 Origins and Evolutions of Sycorax and Prospero

We present the perihelion-inclination diagram of the Centaurs and TNOs in Figure 2.35 to understand the inclination distributions of the surge populations. The surge slope of each object is represented as the symbol size. It is possible to divide the diagram field with respect to the surge slopes into four regions: inner low-inclination, inner high-inclination, outer low-inclination, outer high-inclination.

The mean surge slopes of these regions and JTs are

$$
\begin{aligned}
S_{\mathrm{mean}} &= 0.05 \pm 0.03 \text{ mag deg}^{-1} && \text{in the inner low-inclination region,} \\
S_{\mathrm{mean}} &= 0.14 \pm 0.03 \text{ mag deg}^{-1} && \text{in the inner high-inclination region,} \\
S_{\mathrm{mean}} &= 0.20 \pm 0.03 \text{ mag deg}^{-1} && \text{in the outer low-inclination region,} \\
S_{\mathrm{mean}} &= 0.14 \pm 0.03 \text{ mag deg}^{-1} && \text{in the outer high-inclination region,} \\
S_{\mathrm{mean}} &= 0.04 \pm 0.04 \text{ mag deg}^{-1} && \text{in the JTs.}
\end{aligned}
$$

It indicates a similar surge slope between the inner low-inclination population and JTs. Also, the inner high-inclination population and the outer high-inclination population have a common surge.

These relationships correspond to the surge categories defined in Section 5.3. Figure 2.36 is the same diagram as 2.35 but each object is color-coded according to the surge categories. We found that all the mid-surge objects including the low-inclination Centaurs and high-inclination TNOs are distributed on an upward area with perihelion. Highly-inclined orbits were formed through dynamical excitation due to the gravitational perturbations by the planets or planetary embryos during the final stage of the planet formation (Petit et al., 2002). We considered that the mid-surge area indicated a dynamically-evolutionary path of planetesimals in the giant planet region. It means that the high-inclination TNOs have a common origin with the

low-inclination Centaurs and migrated outward from the primordial region with the increasing inclinations.

This scenario well agrees with the previous evolution models of high-inclination TNOs. Levison & Stern (2001) showed that the high-inclination TNOs have a larger fraction of large-size bodies (with a few km in radius) than low-inclination TNOs. They suggested that the high-inclination TNOs were formed in closer regions to the Sun and were transported outward. According to the model presented by Gomes (2003), the outward migration of Neptune caused by energy and angular momentum exchange with planetesimals (Malhotra, 1995) induced the transportation from the planetesimals inside Neptune's orbit to the TNO region. The low-inclination TNOs also must have been delivered from the region slightly interior to the current orbits, within $\sim$34 AU (Levison et al., 2008; Morbidelli et al., 2009).

Additionally, we suggest that the high-inclination Centaurs experienced orbital evolutions similar to the high-inclination TNOs, i.e. they were formed at the inner region of the present location and then migrated outward. The similarity of the surge slope between the high-inclination Centaurs and JTs supports this idea.

The above discussion gives the following implications

- The high-inclination Centaurs and JTs were originated from the region around 5–10 AU from the Sun.
- The low-inclination Centaurs and high-inclination TNOs were originated from the region around 10–20 AU from the Sun.
- The low-inclination TNOs were originated from the region around 20–35 AU from the Sun.

The distribution of the small bodies shown in Figure 2.36 is explained by this scenario.

Figure 2.36 also shows that the both of the low- and mid-surge populations lie across the Uranus's orbit. This accounts for our result that Uranus

has irregular satellites with different surge slopes. We regarded Sycorax with $S = 0.03$ as a captured body from the low-surge population such as high-inclination Centaurs. In contrast, Prospero with $S = 0.14$ as a captured body from the mid-surge population such as low-inclination Centaurs. According to the above scenario, Sycorax and Prospero were originally formed around 5–10 AU and 10–20 AU, respectively. In other words, Sycorax was derived from a "native" body, while Prospero was an "immigration" from the interior to Uranus. The hypothesis that the irregular satellites were originated from the primordial TNO (i.e. low-inclination TNOs) was rejected because of the disagreement in the surge slopes. This means that the irregular satellites, at least Sycorax and Prospero, are survivors formed in the giant-planet region where there are only small number of small bodies and planetary satellites from the last stage of the planet formation processes. They probably include meaningful clues about the growth and outward migrations of giant planets, dynamical evolution of planetesimals around the planets, and surface compositions of the distant small bodies.

Finally, let us discuss whether main-belt asteroids are still candidates of the origins of Sycorax and Prospero. According to Figure 2.33, (i) Sycorax has indistinguishable surge from the C-/P-type asteroids but shows red color compared to the C-/P-type asteroids, (ii) Prospero's surge and color agree with those of the S-type asteroids. If Sycorax were transported from the main-belt region, there is no reason to change the $B - V$ color into the redder. The different colors deny a connection between Sycorax and C-/P-asteroids. In contrast, we cannot reject the possibility that Prospero was derived from the S-type asteroids. According to the numerical simulations, main-belt asteroids can be delivered beyond the Jupiter/Saturn (Higuchi et al., 2010). The spectrum of Prospero should be obtained to be specified its birthplace.

Our discussion in this thesis was based on the orbital parameters (perihelion and inclination), colors, and surge slopes. To examine the evolutionary

scenario of the small bodies we suggested, other evidences are required, e.g. size distribution. We plan to perform extended wide-field surveys for the small Solar system bodies using a next generation prime focus camera of the Subaru Telescope, Hyper Suprime-Cam (HSC; Komiyama et al., 2004; Miyazaki et al., 2006). HSC has a 1.5 degree diameter field-of-view (1.8 deg^2), seven times larger than the Suprime-Cam. It makes possible to explore sparse objects distributed across the wide field of the sky. We are working on an observing program targeted at high-inclination small bodies including TNOs and Centaurs with a method similar to our survey for high-inclination asteroids mentioned in Part I. We can obtain the unknown size distributions of high-inclination TNOs and Centaurs down to 50 km in diameter via the observation data by HSC. HSC is scheduled for completion in 2011 and the strategic survey program with HSC will be started from 2012. We believe significant contributions of this survey project to understand the formations and evolutions of the planets and small bodies in the Solar system.

6 CONCLUSION

We performed wide-field photometric observations for Uranian irregular satellites using the 8.2-m Subaru Telescope with the Suprime-Cam. The collected data contained seven irregular satellites: Caliban, Sycorax, Prospero, Setebos, Stephano, Trinculo, and Francisco. As the result of data reduction with the color and airmass corrections, the significant brightness variations were confirmed for four objects. We carried out the period analyses and found the periods of brightness variations (corresponding to a half of the rotation period) 5.4 hr or 7.1 hr for Caliban, 3.5 hr for Sycorax, 4.6 hr or 5.9 hr for Prospero, and 2–15 hr for Stephano. Their rotational period-diameter distribution is consistent with that of asteroids and trans-Neptunian objects (TNOs).

Sycorax and Prospero showed clear lightcurves in all of the observation nights enough to measure the slopes of the lightcurves around 1° phase angle. The surge slopes were determined as 0.03 mag deg^{-1} for Sycorax and 0.14 ± 0.03 mag deg^{-1} for Prospero. It is interesting that they have distinct difference of surge slope, indicating heterogeneity of surface properties between them. We also obtained the data of the surge slope and $B-V$ color for TNOs, Centaurs, Jovian Trojans (JTs), asteroids, and regular satellites.

Comparison of the surge slope distributions between the irregular satellites and the other populations indicates that Sycorax's surge is similar to those of Centaurs, JTs, and regular satellites. It also agreed with that of high-inclination (larger than 15°) Centaurs. Prospero has a surge slope consistent with low-inclination Centaurs and high-inclination TNOs. The results indicate that Sycorax was a captured body from the local planetesimals, while Prospero was derived from the region interior to Uranus's orbit, probably the Jupiter–Saturn zone.

Acknowledgment

I really thank associate Prof. Yoichi Itoh for kindly supervising my work. I am grateful to Prof. David Jewitt for giving me the observational data for the irregular satellites of Uranus and the opportunity of my three-month stay in University of California, Los Angeles (UCLA). I thank emeritus Prof. Tadashi Mukai and associate Prof. Akiko Nakamura for giving helpful advices. I am grateful Dr. Fumi Yoshida, Dr. Takashi Ito, Dr. Shinsuke Abe, Dr. Daisuke Kinoshita, Dr. Shigeru Takahashi, Dr. Seitaro Urakawa, Dr. Arika Higuchi, Dr. Patryk S. Lykawka, Prof. Wing-Huen Ip, and Prof. Junichi Watanabe. This work was based on data collected at Subaru Telescope, which is operated by the National Astronomical Observatory of Japan (NAOJ). I am supported by the Grant-in-Aid from Japan Society for the Promotion of Science. Finally, I am grateful to my parents and my colleagues in Kobe University and UCLA.

References

Astakhov, S. A., Burbanks, A. D., Wiggins, S, & Farrelly, D. 2003, Nature, 423, 264

Baba, H., Yasuda, N., Ichikawa, S., Yagi, M., Iwamoto, N., Takata, T., Horaguchi, T., Taga, M., Watanabe, M., Ozawa, T., & Hamabe, M. 2002, ASP Conf. Vol. 281, Astronomical Data Analysis Software and Systems XI, ed. D. A. Bohlender, D. Durand, & T. H. Handley (San Francisco, CA: ASP), 298

Barucci, M. A., Brown, M. E., Emery, J. P., & Merlin, F. 2008, in The Solar System Beyond Neptune, ed. M. A. Barucci, H. Boehnhardt, D. P. Cruikshank, and A. Morbidelli (Tucson: University of Arizona Press), 143

Belskaya, I. N. & Shevchenko, V. G. 2000, Icarus, 147, 94

Belskaya, I. N., Barucci, A. M., & Shkuratov, Y. G. 2003, Earth, Moon, and Planets, 92, 201

Benz, W., & Asphaug, E. 1999, Icarus, 142, 5

Bertin, E., & Arnouts, S. 1996, Astronomy and Astrophysics Supplement, 117, 393

Bottke, W. F., Durda, D. D., Nesvorný, D., Jedicke, R., Morbidelli, A., Vokrouhlický, D., & Levison, H. 2005, Icarus, 175, 111.

Bottke, W. F., Durda, D. D., Nesvorný, D., Jedicke, R., Morbidelli, A., Vokrouhlický, D., & Levison, H. F. 2005, Icarus, 179, 63

Bottke, W. F., Morbidelli, A., Jedicke, R., Petit, J.-M., Levison, H. F., Michel, P., & Metcalfe, T. S. 2002, Icarus, 156, 399

Bottke, W. F., Nolan, M. C., Greenberg, R., & Kolvoord, R. A. 1994, Icarus, 107, 255

Bowell, E 2001, the asteroid orbital elements database, ASTORB (Flagstaff: Lowell Observatory)

Bowell, E., Hapke, B., Domingue, D., Lumme, K., Peltoniemi, J., & Harris, A. W. 1989, in Asteroids II, ed. R. P. Binzel, T. Gehrels, and M. S. Matthews (Tucson: University of Arizona Press), 524

Bowell, E., Skiff, B. A., Wasserman, L. H., & Russel, K. S. 1990, Asteroids, comets, meteors III, ed. C. I. Lagerkvist, H. Rickman, and B. A. Lindblad (Uppsala: Uppsala Universitet), 19

Britt, D. T., Yeomans, D., Housen, K., & Consolmagno, G. 2002, in Asteroids III, ed. W. F. Bottke Jr., A. Cellino, P. Paolicchi, and R. P. Binzel (Tucson: University of Arizona Press), 485

Brunetto, R. & Roush, T. L. 2008, Astronomy and Astrophysics, 481, 879

Bus, S. J., & Binzel, R. P. 2002, Icarus, 158, 146

Cellino, A., Zappala, V., & Farinella, P. 1991, Monthly Notices of the Royal Astronomical Society, 253, 561.

Colombo, G. & Franklin, F. A. 1971, Icarus, 15, 186.

Davis, D. R., Ryan, E. V., Farinella, P. 1994, Planetary and Space Science, 42, 599.

Dermawan, B. 2003, "CYCLOCODE Period Searching & Lightcurve Fitting Program; Ver. 3.6", http://www.toybox.gr.jp/mp366/lightcurve/cyclocode/cyclocode_doc_eng.pdf

Dohnanyi, J. S. 1969, Journal of Geophysical Research, 74, 2531.

Doressoundiram, A., Boehnhardt, H., Tegler, S. C., & Trujillo, C. 2008, in The Solar System Beyond Neptune, ed. M. A. Barucci, H. Boehnhardt, D. P. Cruikshank, and A. Morbidelli (Tucson: University of Arizona Press), 91

Drilling, J. S. & Landolt, A. U. 2000, in Allen's Astrophysical Quantities, ed. A. N. Cox (New York: AIP Press), 381

Durda, D. D., Greenberg, R., & Jedicke, R. 1998, Icarus, 135, 431

Evans, R. W., Stapelfeldt, K. R., Peters, D. P., Trauger, J. T., Padgett, D. L., Ballester, G. E., Burrows, C. J., Clarke, J. T., Crisp, D., Gallagher, J. S., Griffiths, R. E., Grillmair, C., Hester, J. J., Hoessel, J. G., Holtzmann, J., Krist, J., McMaster, M., Meadows, V., Mould, J. R., Ostrander, E., Sahai, R., Scowen, P. A., Watson, A. M., Westphal, J. 1998, Icarus, 131, 261.

Farinella, P., & Davis, D. R. Icarus, 97, 111

French, R. G., Verbiscer, A., Salo, H., McGhee, C., & Dones, L. 2007, Publications of the Astronomical Society of the Pacific, 119, 623

Fukugita, M., Ichikawa, T., Gunn, J. E., Doi, M., Shimasaku, K., & Schneider, D. P. 1996, Astronomical Journal, 111, 1748

Gaffy, M. J., Burbine, T. H., & Binzel, R. P. 1993, Meteoritics, 28, 161

Gil-Hutton, R. 2006, Icarus, 183, 93

Gladman, B. J., Davis, D. R., Neese, C., Jedicke, R., Williams, G., Kavelaars, J. J., Petit, J.-M., Scholl, H., Holman, M., Warrington, B., Esquerdo, G., & Tricarico, P. 2009, Icarus, 202, 104

Gomes, R. S. 2003, Icarus, 161, 404

Gomes, R., Levisonm, H. F., Tsiganis, K., & Morbidelli, A. 2005, Nature, 435, 466

Grav, T., Holman, M. J., & Kavelaars, J. J. 2003, Astrophysical Journal, 591, L71

Grav, T., Holman, M. J., & Fraser, W. C. Astrophysical Journal, 613, L77

Hainaut & Delsanti 2002, Astronomy and Astrophysics, 389, 641

Hayashi, C. 1981, Progress of Theoretical Physics Supplement, 70, 35.

Heppenheimer, T. A. & Porco, C. 1977, Icarus, 30, 385

Higuchi, A., Okamoto, T., & Ida, S. 2010, in Asia Oceania Geosciences Society 2010 (held 5–9 July in Hyderabad, India), PS12-A013

Holsapple, K. A. 2007, Icarus, 187, 500

Ivezić, Ž., Jurić, M., Lupton, R. H., Tabachnik, S. & Quinn, T. (the SDSS Collaboration) 2002, Proceedings of the SPIE, 4836, 98

Ivezić, Ž., Tabachnik, S., Rafikov, R., Lupton, R. H., Quinn, T., Hammergren, M., Eyer, L., Chu, J., Armstrong, J. C., Fan, X., Finlator, K., Geballe, T. R., Gunn, J. E., Hennessy, G. S., Knapp, G. R., Leggett, S. K., Munn, J. A., Pier, J. R., Rockosi, C. M., Schneider, D. P., Strauss, M. A., Yanny, B., Brinkmann, J., Csabai, I., Hindsley, R. B., Kent, S., Lamb, D. Q., Margon, B., McKay, T. A., Smith, J. A., Waddel, P., & York, D. G., for the SDSS Collaboration 2001, Astronomical Journal, 122, 2749

Jedicke, R. 1996, Astronomical Journal, 111, 970

Jedicke, R., & Metcalfe, T. S. 1998, Icarus, 131, 245

Jutzi, M., Michel, P., Benz, Wi., Richardson, D. C., 2010, Icarus, 207, 54

Jewitt, D. & Haghighipour, N. 2007, Annual Review of Astronomy & Astrophysics, 45, 261

Jewitt, D., Luu, J., & Chen, J. 1996, Astronomical Journal, 112, 1225

Kadono, T., Sakaiya, T., Hironaka, Y., Otani, K., Sano, T., Fujiwara, T., Mochiyama, T., Kurosawa, K., Sugita, S., Sekine, Y., Nishikanbara, W., Matsui, T., Ohno, S., Shiroshita, A., Miyanishi, K., Ozaki, N., Kodama,

R., Nakamura, A. M., Arakawa, M., Fujioka, S., & Shigemori, K. 2010, Journal of Geophysics Research, 115, E04003

Knežević, Z., Milani, A., Farinella, P., Froeschle, Ch., Froeschle, Cl. 1991, Icarus, 93, 316

Komiyama, Y., Miyazaki, S., Nakaya, H., Furusawa, H. & Takeshi, K. 2004, SPIE, 5492, 525

Lazzaro, D., Angeli, C. A., Carvano, J. M., Mothe'-Diniz, T., Duffard, R., & Florczak, M. 2004, Icarus, 172, 179

Landolt, A. U., Astronomical Journal, 104, 340

Levison, H. F. & Stern, A. 2001, Astronomical Journal, 121, 1730.

Levison, H. F., Morbidelli, A., Vanlaerhoven, C., Gomes, R., & Tsiganis, K. 2008, Icarus 196, 258

Levison, H. F., Bottke, W. F., Gounelle, M., Morbidelli, A., Nesvorný, D., & Tsiganis, K. 2009, Nature, 460, 364.

Lewis, J. S. 1972, Icarus, 16, 241

Livingston, W. C. 2000, in Allen's Astrophysical Quantities, ed. A. N. Cox (New York: AIP Press), 339

Lomb, N. R. 1976, Astrophysics and Space Science, 39, 447

Malhotra, R. 1995, Astronomical Journal, 110, 420.

Maris, M., Carraro, G., Cremonese, G., & Fulle, M. 2001, Astronomical Journal,121, 2800

Maris, M., Carraro, G., & Parisi, M. G. 2007, Astronomy and Astrophysics, 472, 311

Mishchenko, M. I. 1993, Astrophysical Journal, 411, 351

Miyazaki, S., Komiyama, Y., Sekiguchi, M., Okamura, S., Doi, M., Furusawa, H., Hamabe, M., Imi, K., Kimura, M., Nakata, F., Okada, N., Ouchi, M., Shimasaku, K., Yagi, M., & Yasuda, N. 2002, Publications of the Astronomical Society of Japan, 54, 833

Miyazaki, S., Komiyama, Y., Nakaya, H., Doi, Y., Furusawa, H., Gillingham, P., Kamata, Y., Takeshi, K. & Nariai, K. 2006, Proc. SPIE, 6269, 9

Moroz, L., Baratta, G., Strazzulla, G., Starukhina, L., Dotto, E., Barucci, M. A., Arnold, G., & Distefano, E. 2004, Icarus, 170, 214

Mosqueira, I. & Estrada, P. R. 2003, Icarus, 163, 198

Mothé-Diniz, T., Carvano, J. M., & Lazzaro, D. 2003, Icarus, 162, 10

Morbidelli, A, Levison, H. F., Bottke, W. F., Dones, L., Nesvorný, D. 2009, Icarus, 202, 310.

Morbidelli, A, Levison, H. F., Tsiganis, K., & Gomes, R. 2005, Nature, 435, 462.

Muinonen, K., Piironen, J., Shkuratov, Y. G., Ovcharenko, A., & Clark, B. E. 2002, in Asteroids III, ed. W. F. Bottke Jr., A. Cellino, P. Paolicchi, and R. P. Binzel (Tucson: University of Arizona Press), 123

Nakamura, T., & Yoshida, F. 2002, Publications of the Astronomical Society of Japan, 54, 1079

Neese, C. 2004, in EAR-SA-COMPIL-3-SATELLITE-COLOR-V1.0, NASA Planetary Data System (http://sbn.psi.edu/pds/resource/satcol.html)

Nelson, R. M., Hapke, B. W., Smythe, W. D., & Spilker, L. J. 2000, Icarus, 147, 545

Newberry, M. V. 1991, Publications of the Astronomical Society of the Pacific, 103, 122

O'Brien, D. P., & Greenberg, R. 2003, Icarus, 164, 334

O'Brien, D. P., & Greenberg, R. 2005, Icarus, 178, 179

Ouchi, M., Shimasaku, K., Okamura, S., Furusawa, H., Kashikawa, N., Ota, K., Doi, M., Hamabe, M., Kimura, M., Komiyama, Y., Miyazaki, M., Miyazaki, S., Nakata, F., Sekiguchi, M., Yagi, M., & Yasuda, N. 2004, Astrophysical Journal, 611, 660

Petit, J.-M., Chambers, J., Franklin, F., & Nagasawa, M. 2002, in Asteroids III, ed. W. F. Bottke Jr., A. Cellino, P. Paolicchi, and R. P. Binzel (Tucson: University of Arizona Press), 711

Peixinho, N., Lacerda, P., & Jewitt, D. 2008, Astronomical Journal, 136, 1837

Pollack, J. B., Burns, J. A., & Tauber, M. E. 1979, Icarus, 37, 587.

Rabinowitz, D. L., Schaefer, B. E., & Tourtellotte, S. W. 2007, Astronomical Journal, 133, 26

Scargle, J. D. 1982, Astrophysical Journal, 263, 835

Schaefer, B.E., Rabinowitz, D. L., & Tourtellotte, S. W. 2009, Astronomical Journal, 137, 129

Schaefer, B. E., Tourtellotte, S. W., Rabinowitz, D. L., & Schaefer, M. W. 2008, Icarus, 196, 225

Schaefer, M. W., Schaefer, B.E., Rabinowitz, D. L., & Tourtellotte, S. W. 2010, Icarus, 207, 699

Sheppard, S. S. & Jewitt, D. C. 2002, Astronomical Journal, 124, 1757

Sheppard, S., Jewitt, D., & Kleyna, J. 2005, Astronomical Journal, 129, 518

Shkuratov, Y., Ovcharenko, A., Zubko, E., Miloslavskaya, O., Muinonen, K., Piironen, J., Nelson, R., Smythe, W., Rosenbush, V., & Helfenstein, P. 2002, Icarus, 159, 396

Stevenson, D. J., Harris, A. W., & Lunine, J. I. 1986, in Satellites, ed. J. A. Burns and M. S. Matthews (Tucson: University of Arizona Press), 39

Tedesco, E. F., Noah, P. V., Noah, M., & Price, S. D. 2002, Astronomical Journal, 123, 1056

Terai, T., Itoh, Y., & Mukai, T. 2007, Publications of the Astronomical Society of Japan, 59, 1175

Tegler, S. C., Romanishin, W., & Consolmagno, G. J. 2003, Astrophysical Journal, 599, L49

Trujillo, C. A. & Brown, M. E. 2002, ApJ, 566, L125

Tsiganis, K., Gomes, R., Morbidelli, A., & Levison, H. F. 2005, Nature, 435, 460

Van Houten, C. J., Herget, P., & Marsden, B. G. 1984, Icarus, 59, 1

Vedder, J. D. 1998, Icarus, 131, 283

Vieira Neto, E., & Winter, O. C. 2001, AJ, 122, 440

Welch, B. L. 1938, Biometrika, 29, 350

Wiegert, P., Balam, D., Moss, A., Veillet, C., Connors, M., & Shelton, I. 2007, Astronomical Journal, 133, 1609

Yagi, M., Kashikawa, N., Sekiguchi, M., Doi, M., Yasuda, N., Shimasaku, K., & Okamura, S. 2002, Astronomical Journal, 123, 66

Yoshida, F., & Nakamura, T. 2007, Planetary Space Science, 55, 1113

Yoshida, F., Nakamura, T., Watanabe, J., Kinoshita, D., Yamamoto, N., & Fuse, T. 2003, Publications of the Astronomical Society of Japan, 55, 701

Wald, A. & Wolfowitz, J. 1940, Annals of Mathematical Statistics, 11, 147

FIGURES and TABLES

Table 1.1: Observations with the Suprime-Cam on June 3, 2008 (UT).

Field	RA(J2000)	Dec(J2000)	β[1] (deg)	Obs. time (UT)
Field 1-1	16:39:00	+00:00:00	+21.9	10:46:58, 11:12:50
Field 1-2	16:36:00	+00:36:00	+22.4	10:52:02, 11:17:57
Field 1-3	16:47:10	+02:40:00	+24.8	10:57:07, 11:22:59
Field 1-4	16:49:25	+01:25:00	+23.7	11:02:40, 11:28:02
Field 2-1	16:51:10	+02:30:30	+24.8	11:33:04, 11:53:11
Field 2-2	16:53:00	+02:03:33	+24.4	11:38:07, 11:58:13
Field 2-3	16:52:30	+01:34:49	+23.9	11:43:08, 12:03:17
Field 2-4	16:52:35	+01:04:59	+23.5	11:48:08, 12:08:17
Field 3-1	16:53:00	+03:25:00	+25.8	12:13:18, 12:33:28
Field 3-2	16:55:30	+03:15:00	+25.7	12:18:22, 12:38:32
Field 3-3	16:55:30	+02:32:59	+25.0	12:23:23, 12:43:34
Field 3-4	16:55:30	+01:55:30	+24.4	12:28:27, 12:48:37
Field 4-1	17:00:28	+03:25:29	+26.0	12:53:40, 13:13:47
Field 5-1	17:02:30	+01:58:00	+24.6	13:34:00, 13:56:47

[1] Ecliptic latitude.

Table 1.2: The Suprime-Cam archival data used in this survey.

Field	RA(J2000)	Dec(J2000)	β[1] (deg)	Date (UT)	Obs. time (UT)	Exp. (sec)
SDA01	13:24:29	+27:46:13	+33.7	2002-04-11	06:49:10, 08:10:58	480
SDA02	13:24:33	+27:29:22	+33.4	2003-04-02	09:57:21, 10:51:20	480
SDA03	10:12:18	+46:56:40	+33.2	2004-02-17	08:03:01, 08:27:02	300
SDA04	08:49:46	+44:15:14	+25.5	2002-01-09	14:10:52, 14:17:32	280
SDA05	08:47:20	+44:15:15	+25.3	2002-01-09	14:24:05, 14:30:31	280
SDA06	08:49:46	+44:15:15	+25.5	2002-01-15	14:05:25, 14:12:15	280
SDA07	08:47:20	+44:15:15	+25.3	2002-01-15	14:19:01, 14:25:30	280
SDA08	21:53:40	+17:39:52	+28.5	2004-09-15	06:21:46, 06:49:48	500
SDA09	11:49:34	+22:23:42	+19.4	2005-03-05	08:37:07, 08:44:07	150
SDA10	07:02:42	+38:54:40	+16.2	2002-01-12	06:47:56, 07:11:58	600
SDA11	00:18:16	+16:17:40	+13.1	2003-09-27	08:23:14, 08:50:05	480
SDA12	22:18:21	+00:37:27	+10.4	2004-08-18	09:13:12, 09:31:14	480
SDA13	23:31:55	+00:10:38	+3.0	2003-09-28	05:26:50, 05:52:19	450
SDA14	23:34:03	+00:10:38	+2.7	2003-09-28	06:03:10, 06:28:40	450
SDA15	23:28:29	+00:08:39	+3.3	2003-09-28	06:38:23, 07:03:48	450
SDA16	00:22:53	+04:25:14	+1.8	2003-09-28	07:26:54, 07:52:16	450
SDA17	23:56:57	−00:59:31	−0.6	2004-09-16	08:17:16, 08:35:19	300
SDA18	23:01:27	−05:34:30	+0.6	2004-09-16	08:53:01, 09:20:15	480
SDA19	21:40:18	−23:40:51	−9.2	2003-07-27	11:18:13, 11:36:07	480
SDA20	07:50:50	+10:09:15	−10.7	2002-01-09	13:43:14, 13:49:47	280
SDA21	07:49:04	+10:09:15	−10.7	2002-01-09	13:56:17, 14:02:55	280
SDA22	07:50:49	+10:08:30	−10.7	2002-01-14	13:39:28, 13:46:16	280
SDA23	07:49:03	+10:08:30	−10.7	2002-01-14	13:53:34, 14:00:05	280
SDA24	02:18:03	−04:58:29	−17.7	2002-10-08	10:21:43, 10:39:37	480
SDA25	02:18:00	−05:25:00	−18.1	2002-11-02	11:05:01, 11:22:55	480
SDA26	02:18:00	−04:35:00	−17.3	2002-11-02	11:49:55, 12:07:50	480
SDA27	02:19:47	−05:00:00	−17.9	2002-11-03	12:22:08, 12:40:03	480
SDA28	02:16:21	−04:59:00	−17.6	2002-11-03	13:26:36, 13:53:41	480

[1] Ecliptic latitude.

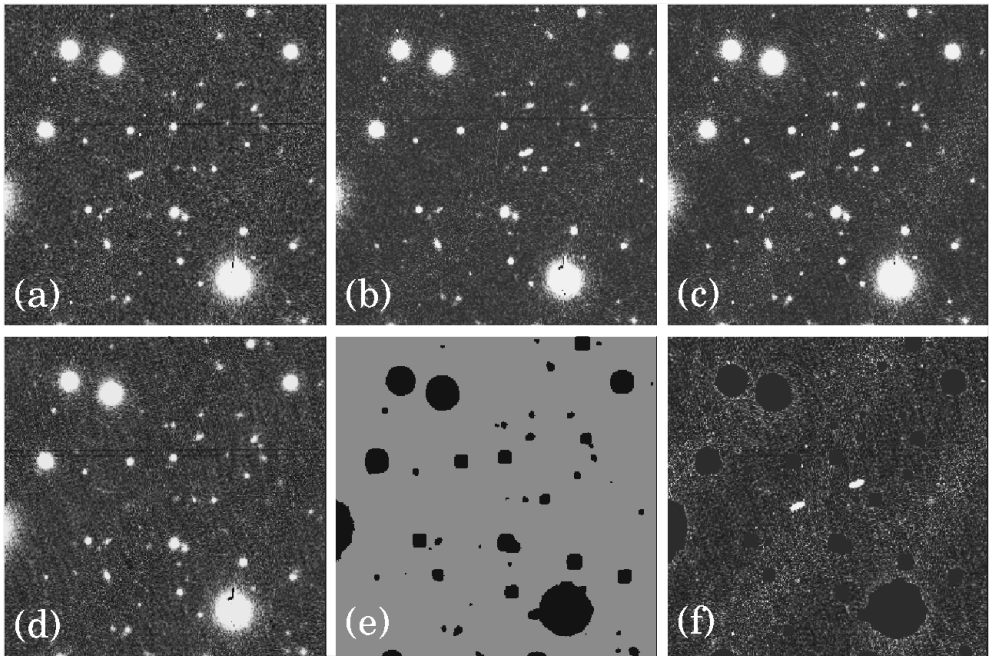

Figure 1.1: The procedures of data reduction for detecting moving objects (see text). (a) and (b) are a portion of the original r-band images taken at a 20-minute interval. (c) and (d) are the "OR" and "AND" images, respectively. (e) shows the mask image created from the AND image. (f) is the final processed image. The field stars and galaxies are eliminated and the moving object appears as two sources. The field-of-view of each image is $1' \times 1'$.

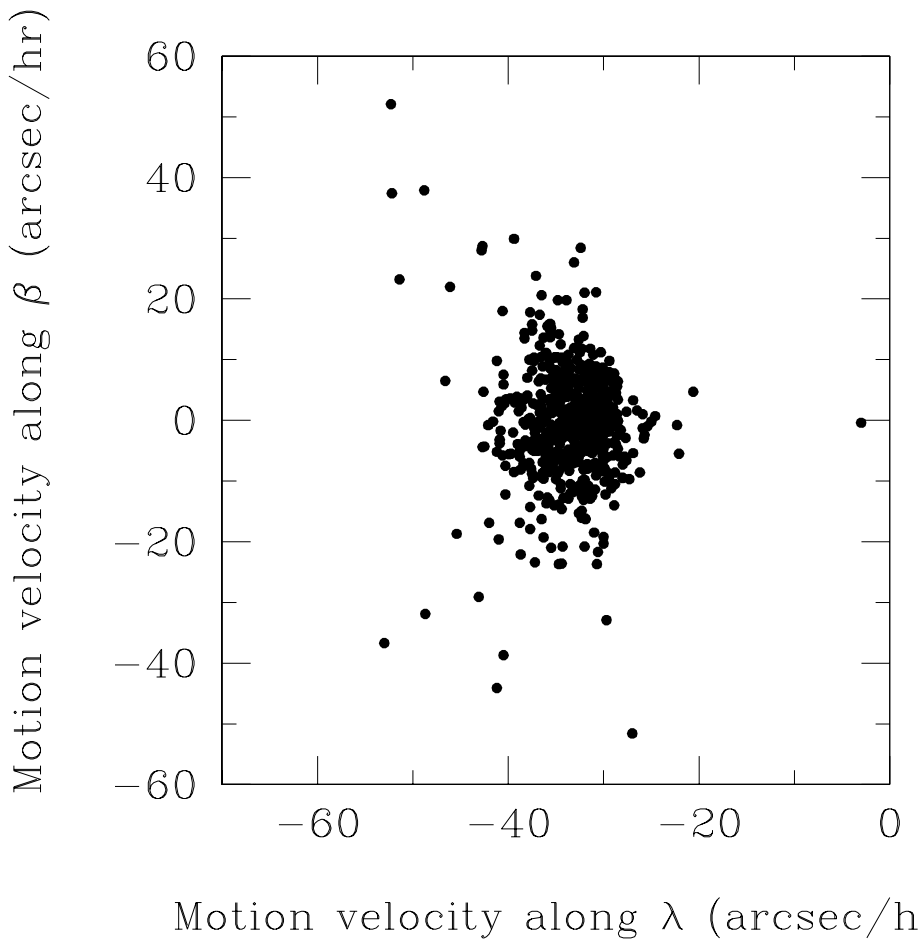

Figure 1.2: Ecliptic longitude (λ) and latitude (β) components of the apparent motions of the detected moving objects. The largest swarm consists of MBAs with low inclination. High-inclination MBAs are located away from 0 arcsec hr^{-1} of the β component. The point with low velocities corresponds to a trans-Neptunian object.

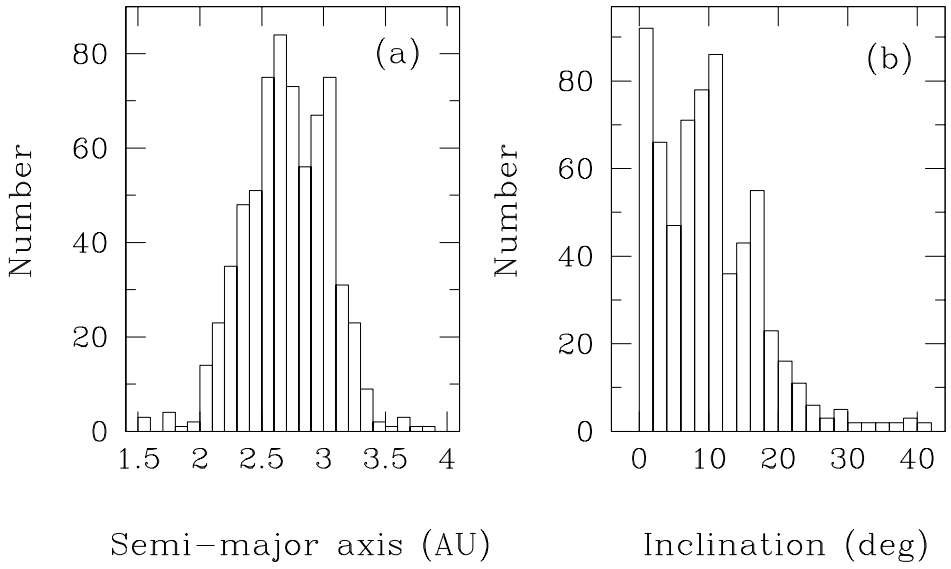

Figure 1.3: The distributions in semi-major axis (left) and inclination (right) of the detected moving objects.

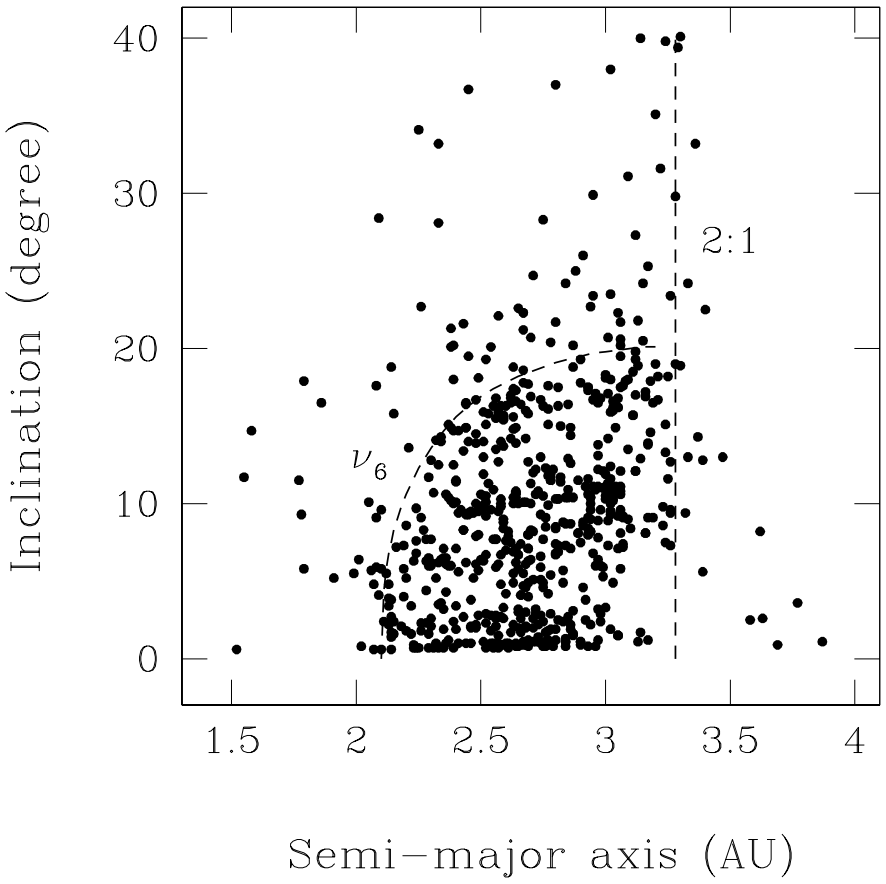

Figure 1.4: Semi-major axis vs. inclination distribution of the detected moving objects. The dashed vertical line shows the 2:1 mean motion resonance, and the dashed curve shows the ν_6 secular resonance.

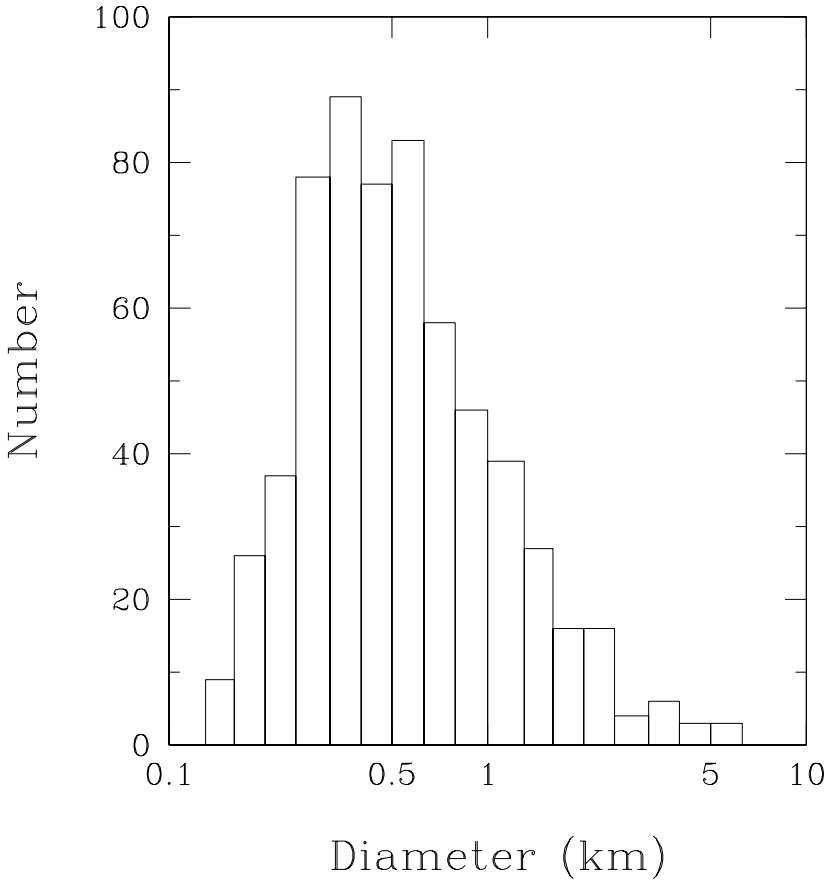

Figure 1.5: Diameter distribution of the detected MBAs. The horizontal axis is shown in logarithmic scale with a step of 0.1.

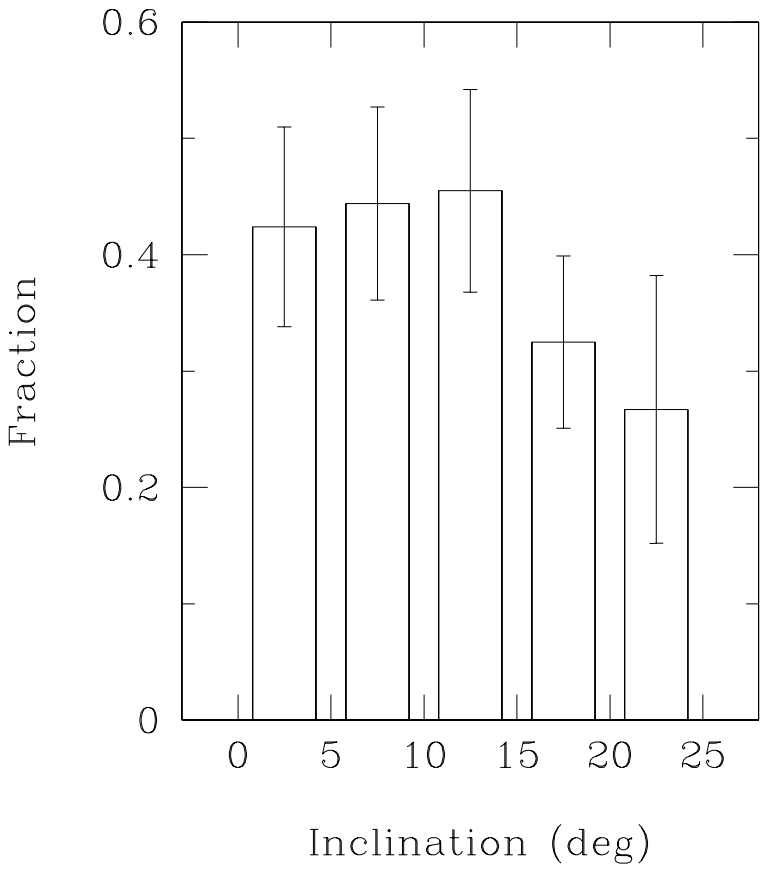

Figure 1.6: The fraction of MBAs smaller than 1 km in diameter. This drops steeply beyond 15°.

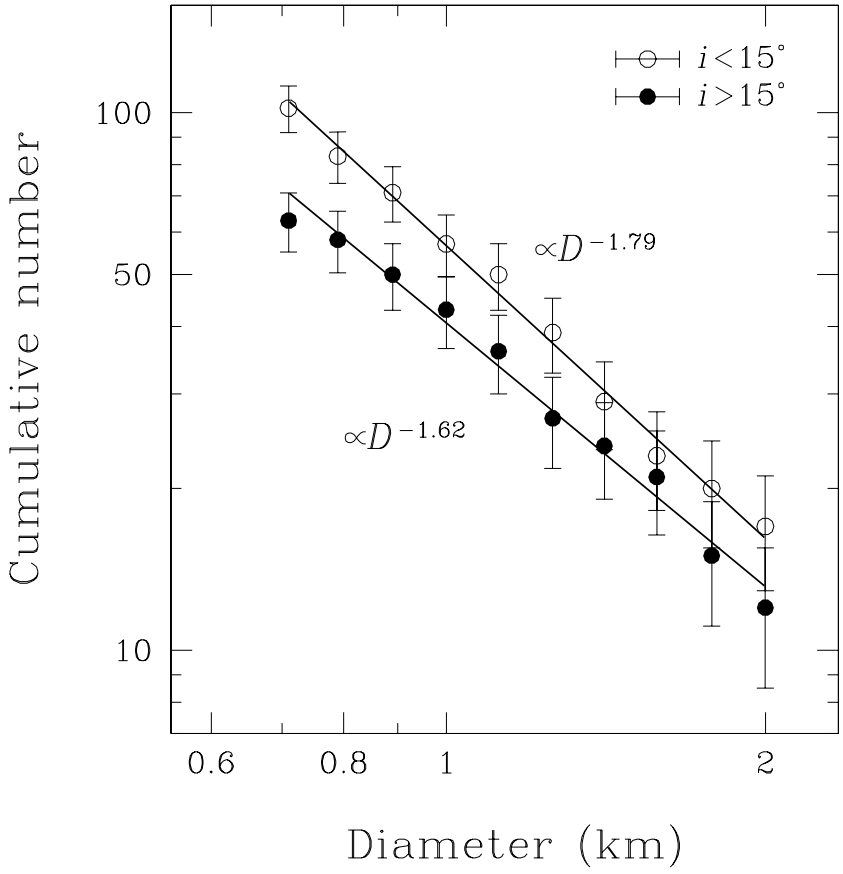

Figure 1.7: Cumulative size distributions (CSDs) of the MBA sample. The open circles show the CSD of low-i MBAs ($i < 15°$) and the filled circles show the CSD of high-i MBAs ($i > 15°$). The solid lines are fitted power laws of $N(> D) \propto D^{-b}$. The slope of the high-i CSD ($b = 1.62$) is smaller than that of the low-i CSD ($b = 1.79$).

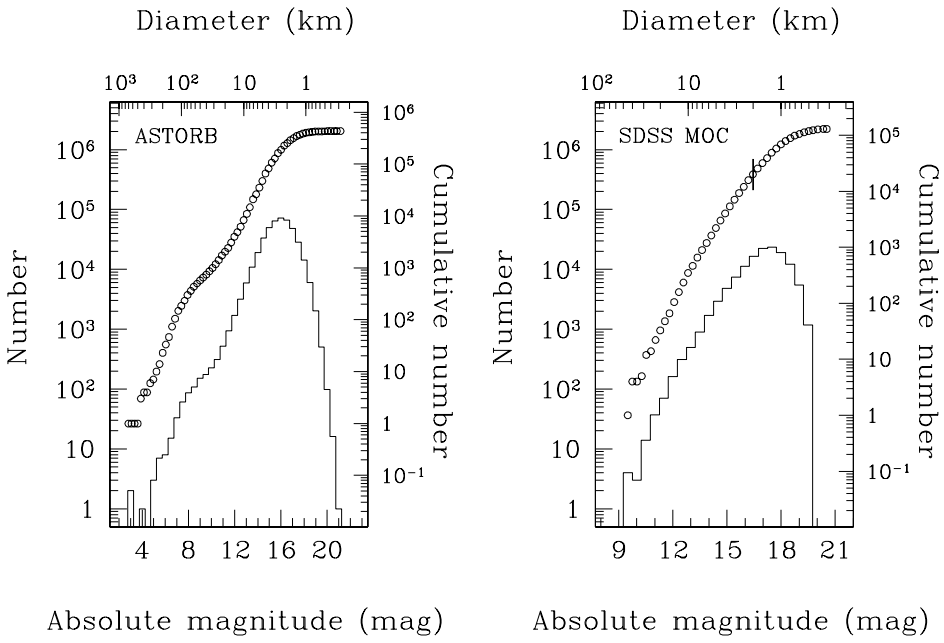

Figure 1.8: The absolute magnitude distributions (histogram) and the cumulative size distributions (open circles) obtained by the ASTORB database in the left and SDSS Moving Objects Catalog (SDSS MOC) in the right. The horizontal axes of absolute magnitude (bottom) and diameter (upper) do not exactly correspond with each other. The vertical bar in the panel of the SDSS MOC shows a detection limit of 2 km in diameter.

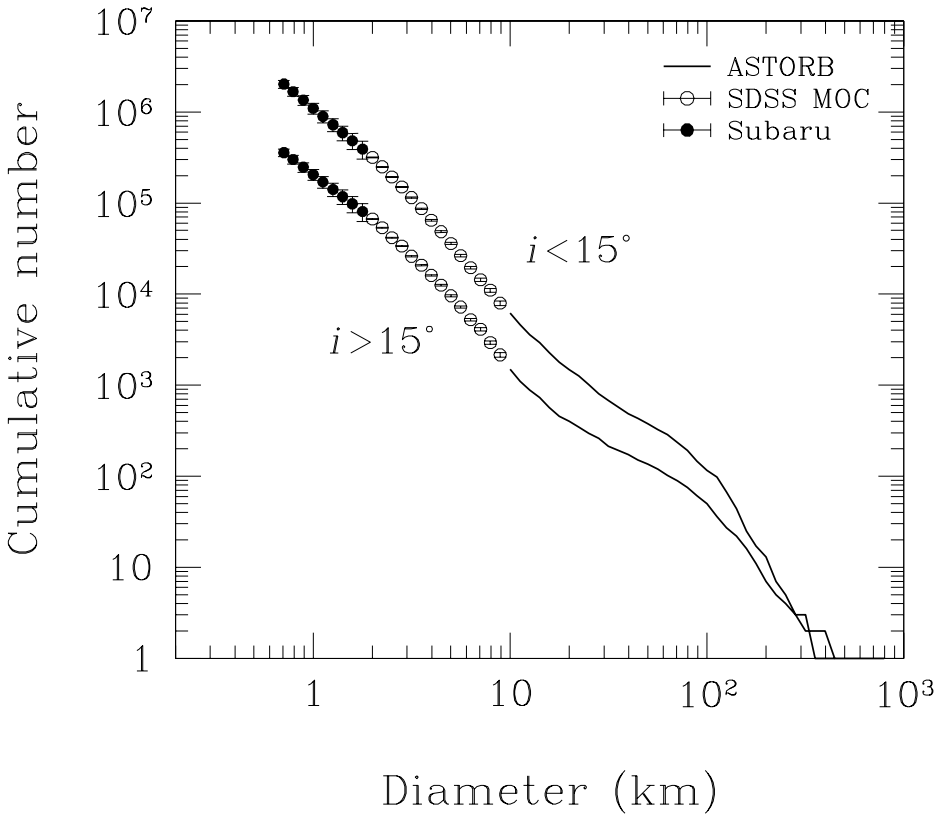

Figure 1.9: Combined CSDs of the low-i and high-i MBAs down to 0.7 km in diameter. The solid curves are the numbered MBA population in the ASTORB database, the open circles show the scaled CSDs based on the SDSS MOC, and the filled circles show the scaled CSDs based on the Subaru data. The high-i CSD is shallower than the low-i CSDs across the entire size range.

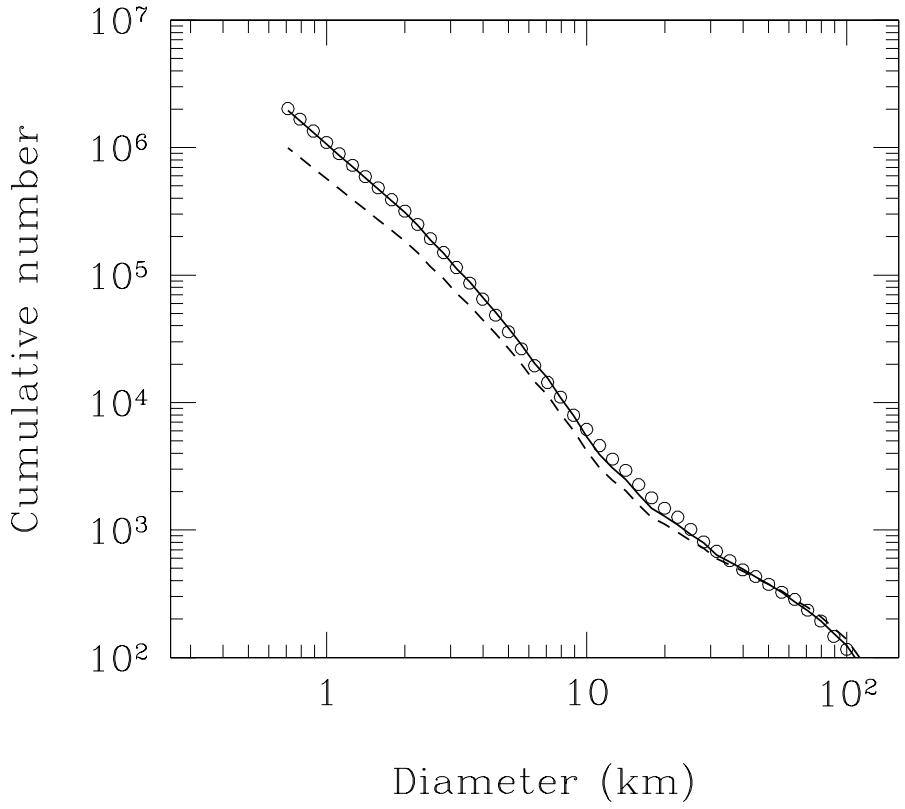

Figure 1.10: Comparison of the CSDs between low-i (open circles) and high-i MBAs (dashed line). The solid curve is the adjusted high-i CSD whose single-slope power-law index fit was transformed into the index of the low-i CSD. It coincides with the low-i CSD across the entire size range of less than 100 km in object diameter.

Table 1.3: The power-law indexes of the compounded CSDs from S-like and C-like MBAs.

	S/C [1]	$b_{\rm s}$ [2]	$b_{\rm c}$ [3]	b [4]
SDSS MOC				
low-i	0.67	2.66	2.41	2.49±0.02
high-i	0.56	2.26	2.36	2.32±0.04
Model 1				
low-i	0.67	2.66	2.41	2.50 [5]
high-i	0.56	2.66	2.41	2.49 [5]
Model 2				
low-i	0.67	2.66	2.41	2.50 [5]
high-i	0.67	2.26	2.36	2.32 [5]

[1] Population ratio of the S-like MBAs to the C-like MBAs.
[2] Power-law index of the CSD for S-like group.
[3] Power-law index of the CSD for C-like group.
[4] Power-law index of the summed CSD.
[5] The fitting error is $\ll 0.01$.

Table 2.1: Hill spheres and satellite number of the giant planets.

Planet	a_p[1] (AU)	r_H[2] (AU)	N[3]	N_r[4]	N_i[5]	$N_{i,pro}$[6]	$N_{i,ret}$[7]
Jupiter	5.20	0.35	63	8	55	6	49
Saturn	9.55	0.43	56	21	35	8	27
Uranus	19.22	0.47	27	18	9	1	8
Neptune	30.11	0.77	13	6	7	3	4

[1] Semi-major axis.

[2] Radius of Hill sphere.

[3] Total number of known satellites.

[4] Number of regular satellites.

[5] Number of irregular satellites.

[6] Number of prograde irregular satellites.

[7] Number of retrograde irregular satellites.

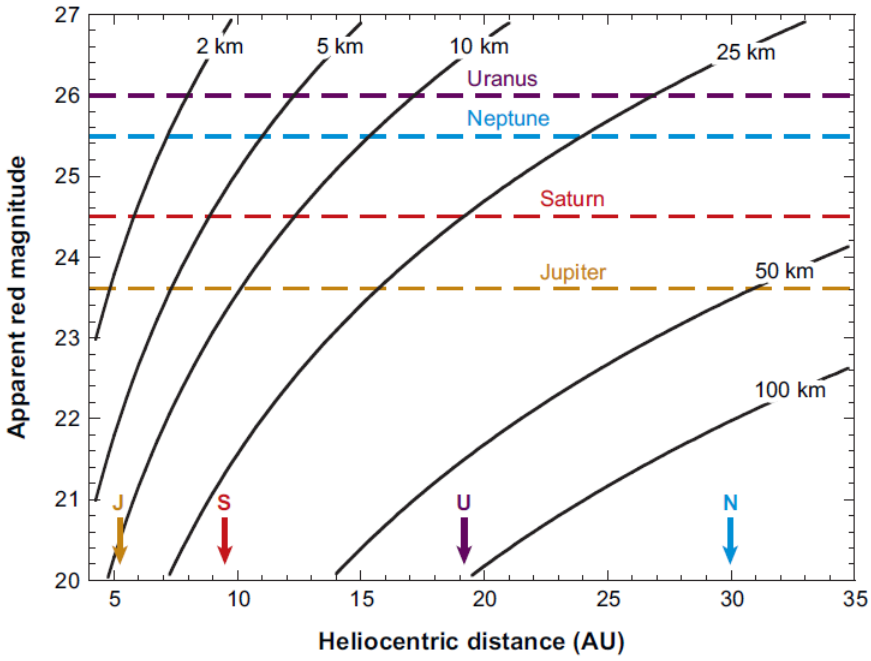

Figure 2.1: The relationship between diameter and apparent R-band magnitude for distant bodies as function of heliocentric distance. Values of diameter were derive with assuming a geometric albedo of 0.04, the typical value among comet nuclei. The semi-major axes of the giant planets are pointed by arrows with an initial letter. Dashed lines correspond to the observational magnitude limits of previous satellite surveys. This figure is originated from Jewitt & Haghighipour (2007).

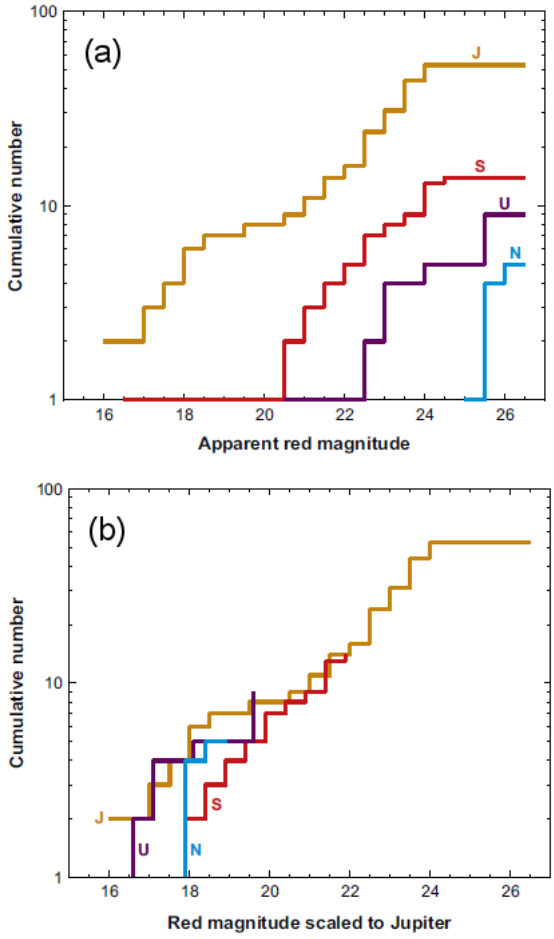

Figure 2.2: (a) Cumulative size distribution of the apparent R-band magnitude for the irregular satellites. (b) Cumulative size distribution of the apparent R-band magnitude for the irregular satellites corrected to Jupiter's opposition distance by the inverse square law. These figures are originated from Jewitt & Haghighipour (2007).

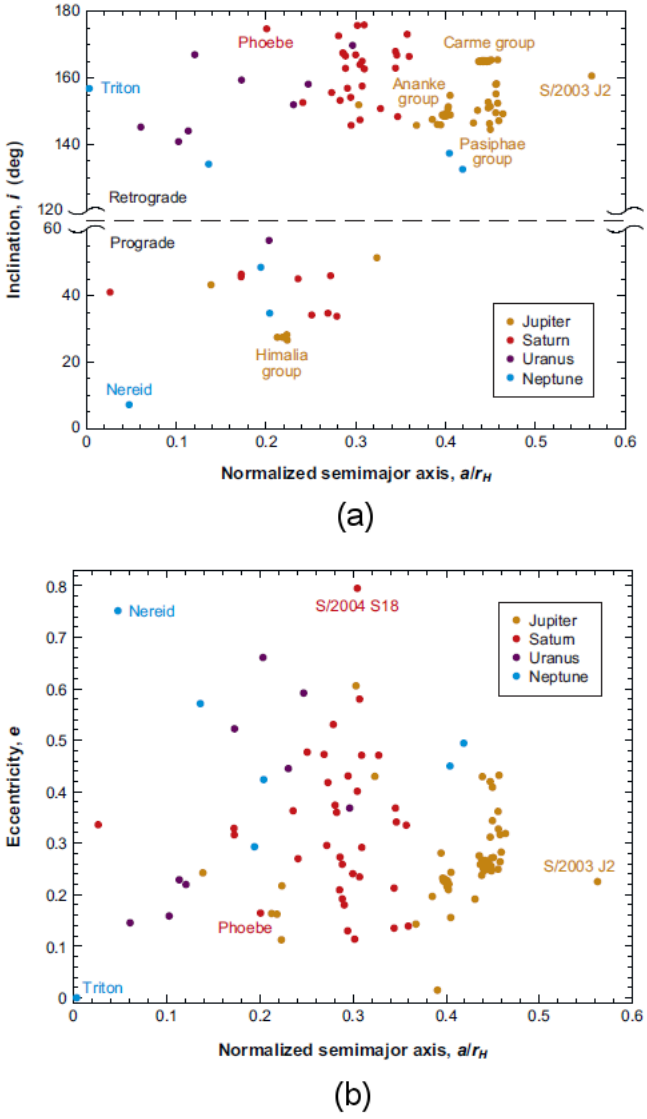

Figure 2.3: (a) Semi-major axis scaled to the Hill radius vs. inclination for the irregular satellites. The Jovian satellites have several cluster (family) labeled in the figure with the name of the largest members. (b) Semi-major axis scaled to the Hill radius vs. eccentricity for the irregular satellites. These figures are originated from Jewitt & Haghighipour (2007).

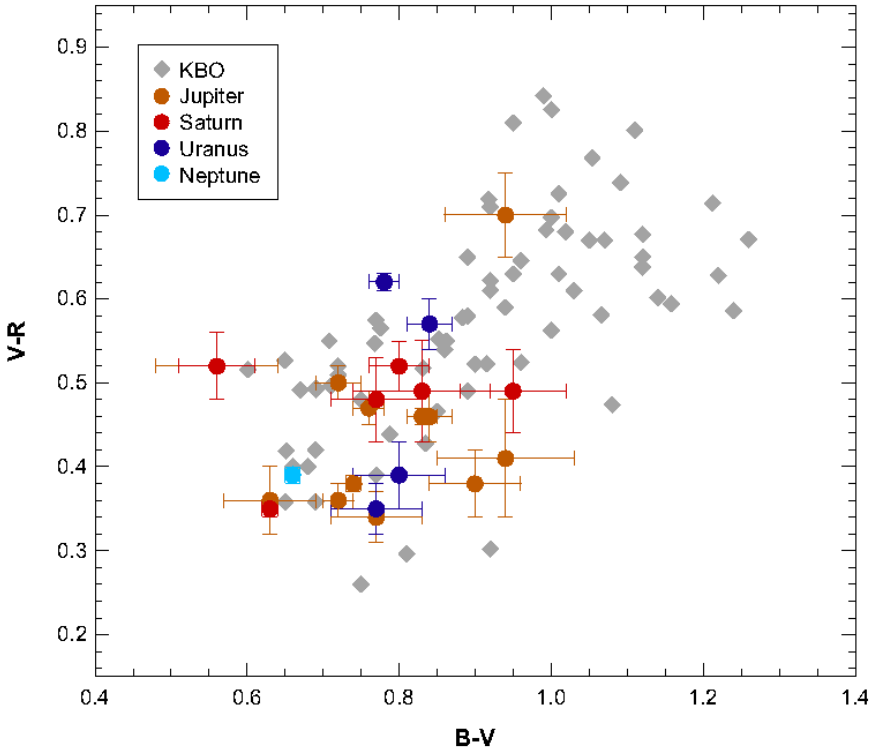

Figure 2.4: Color-cola diagram of $B-V$ and $V-R$ for the irregular satellites with TNOs. This figure is originated from Jewitt & Haghighipour (2007).

Table 2.2: Orbital and physical parameters for irregular satellites of Uranus. The orbital data were derived from JPL/NASA at http://ssd.jpl.nasa.gov/?sat_elem. The photometric data were derived from Sheppard et al. (2005). The diameters were estimated with an assumed albedo of 0.04.

Name		a[1] (km)	i[2] (deg)	e[3]	Period[4] (days)	R mag[5]	D[6] (km)	Year[7]
XXII	Francisco	4276000	145.2	0.146	266.6	25.0	22	2001
XVI	Caliban	7231000	140.9	0.159	579.7	22.4	72	1997
XX	Stephano	8004000	144.1	0.229	677.4	24.1	32	1999
XXI	Trinculo	8504000	167.1	0.220	759.0	25.4	18	2001
XVII	Sycorax	12179000	159.4	0.522	1288.3	20.8	150	1997
XXIII	Margaret	14345000	56.6	0.661	1694.8	25.2	20	2003
XVIII	Prospero	16256000	152.0	0.445	1977.3	23.2	50	1999
XIX	Setebos	17418000	158.2	0.591	2234.8	23.3	47	1999
XXIV	Ferdinand	20901000	169.8	0.368	2823.4	25.1	21	2003

[1] The mean semi-major axis.

[2] The mean inclination.

[3] The mean eccentricity.

[4] The time of one revolution around Uranus.

[5] The R-band magnitude of the object.

[6] The diameter of the object.

[7] The year of discovery.

Table 2.3: The results of previous photometric observations for irregular satellites of Uranus.

	M2001[1]		M2007[2]		G2004[3]		S2007[4]
Satellite	R (mag)	$V-R$ (mag)	V (mag)	$V-R$ (mag)	V (mag)	$V-R$ (mag)	R_c (mag)
Caliban	21.91±0.01	0.47±0.05			22.58±0.02	0.57±0.03	22.4
Sycorax	20.46±0.01	0.48±0.04	20.81±0.01	0.53±0.01	20.94±0.01	0.62±0.01	20.8
Prospero			23.79±0.04	0.59±0.07	23.91±0.03	0.39±0.04	23.2
Setebos			23.71±0.04	0.52±0.04	23.88±0.03	0.35±0.03	23.3
Stephano			24.94±0.16	0.73±0.17	25.12±0.17	0.67±0.22	24.1
Trinculo			25.67±0.41	0.82±0.43	25.25±0.18	0.35±0.19	25.4

[1] Maris et al. (2001)

[2] Maris et al. (2007)

[3] Grav et al. (2004)

[4] Sheppard et al. (2007)

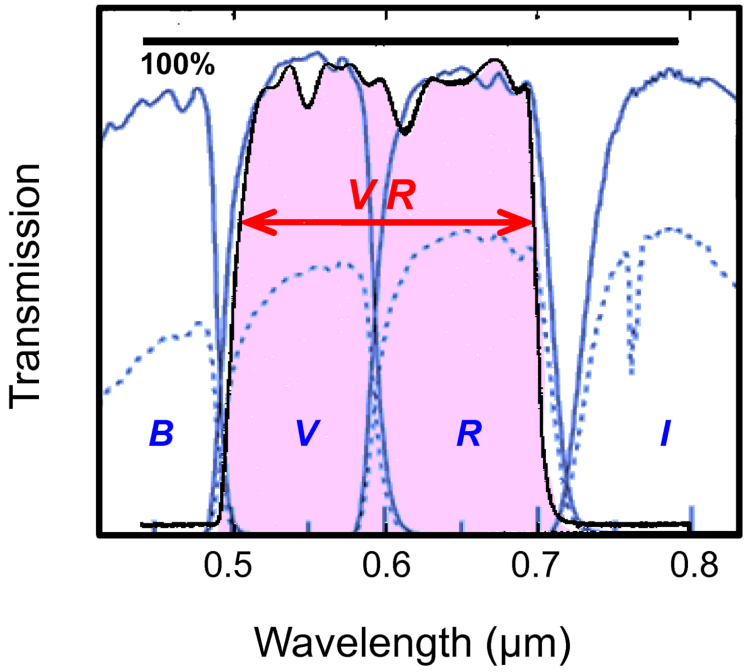

Figure 2.5: Transmission curves of VR filter (black line; Jewitt et al. 1996) The blue lines indicate the transmission curves of Suprime-Cam standard filters (Miyazaki et al., 2002).

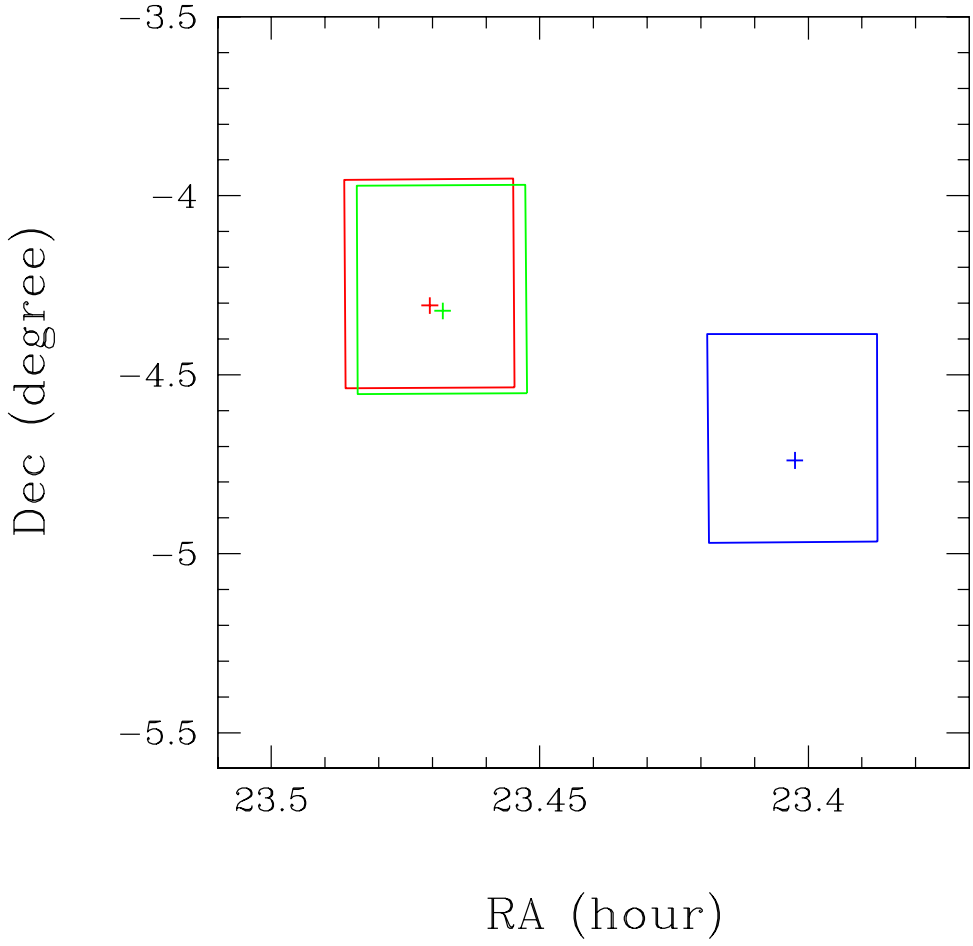

Figure 2.6: The observation fields at Sep 1 (red line), Sep 2 (green line), and Sep 29 (blue line). The cross marks shows the position of Uranus at each night.

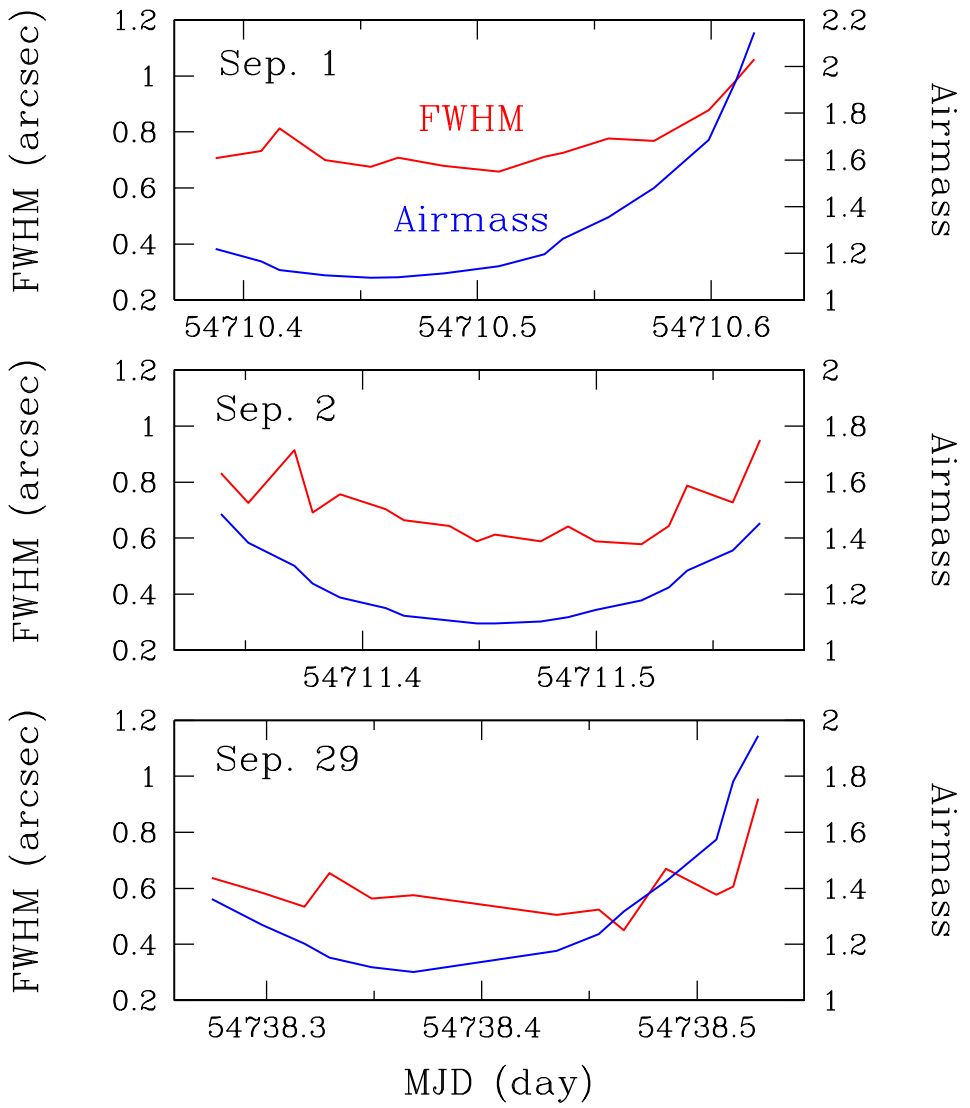

Figure 2.7: The red curves show the change of the full width at half maximum (FWHM) for point sources with time. The blue curves show the change of airmass with time at the observational field. The abscissa of each panel was expressed by modified Julian date (MJD=JD–2400000.5).

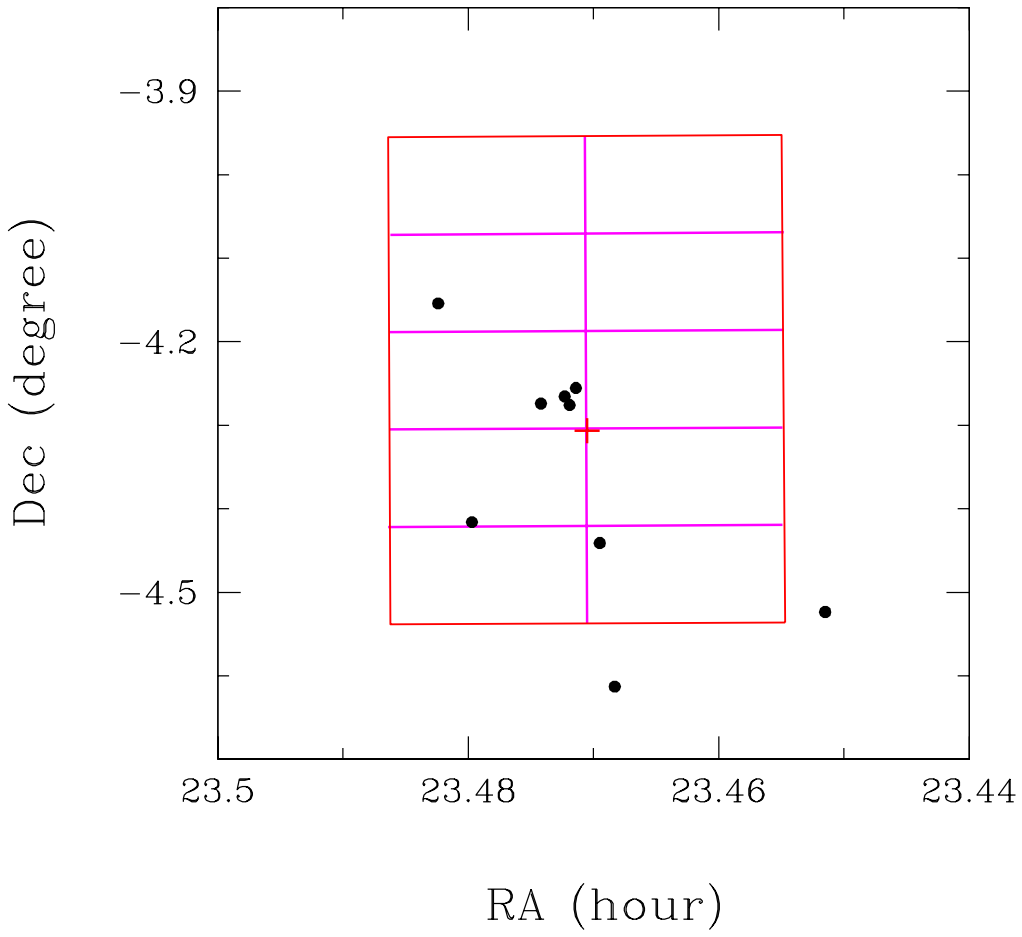

Figure 2.8: The positions of the known irregular satellites of Uranus (black dots) in the field of view (red line) in Sep 1. The pink lines show the gaps between CCD chips of the Suprime-Cam. The cross mark shows the position of Uranus.

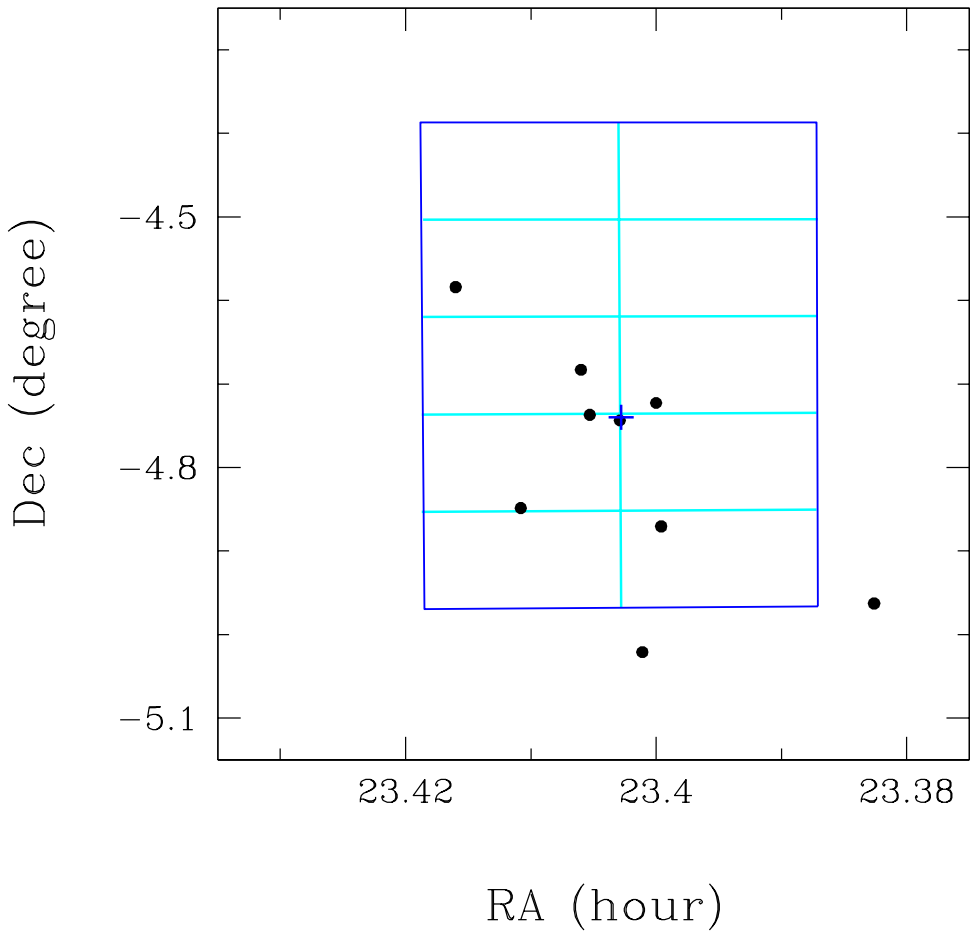

Figure 2.9: The same figure as Figure 2.8 but in Sep 29.

Table 2.4: Standard stars used for photometric calibrations (Landolt 1992).

Star	RA (J2000.0)	Dec (J2000.0)	V (mag)	$V-R$ (mag)
Region 1				
PG2213-006C	22:16:17.67	−00:22:14.2	15.109 ± 0.005	0.426 ± 0.002
PG2213-006B	22:16:21.68	−00:21:48.3	12.706 ± 0.001	0.427 ± 0.001
PG2213-006A	22:16:23.14	−00:21:26.8	14.178 ± 0.005	0.406 ± 0.003
PG2213-006	22:16:28.38	−00:21:13.1	14.124 ± 0.002	−0.092 ± 0.004
Region 2				
PG1633+099	16:35:24.09	+09:47:50.4	14.397 ± 0.003	−0.093 ± 0.003
PG1633+099A	16:35:25.98	+09:47:53.7	15.256 ± 0.004	0.505 ± 0.004
PG1633+099B	16:35:33.28	+09:46:21.3	12.969 ± 0.002	0.590 ± 0.001
PG1633+099C	16:35:37.30	+09:46:15.6	13.229 ± 0.003	0.618 ± 0.002
PG1633+099D	16:35:40.10	+09:46:41.8	13.691 ± 0.002	0.324 ± 0.002
Region 3				
MARK A2	20:43:54.99	−10:45:31.1	14.540 ± 0.003	0.379 ± 0.002
MARK A1	20:43:58.49	−10:47:11.7	15.911 ± 0.004	0.367 ± 0.004
MARK A	20:43:59.16	−10:47:41.7	13.258 ± 0.002	−0.115 ± 0.002
MARK A3	20:44:03.79	−10:45:36.5	14.818 ± 0.002	0.587 ± 0.002
Region 4				
RU 152F	07:29:53.74	−02:04:51.7	14.564 ± 0.005	0.382 ± 0.007
RU 152E	07:29:54.24	−02:05:30.6	12.362 ± 0.001	0.030 ± 0.001
RU 152	07:29:58.45	−02:06:37.2	13.014 ± 0.002	−0.057 ± 0.002
RU 152B	07:29:59.23	−02:05:57.1	15.019 ± 0.005	0.290 ± 0.005
RU 152A	07:30:00.49	−02:06:22.5	14.341 ± 0.006	0.325 ± 0.005
RU 152C	07:30:02.51	−02:05:37.6	12.222 ± 0.003	0.342 ± 0.002

Table 2.5: The observation parameters for the standard stars.

Region	RA (J2000.0)	Dec (J2000.0)	Exp (sec)	Airmass
Sep. 1				
Region 1	22:16:44.65	−00:22:18.0	2	2.782
Region 2	16:35:53.04	+09:47:48.0	2	1.071
Region 3	20:44:25.13	−10:47:10.9	2	1.596
Sep. 2				
Region 1	22:16:44.65	−00:21:28.0	2	2.634
Region 2	16:35:53.05	+09:48:38.0	2	1.061
Region 3	20:44:25.13	−10:46:21.0	2	1.648
Sep. 29				
Region 2	16:35:53.04	+09:48:38.1	2	1.297
Region 3	20:44:25.13	−10:46:20.9	2	1.243
Region 4	07:30:23.17	−02:04:58.0	2	1.277

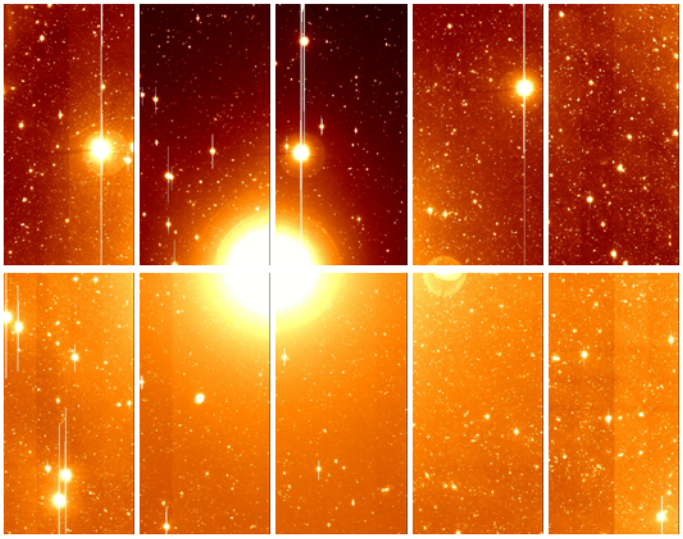

(a)

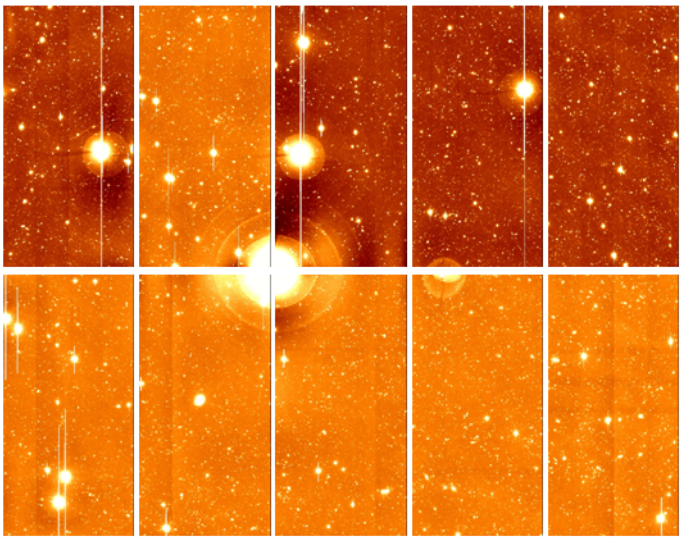

(b)

Figure 2.10: (a) A reduced image after bias subtracting and flat-fielding. (b) The same image as (a) but after background correction.

Table 2.6: Positions, distances from Uranus, and apparent motions of the observed satellites.

Satellite	RA (J2000.0)	Dec (J2000.0)	ΔRA (″)	ΔDec (″)	d(RA)/dt (″/hr)	d(Dec)/dt (″/hr)
Sep. 1						
Caliban	23:28:18.90	−04:16:32.7	77.8	110.5	−5.55	−2.50
Sycorax	23:28:56.59	−04:09:14.6	641.5	548.7	−5.33	−2.29
Prospero	23:28:47.08	−04:24:57.4	499.3	−394.1	−5.54	−2.32
Setebos	23:28:10.34	−04:26:27.7	−50.2	−484.4	−5.63	−2.31
Stephano	23:28:27.01	−04:16:26.4	199.2	116.8	−5.53	−2.48
Trinculo	23:28:20.43	−04:15:55.7	100.7	147.5	−5.33	−2.23
Francisco	23:28:16.99	−04:15:19.6	49.2	183.6	−5.75	−2.43
Sep. 2						
Caliban	23:28:10.14	−04:17:32.8	75.9	106.2	−5.58	−2.51
Sycorax	23:28:48.19	−04:10:09.7	644.8	549.4	−5.36	−2.30
Prospero	23:28:38.34	−04:25:53.2	497.6	−394.1	−5.57	−2.33
Setebos	23:28:01.46	−04:27:23.2	−53.9	−484.2	−5.65	−2.32
Stephano	23:28:18.29	−04:17:26.0	197.7	113.1	−5.56	−2.49
Sep. 29						
Sycorax	23:24:57.73	−04:35:02.4	727.7	560.4	−5.23	−2.19
Prospero	23:24:39.11	−04:50:54.9	449.6	−392.2	−5.42	−2.19
Setebos	23:23:58.66	−04:52:13.5	−155.1	−470.9	−5.49	−2.16
Trinculo	23:24:21.75	−04:40:58.7	189.9	203.9	−5.21	−2.12

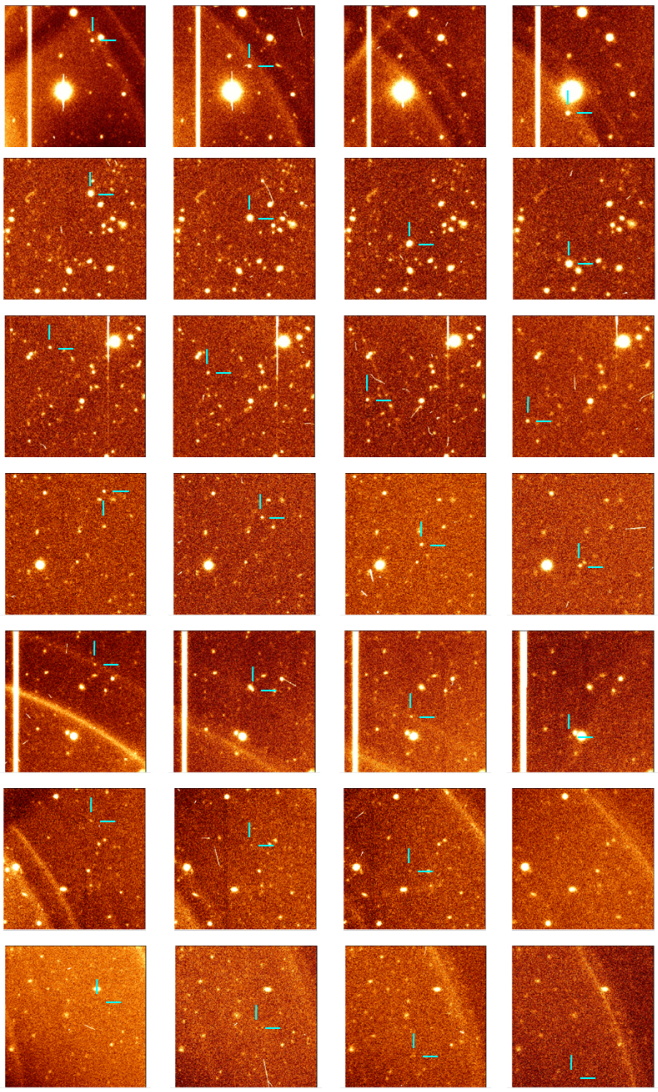

Figure 2.11: Motions of the detected irregular satellites from the data in Sep. 1, 2008. Each line includes XVI Caliban, XVII Sycorax, XVIII Prospero, XIX Setebos, XX Stephano, XXI Trinculo, and XXII Francisco in descending order. All frames have $1' \times 1'$ field of view. The intervals between two adjacent frames are $\sim$2 hours.

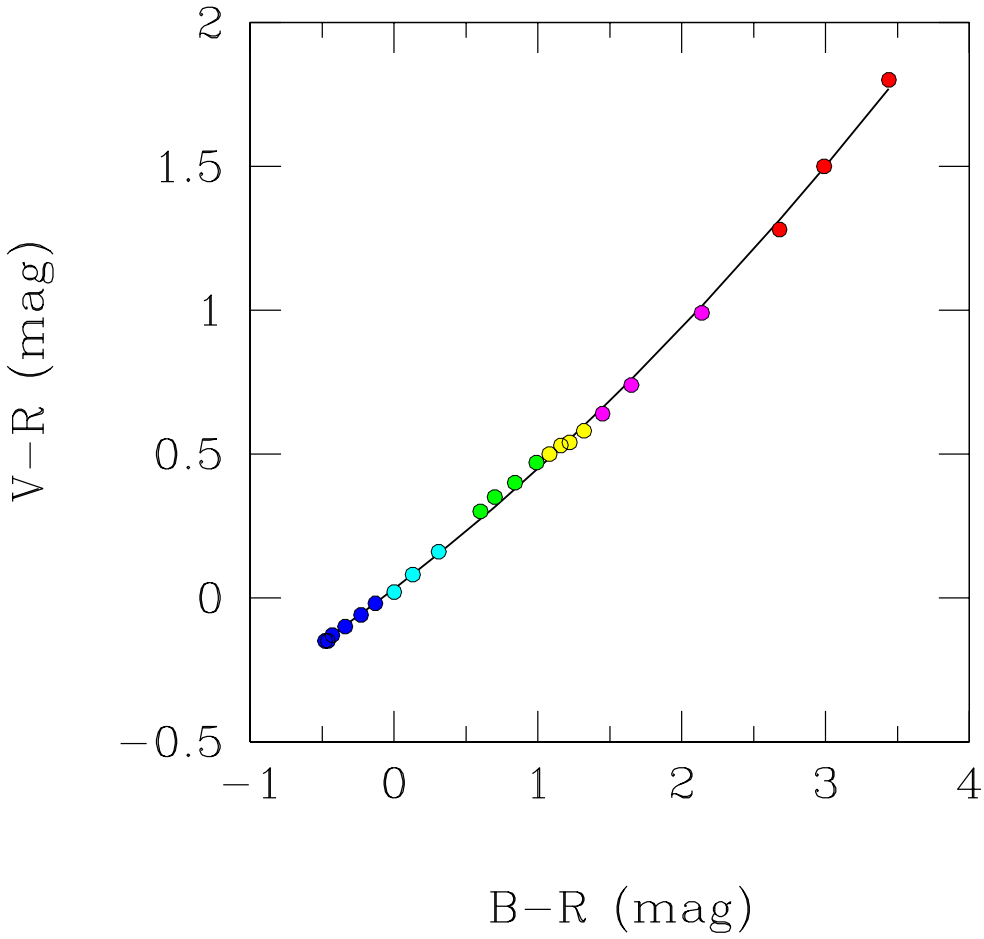

Figure 2.12: B–R vs V–R color for main sequence stars in Drilling & Landolt (2000). Each spectral class is shown by own-colored points (blue: O/B types, cyan: A type, green: K type, yellow: G type, pink: K type, red: M type). The solid curve indicates the approximated quadratic line with a least-square method.

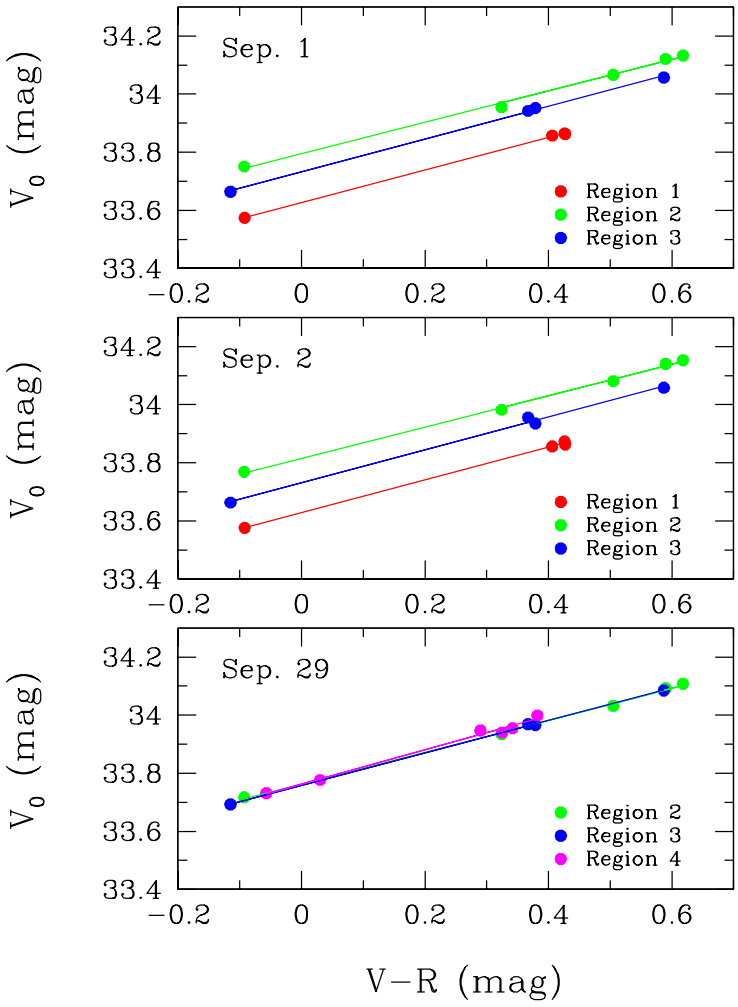

Figure 2.13: Correlations between the $V - R$ colors and the zero point V magnitudes of the Landolt standard stars. The objects in each region are listed in Table 2.4. The solid lines show the linear regression lines for each set of standard stars.

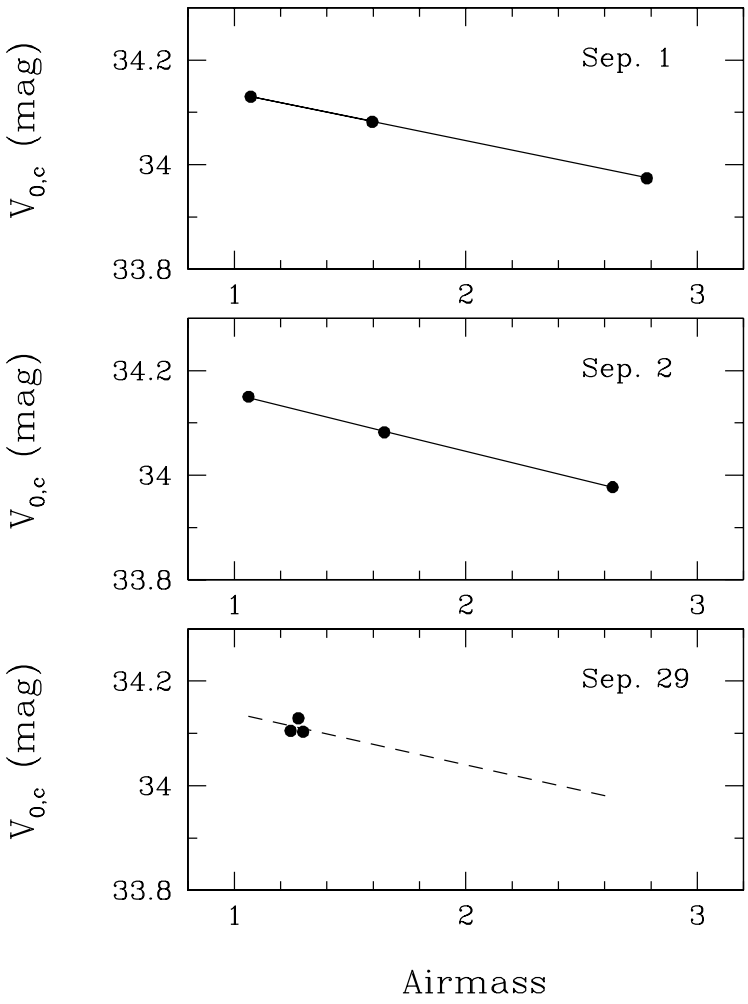

Figure 2.14: Correlations between the airmass and the color-corrected zero point V magnitudes of the standard stars for Sycorax. The solid lines are the linear regression lines. The dashed line in the bottom panel also shows the regression line, but it was obtained from the field stars, as shown in Figure 2.15.

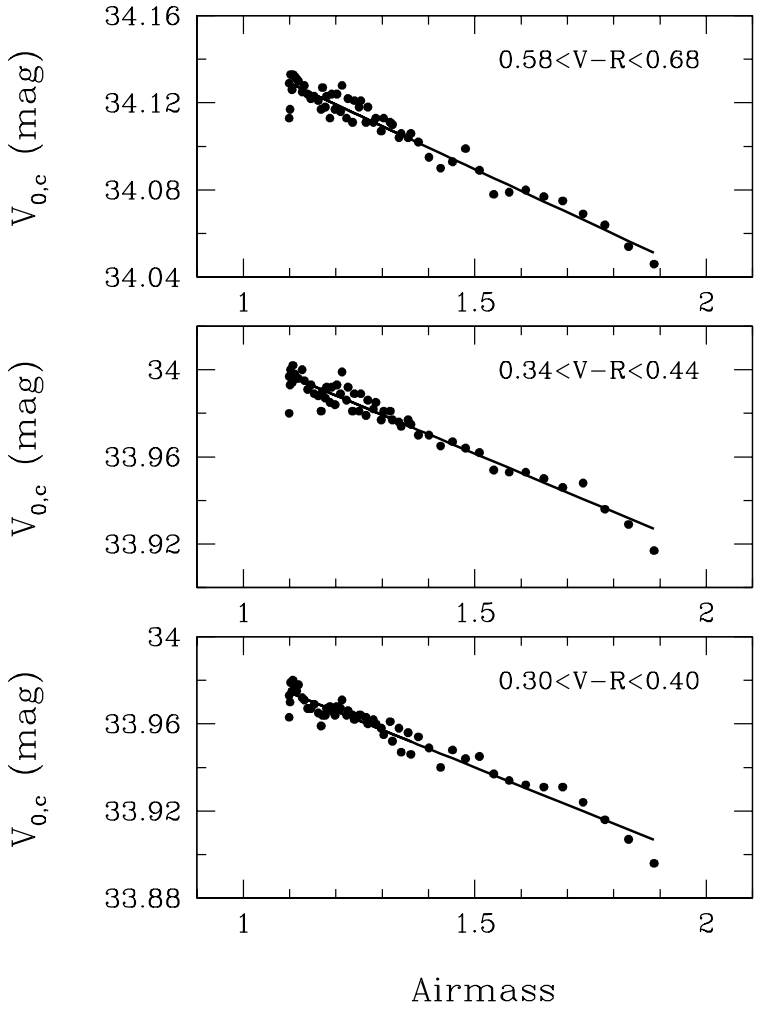

Figure 2.15: Correlations between the airmass and the color-corrected zero point V magnitudes of the field stars for the observation data obtained in Sep 29. The standard stars were selected with close $V-R$ colors for Sycorax (upper), Prospero (center), and Setebos (bottom). The solid lines are the linear regression lines.

Table 2.7: Color- and airmass-corrected zero point magnitudes $V_{0,c}(1)$ and atmospheric extinction slopes c.

	Sep. 1		Sep. 2		Sep. 29	
Satellite	$V_{0,c}(1)$ (mag)	c (mag)	$V_{0,c}(1)$ (mag)	c (mag)	$V_{0,c}(1)$ (mag)	c (mag)
Caliban	34.109±0.001	0.092±0.000	34.128±0.007	0.110±0.004	N/A	N/A
Sycorax	34.164±0.001	0.091±0.000	34.182±0.004	0.109±0.002	N/A	N/A
Prospero	34.137±0.000	0.091±0.000	34.155±0.005	0.109±0.002	34.139±0.004	0.099±0.003
Setebos	34.011±0.006	0.093±0.003	34.029±0.012	0.112±0.006	34.006±0.004	0.089±0.003
Stephano	33.989±0.005	0.094±0.003	34.008±0.011	0.113±0.006	33.983±0.004	0.086±0.003

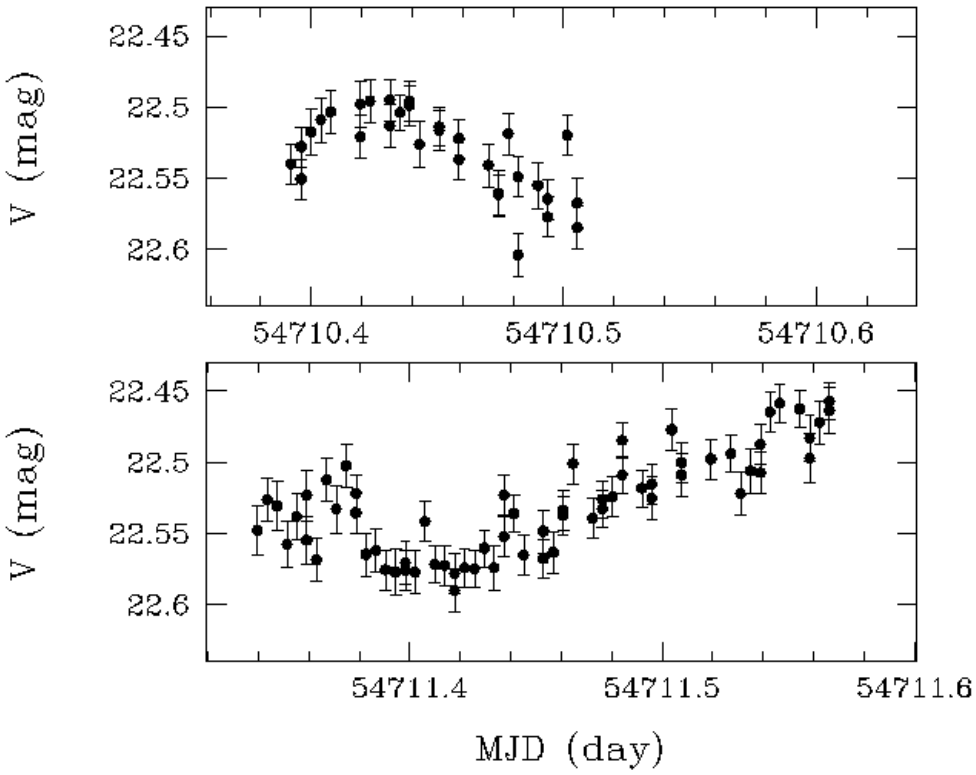

Figure 2.16: Light curves for Caliban. Data are for September 1 (upper) and 2 (bottom). The atmospheric extinction due to airmass was corrected. The blanks of data points indicate unmeasurable intervals due to overlapping with a star.

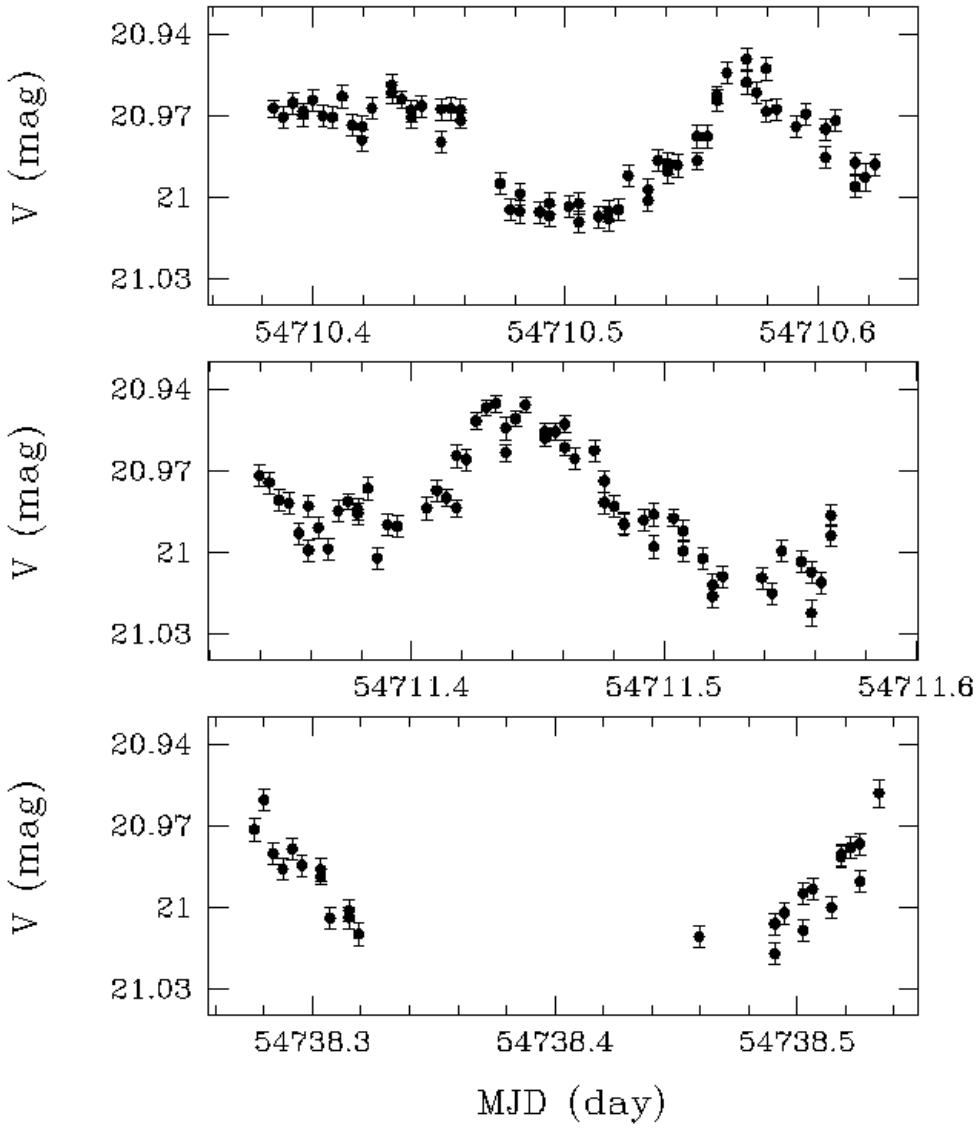

Figure 2.17: Light curves for Sycorax. Data are for September 1 (upper), 2 (middle), and 29 (bottom). see Figure 2.16 for comments.

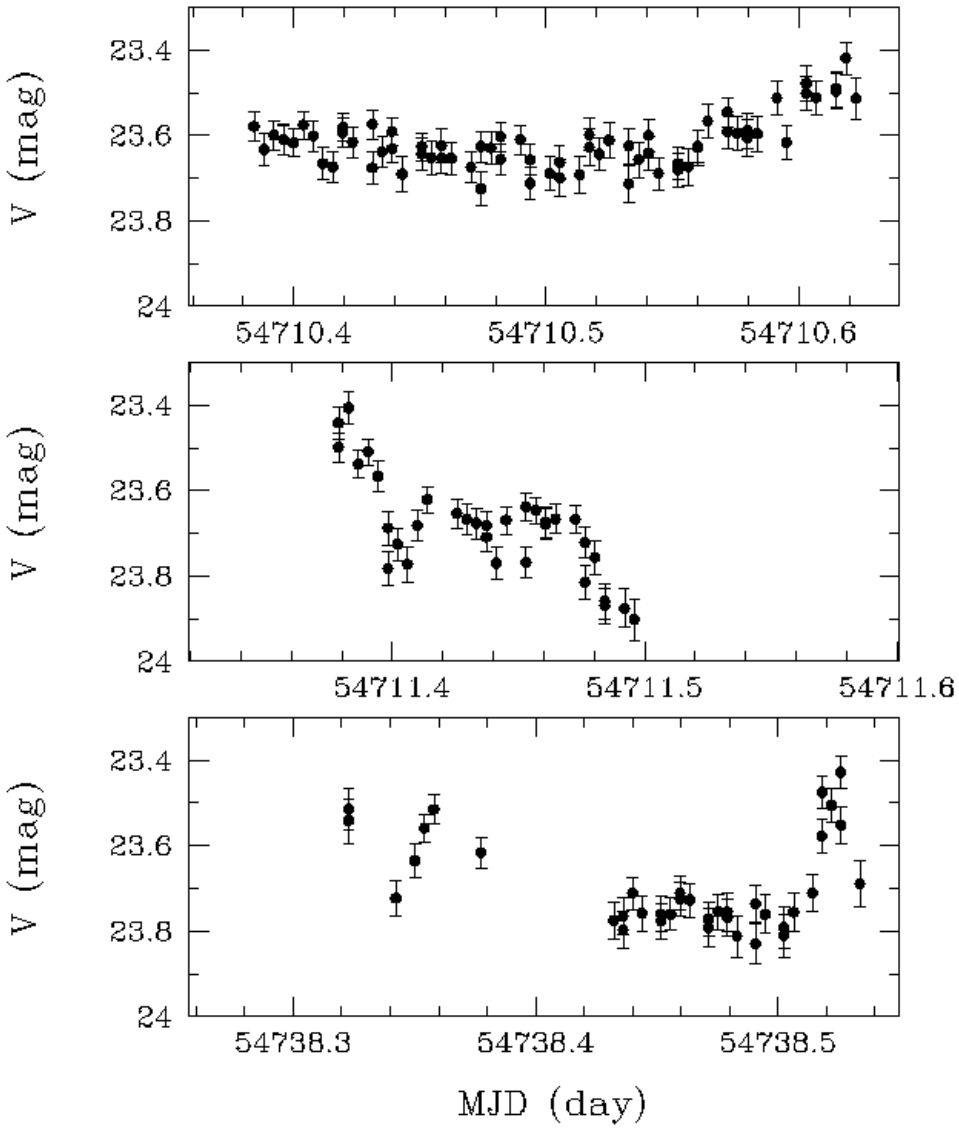

Figure 2.18: The same figure as Figure 2.17 but for Prospero.

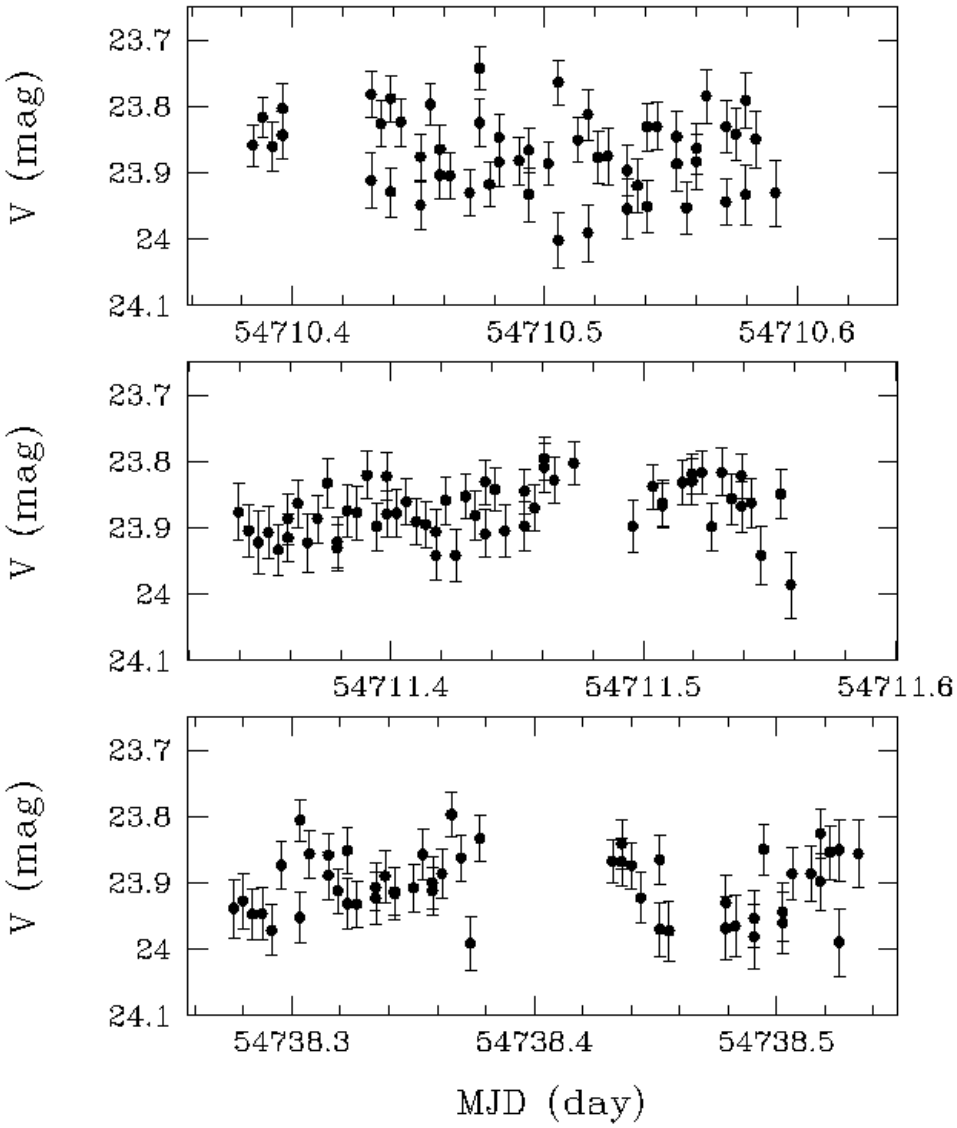

Figure 2.19: The same figure as Figure 2.17 but for Setebos.

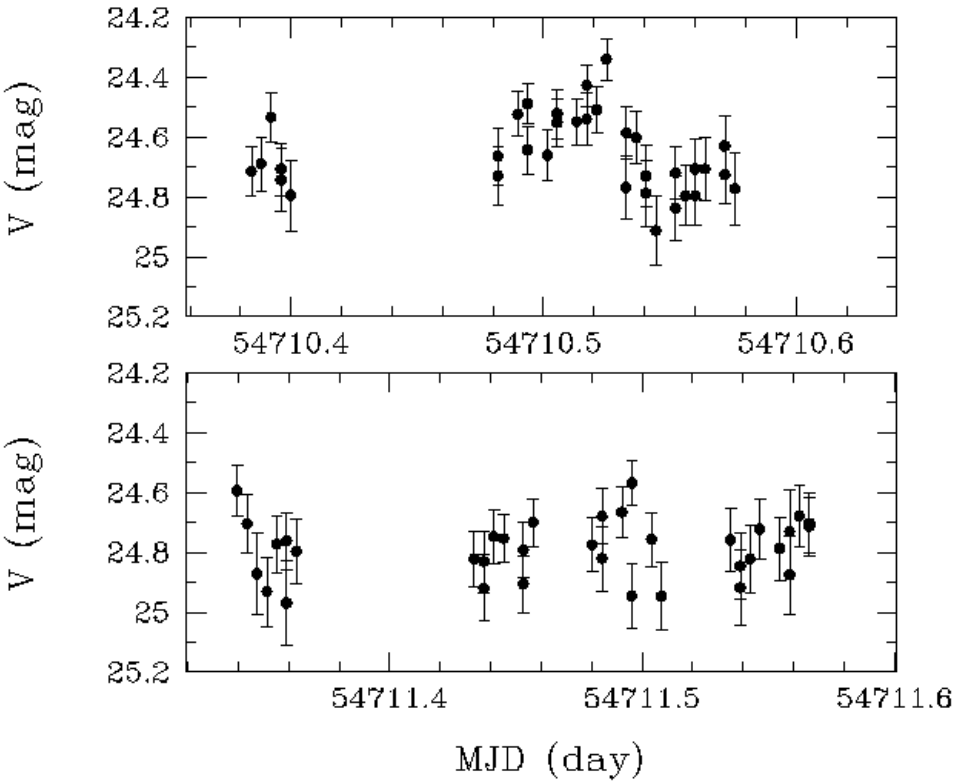

Figure 2.20: The same figure as Figure 2.16 but for Stephano.

Table 2.8: The results of the Wald-Wolfwitz runs test to check whether the magnitude variation is due to the random errors. z is the test statistic and z_0 is the significance level of 0.05 (z_0=1.96). If $|z| > z_0$, the null hypothesis is rejected.

Satellite	Date	z	Results
Caliban	Sep. 1	-2.66	$\|z\| > z_0$
	Sep. 2	-4.87	$\|z\| > z_0$
Sycorax	Sep. 1	-6.39	$\|z\| > z_0$
	Sep. 2	-5.50	$\|z\| > z_0$
	Sep. 29	-3.60	$\|z\| > z_0$
Prospero	Sep. 1	-3.49	$\|z\| > z_0$
	Sep. 2	-2.58	$\|z\| > z_0$
	Sep. 29	-4.67	$\|z\| > z_0$
Setebos	Sep. 1	0.70	$\|z\| < z_0$
	Sep. 2	-1.20	$\|z\| < z_0$
	Sep. 29	-1.52	$\|z\| < z_0$
Stephano	Sep. 1	-2.33	$\|z\| > z_0$
	Sep. 2	-0.47	$\|z\| < z_0$

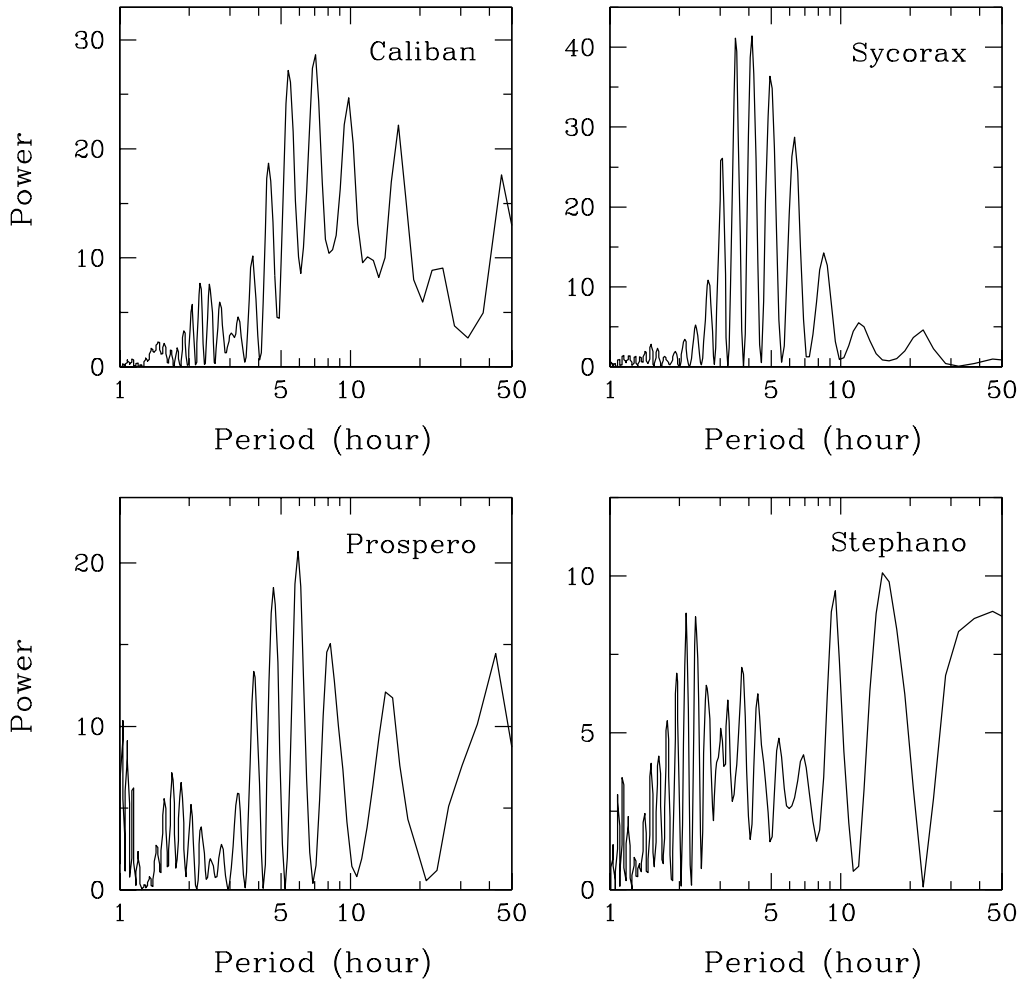

Figure 2.21: The periodogram for Caliban, Sycorax, Prospero, and Stephano using the first- and second-night photometric data.

Table 2.9: The results of periodic analysis. V_0 and A show the basement magnitude and amplitude, respectively. χ^2 was defined in Eq. 2.12.

Satellite	Period (hour)	V_0 (mag)	A (mag)	χ^2
Caliban	5.4 ± 0.3	22.531	0.037	2.22×10^2
	7.1 ± 0.5	22.525	0.039	1.97×10^2
Sycorax	3.5 ± 0.2	20.981	0.022	10.1×10^2
	4.1 ± 0.3	20.982	0.021	9.70×10^2
Prospero	4.6 ± 0.1	23.639	0.067	3.33×10^2
	5.9 ± 0.1	23.624	0.078	3.06×10^2
Stephano	2.14 ± 0.05	24.681	0.107	1.00×10^2
	2.34 ± 0.05	24.686	0.105	1.00×10^2
	9.5 ± 0.5	24.700	0.121	0.99×10^2
	15 ± 2	24.703	0.099	0.99×10^2

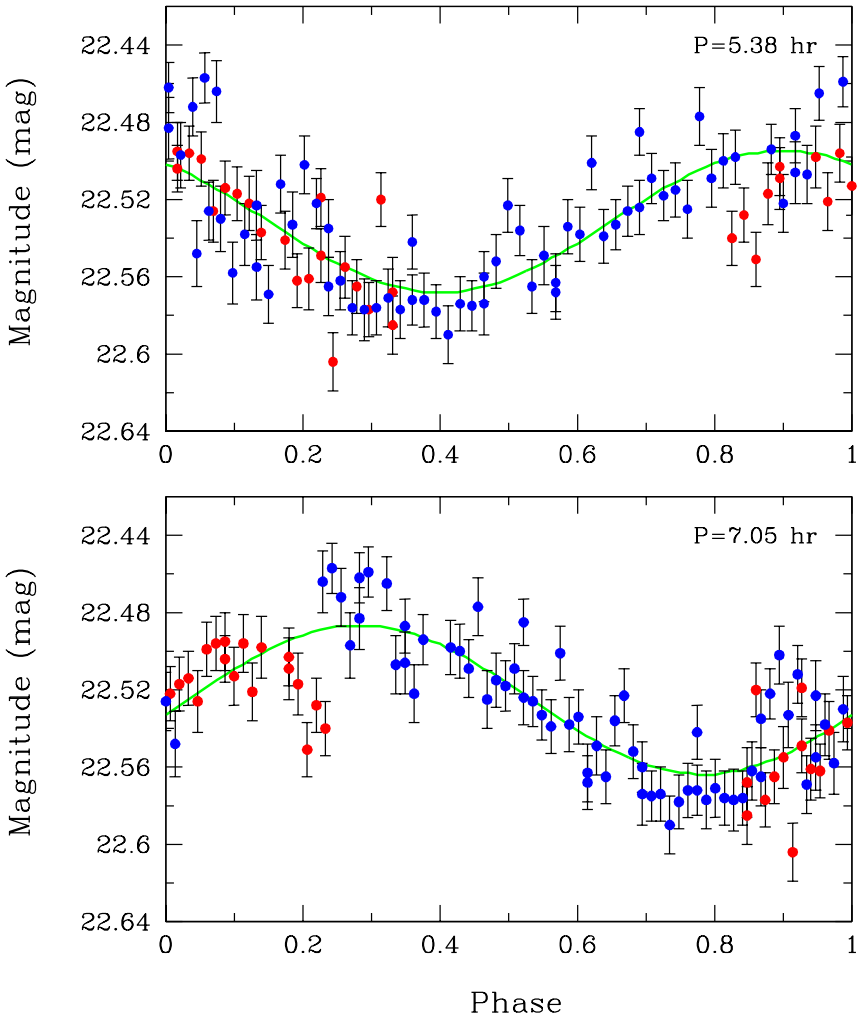

Figure 2.22: Lightcurves for Caliban.

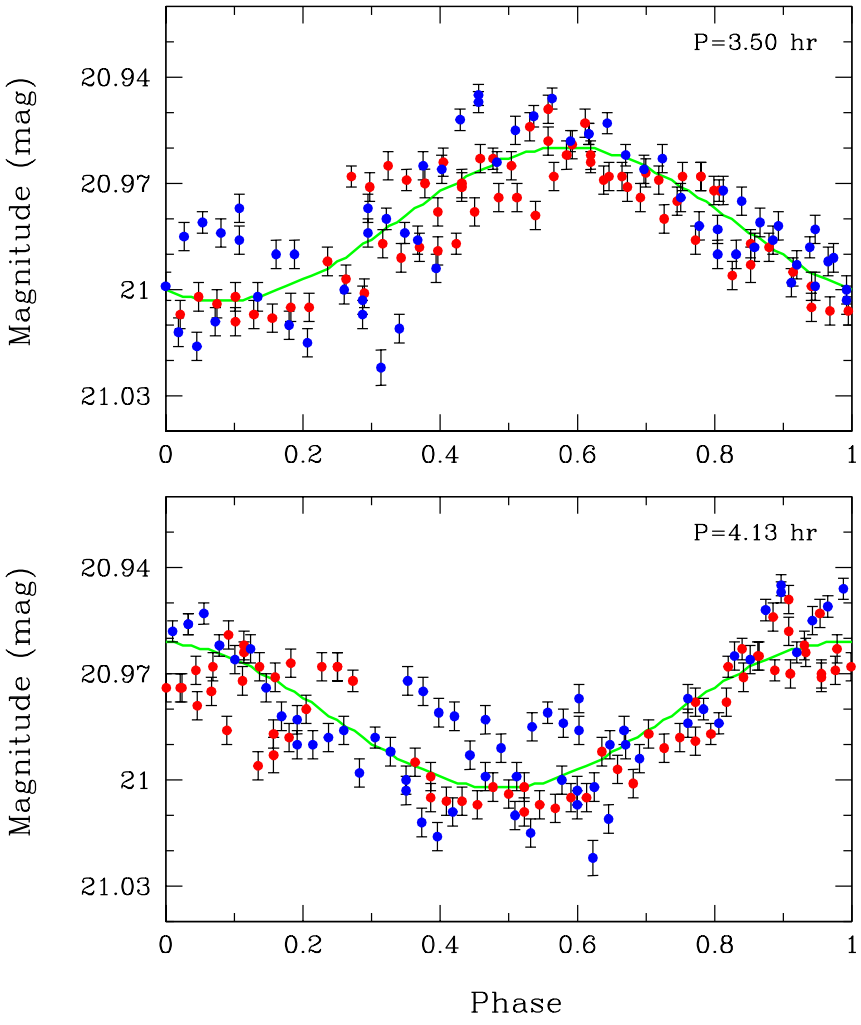

Figure 2.23: Lightcurves for Sycorax.

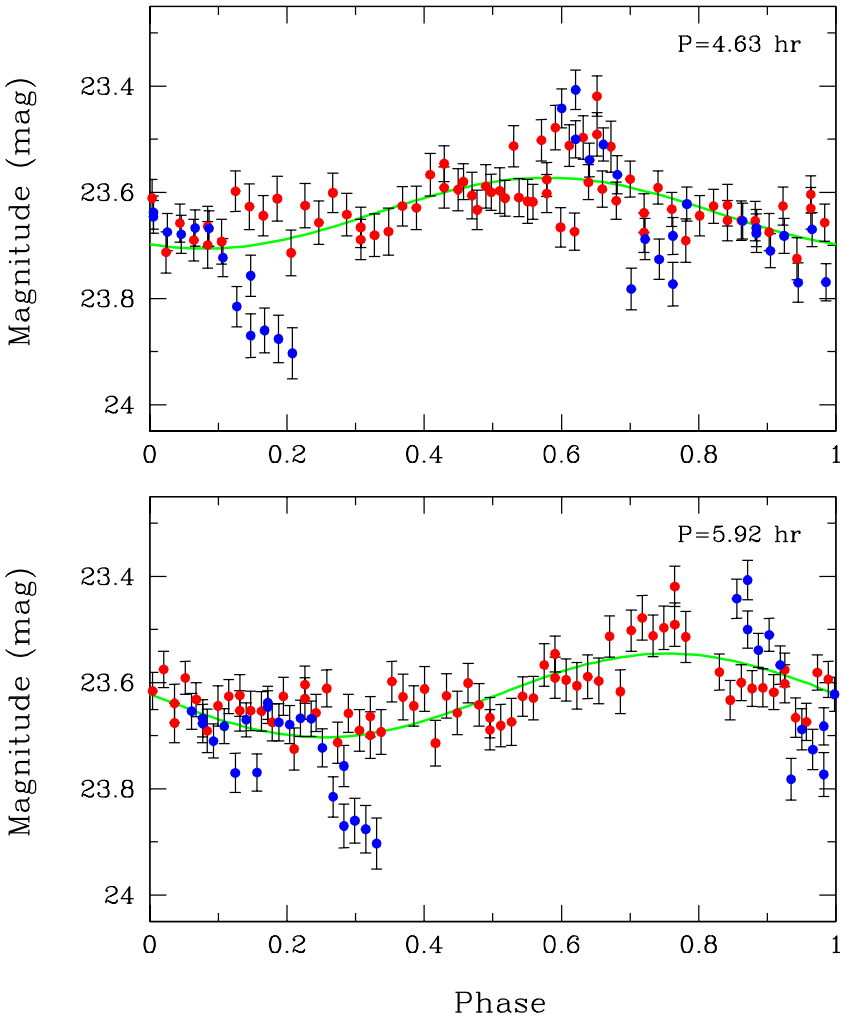

Figure 2.24: Lightcurves for Prospero.

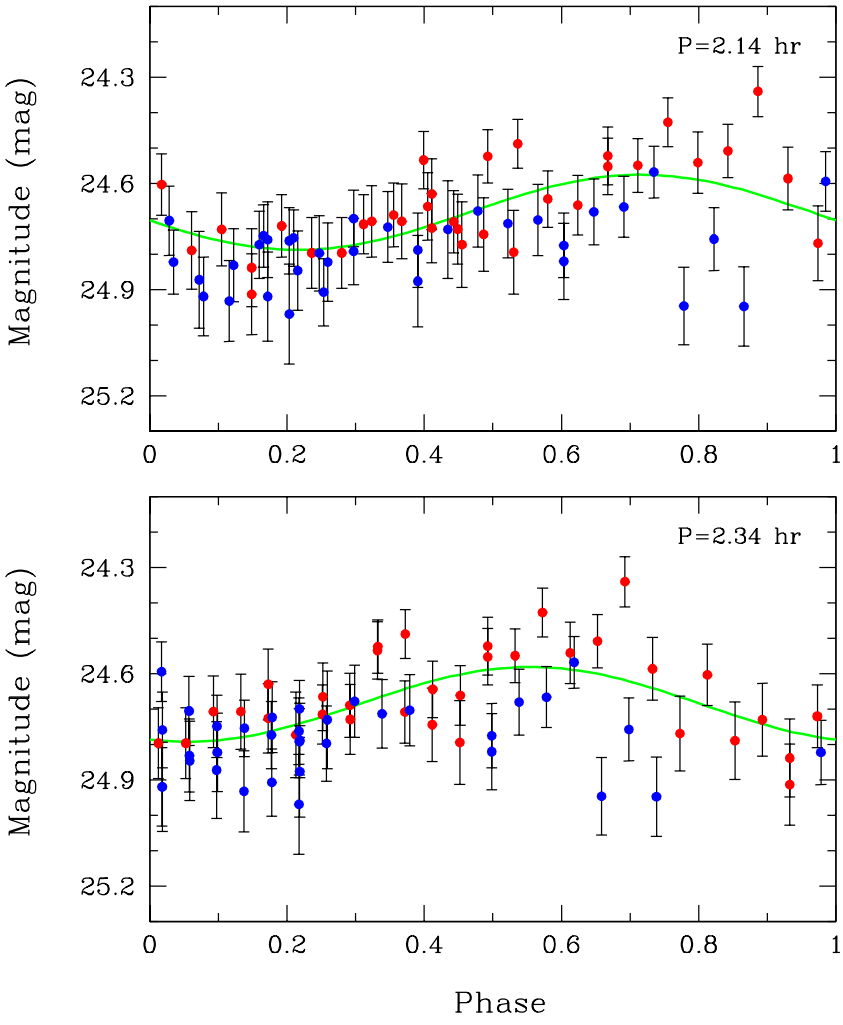

Figure 2.25: Lightcurves for Stephano.

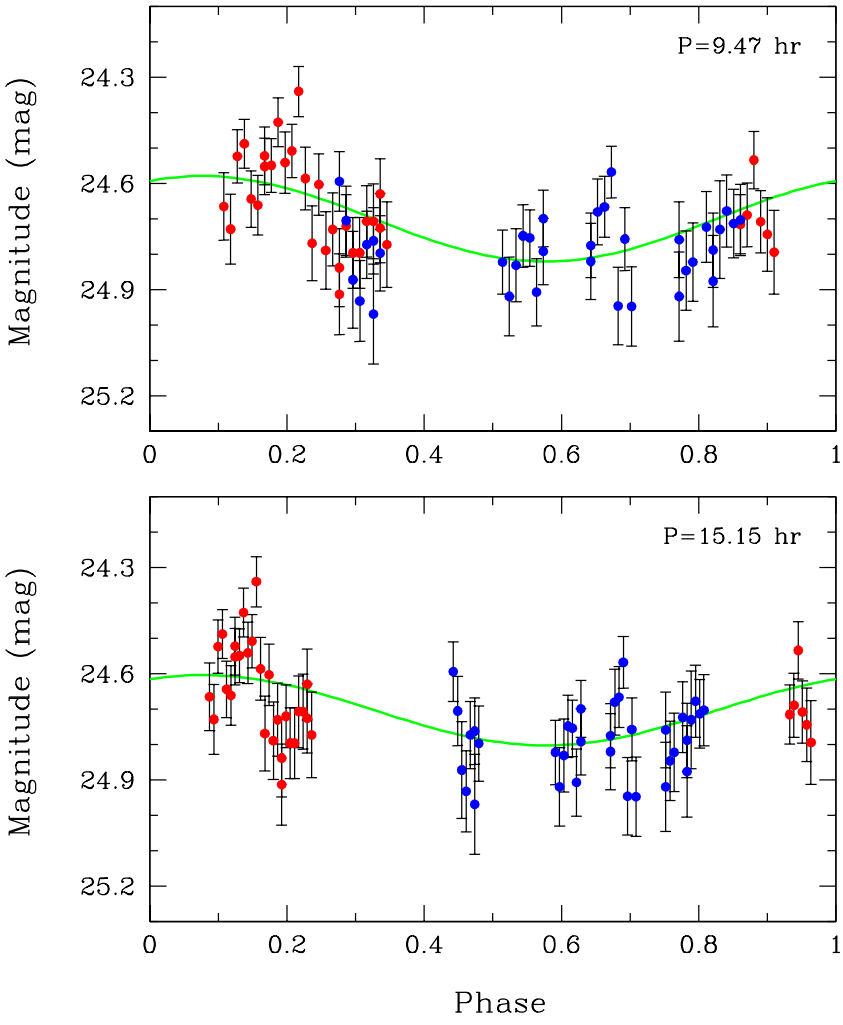

Figure 2.25: *Continued.*

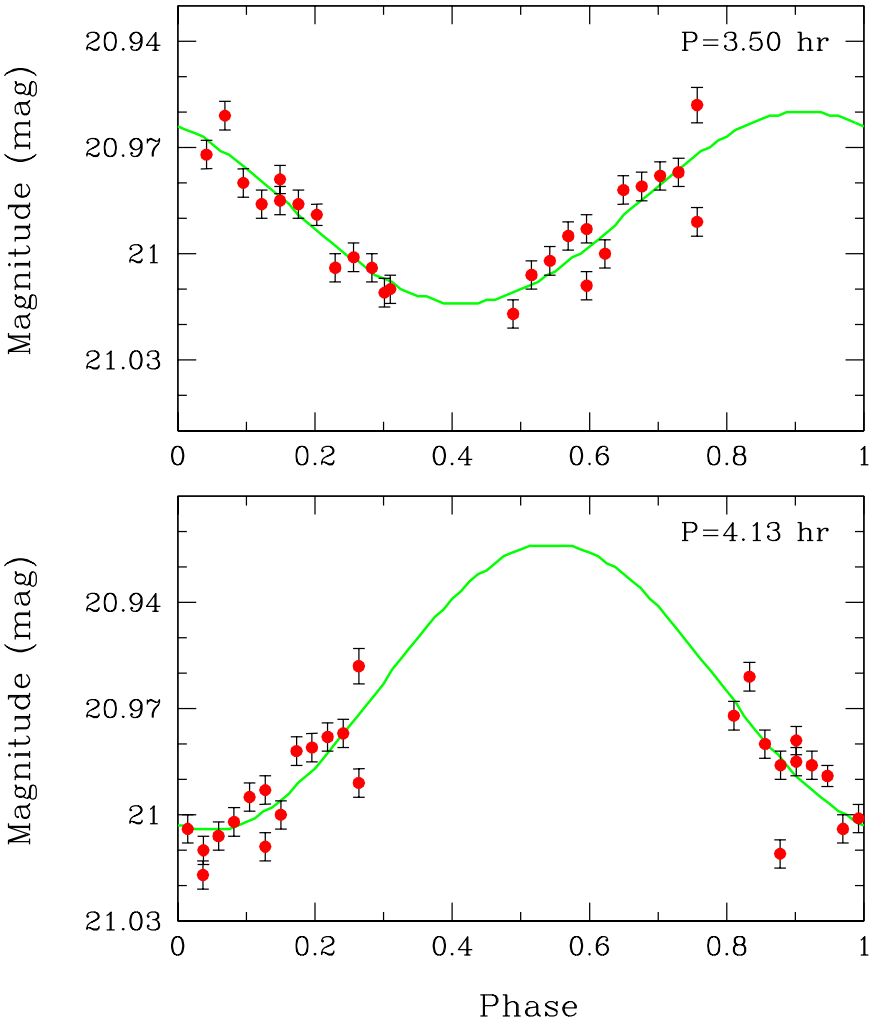

Figure 2.26: Brightness variations for Sycorax in the last-night data. The upper panel shows phase vs magnitude under 3.50-hr period. The bottom panel shows the same one under 4.13-hr period. The green lines are lightcurves derived from the first- and second-night data.

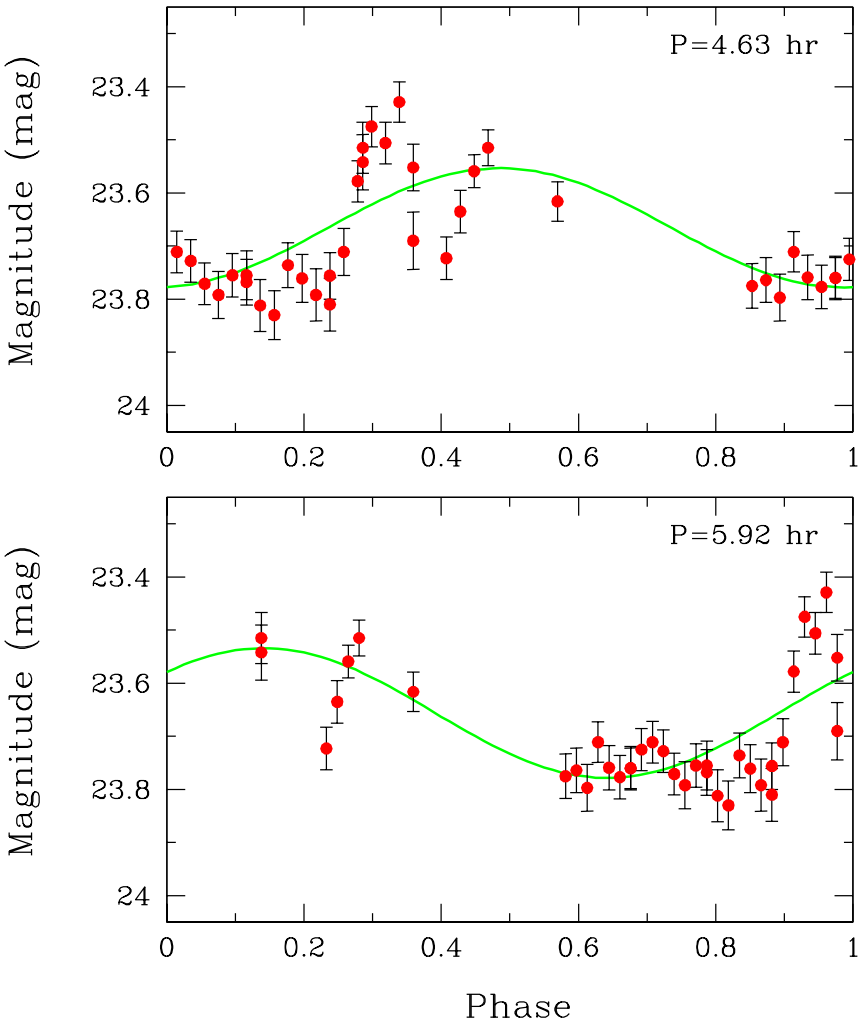

Figure 2.27: The same figure as Figure 2.26 but for Prospero. The upper and bottom panels show phase vs magnitude under 4.63-hr and 5.92-hr periods, respectively.

Table 2.10: The results of periodic analysis using the last-night data. V_0 and A show the basement magnitude and amplitude, respectively. χ^2 was defined in Eq. 2.12.

Satellite	Period (hour)	V_0 (mag)	A (mag)	χ^2
Sycorax	3.5	20.987	0.027	0.73×10^2
	4.1	20.984	0.040	1.42×10^2
Prospero	4.6	23.665	0.112	1.21×10^2
	5.9	23.666	0.122	1.22×10^2

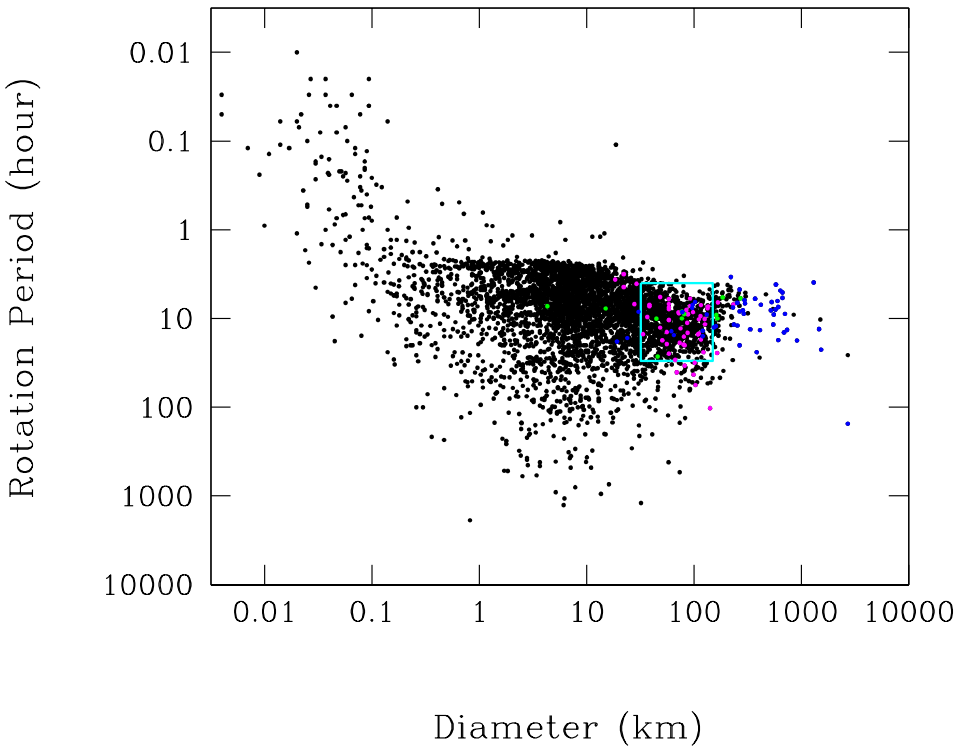

Figure 2.28: Diameter vs rotation periods of small Solar system bodies: asteroids (black), JTs (pink), Centaurs (green), and trans-Neptunian objects (blue). The period data were obtained from Collaborative Asteroid Lightcurve Link (http://www.minorplanetobserver.com/astlc/LightcurveParameters.htm). The region surrounded cyan lines shows the period distribution of the Uranian irregular satellites determined by this study. The diameters of the satellites were derived from Sheppard et al. (2005).

Table 2.11: The basement magnitude V_0 at the first/second and last nights, the difference in V_0 between the two epochs, and the one per 1° phase angle. V_0 for Sycorax and Prospero were derived from the fitted lightcurves. For Setebos, the mean magnitudes were used as V_0.

Satellite	V_0 (mag)		ΔV_0	S
	Sep. 1–2	Sep. 29	(mag)	(mag deg^{-1})
Sycorax	20.981±0.001	20.987±0.001	+0.006±0.001	0.03±0.01
Prospero	23.632±0.008	23.666±0.001	+0.034±0.008	0.14±0.03
Setebos	23.872±0.050	23.903±0.049	+0.031±0.070	0.13±0.55

Table 2.12: $B-V$ colors and sarge slopes S for Centaurs and trans-Neptunian objects (TNOs).

Object	$B-V$ (mag)	S (mag deg^{-1})	Reference
Centaurs			
Echeclus	0.85±0.08	0.18±0.02	Schaefer et al. (2009)
Asbolus	0.74±0.04	0.05±0.01	Schaefer et al. (2009)
Elatus	1.08±0.05	0.18±0.05	Schaefer et al. (2009)
Thereus	0.71±0.01	0.07±0.01	Schaefer et al. (2009)
1999 TD10	0.73±0.04	0.12±0.01	Schaefer et al. (2009)
Bienor	0.70±0.06	0.10±0.01	Schaefer et al. (2009)
2002 PN34	0.76±0.01	0.04±0.01	Schaefer et al. (2009)
Pelion	0.75±0.08	0.11±0.03	Schaefer et al. (2009)
Typhon	0.75±0.04	0.13±0.01	Schaefer et al. (2009)
2002 GZ32	0.67±0.04	0.01±0.03	Schaefer et al. (2009)
Hylonome	0.67±0.08	0.13±0.06	Schaefer et al. (2009)
TNOs			
2000 GN171	0.92±0.06	0.21±0.02	Schaefer et al. (2009)
Huya	0.96±0.05	0.13±0.01	Schaefer et al. (2009)
Ixion	1.03±0.03	0.15±0.03	Schaefer et al. (2009)
1999 TC36	1.03±0.04	0.21±0.03	Schaefer et al. (2009)
1999 DE9	0.97±0.05	0.16±0.02	Schaefer et al. (2009)
1999 KR16	1.12±0.07	0.12±0.03	Schaefer et al. (2009)
2005 RM43	0.59±0.04	0.18±0.03	Schaefer et al. (2009)
2002 UX25	0.98±0.05	0.14±0.02	Schaefer et al. (2009)
2002 KX14	1.05±0.03	0.18±0.03	Schaefer et al. (2009)
Varuna	0.89±0.05	0.25±0.02	Schaefer et al. (2009)
2002 AW197	0.90±0.03	0.10±0.03	Schaefer et al. (2009)
1996 GQ21	1.01±0.07	0.14±0.03	Sheppard & Jewitt (2002)
2001 CZ31	0.60±0.15	0.13±0.04	Sheppard & Jewitt (2002)

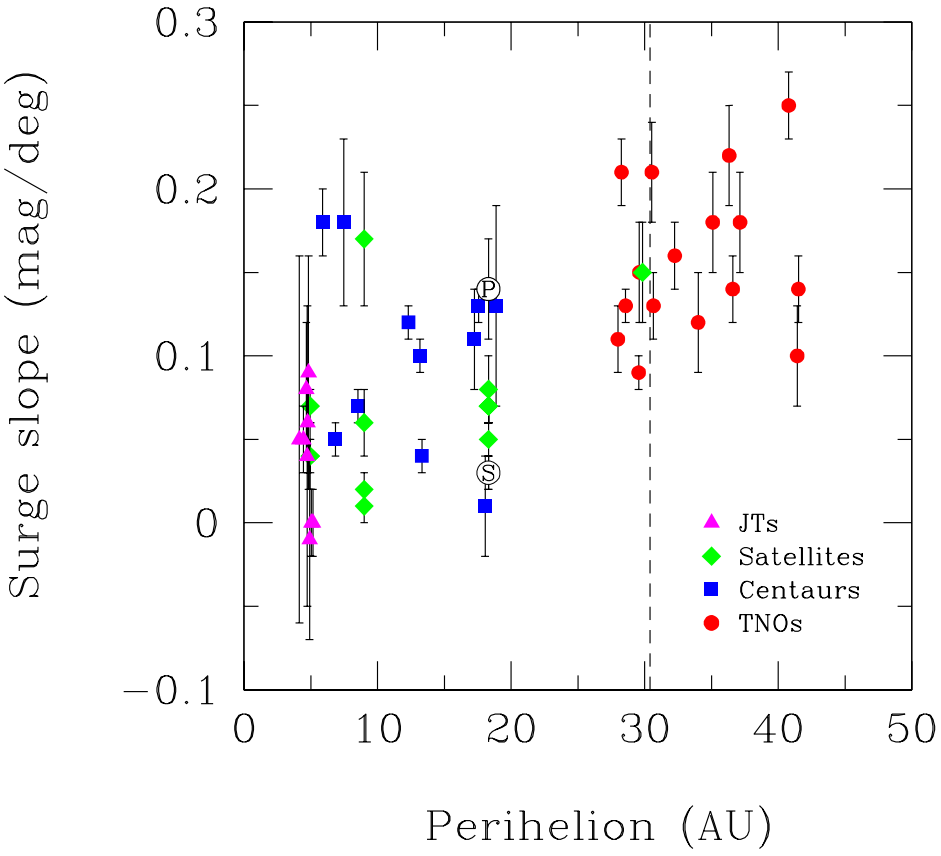

Figure 2.29: Surge slope vs. perihelion distribution. The symbols are circles for TNOs, squares for Centaurs, diamonds for planetary satellites, and triangles for Jovian Trojans. The dashed line represents the 40-AU semi-major axis with the mean eccentricity 0.24 of the sample objects. The open-circle symbols lettered with "S" and "P" show Sycorax and Prospero, respectively.

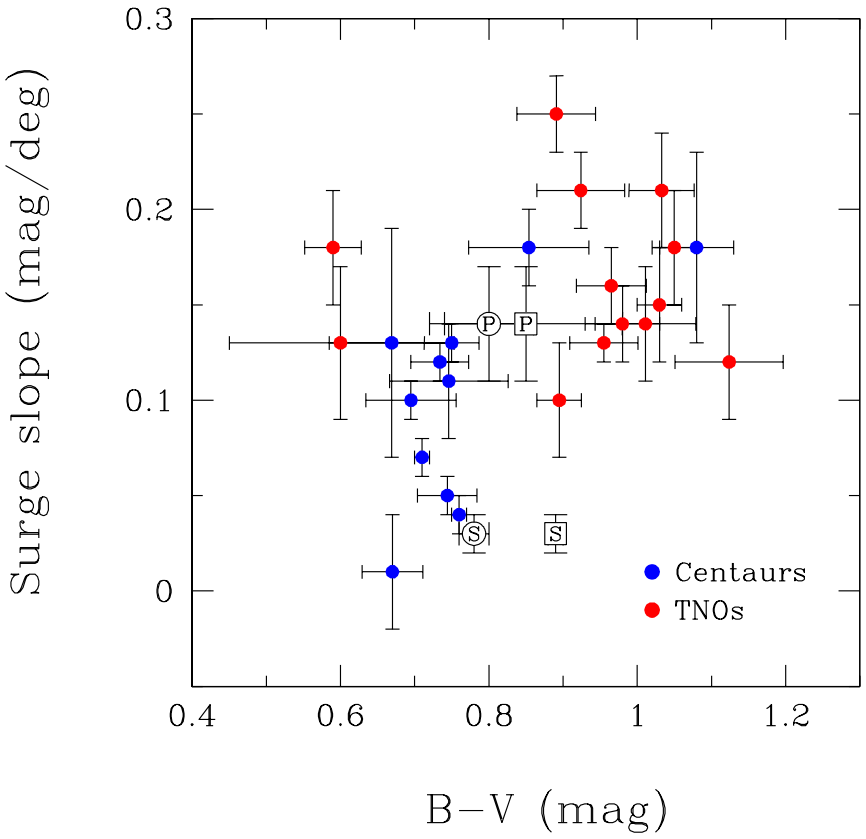

Figure 2.30: $B-V$ color vs surge slope at phase angles less than 1° for observed satellites with Centaurs and trans-Neptunian objects. The marks lettered with "S" and "P" indicate Sycorax and Prospero, respectively. The open squares with a letter show that the color data derived from (Maris et al., 2007). The open circles with a letter show that the color data derived from (Grav et al., 2004). The blue points are Centaurs, and the red points are trans-Neptunian objects. The $B-V$ color of the Sun is 0.65 (Livingston, 2000).

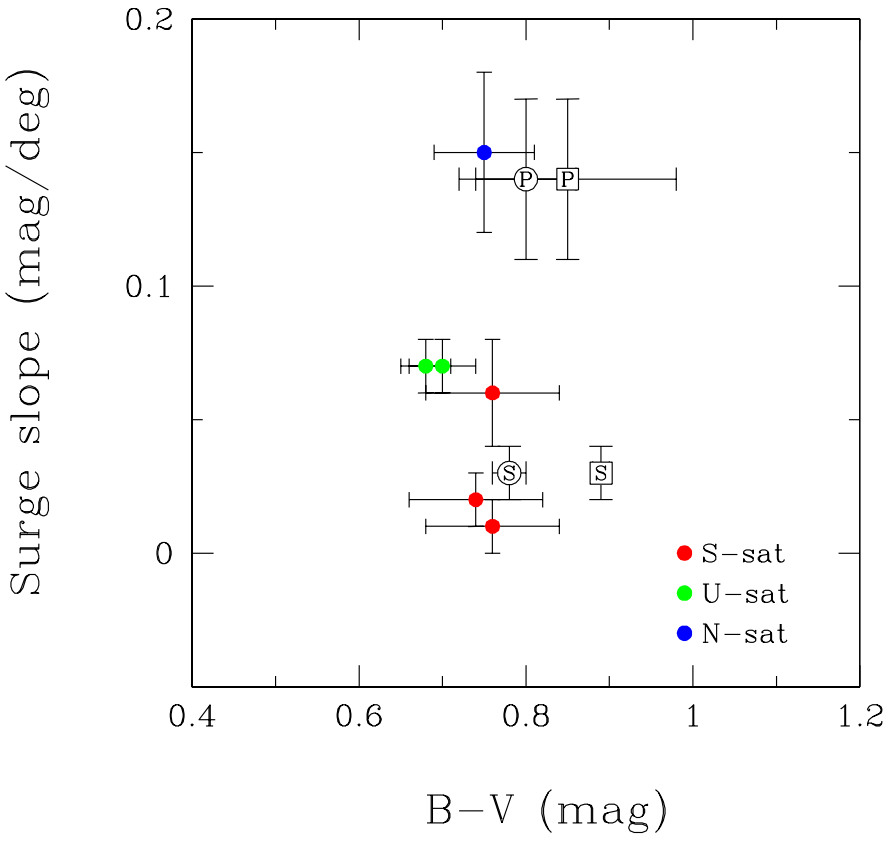

Figure 2.31: Surge slope vs. $B-V$ color at phase angles less than 1° for observed satellites with 7 satellites of Saturn and Uranus, and Neptune. The representations of the symbols for observed satellites are same as Figure 2.30. The red and green points show regular satellites of Saturn (Tethys, Dione, and Rhea) and Uranus (Titania and Oberon), respectively. The blue points represent a irregular satellites of Neptune, Nereid.

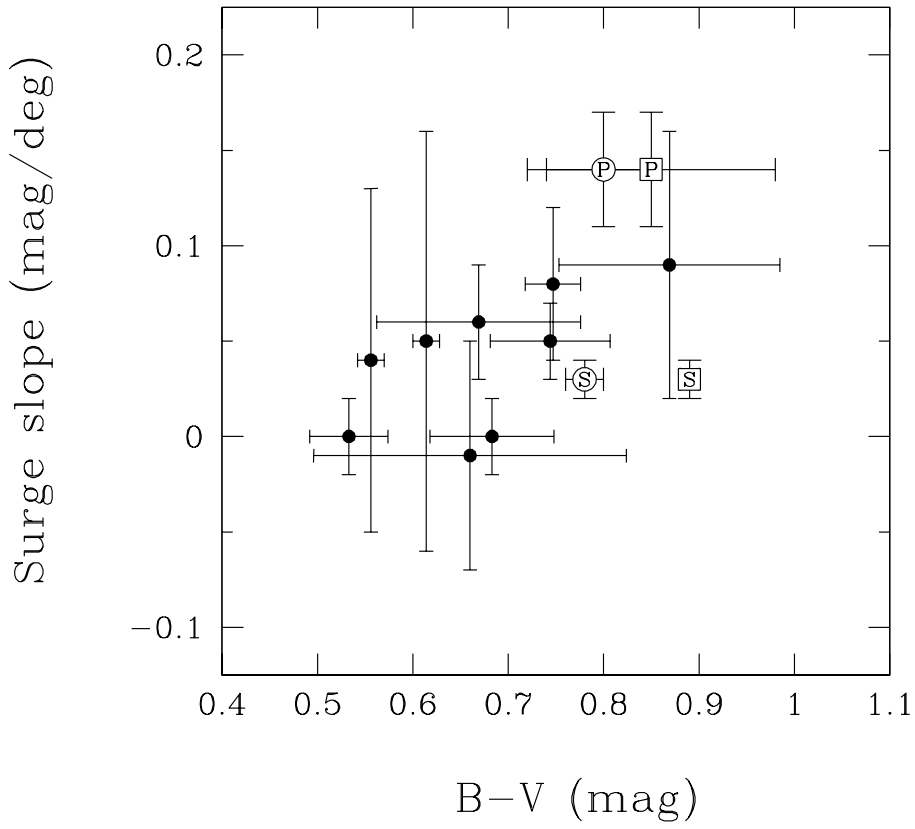

Figure 2.32: Surge slope vs. $B-V$ color at phase angles less than 1° for observed satellites with 9 Jovian Trojans. The representations of the symbols for observed satellites are same as Figure 2.30. The filled circles show the Trojan objects.

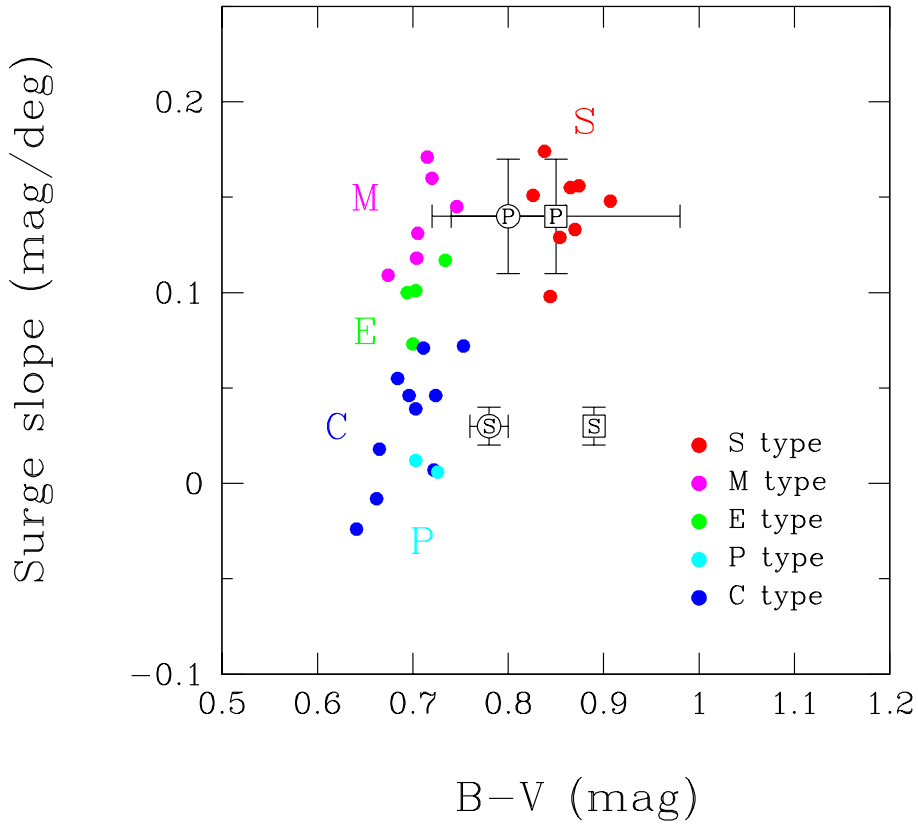

Figure 2.33: Surge slope vs. $B-V$ color at phase angles less than 1° for observed satellites with 31 asteroids. The representations of the symbols for observed satellites are same as Figure 2.30. The asteroids are classified as S- (red), M- (pink), E- (green), P- (cyan), and C-types (blue).

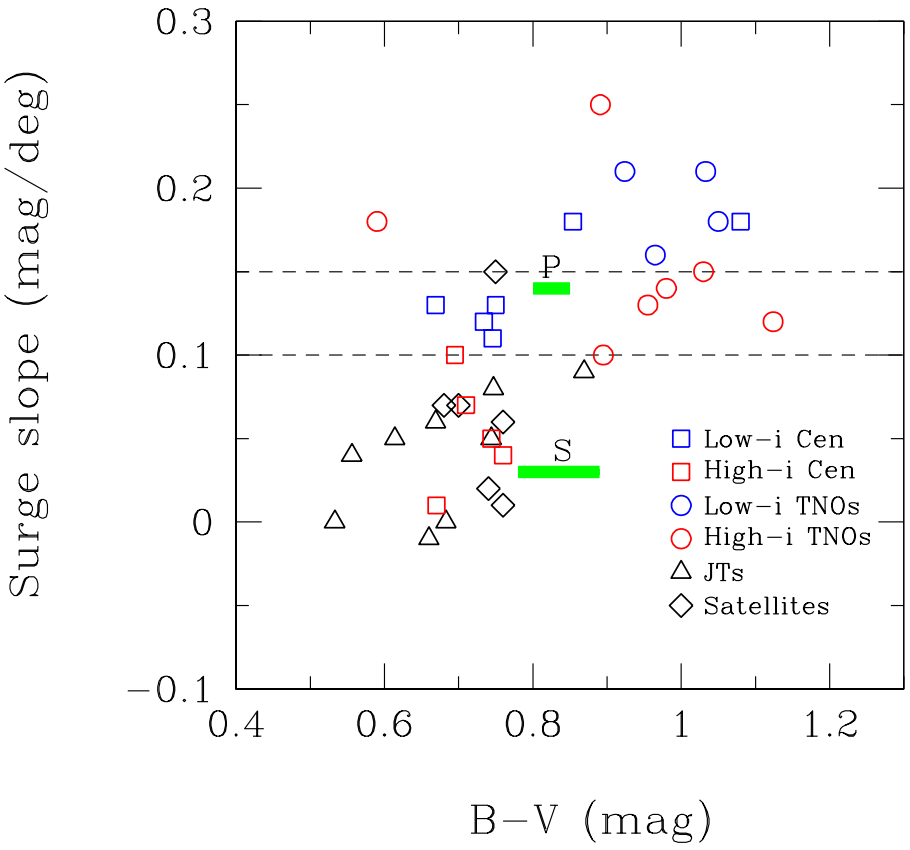

Figure 2.34: Surge slope vs. $B-V$ color distribution. The symbols are blue circles for TNOs with i<15°, red circles for TNOs with i>15°, blue squares for Centaurs with i<15°, red squares for Centaurs with i>15°, where i is inclination. The bars lettered by "S" and "P" show Sycorax and Prospero, respectively, whose length corresponds to the variation of the measurements by Grav et al. (2004); Maris et al. (2007). The open triangles and open diamonds represent Jovian Trojans and planetary satellites (regular satellites of Saturn and Uranus and a irregular satellite Nereid). Only Nereid has a surge slope larger than 0.1 in the satellite sample. The dashed lines indicate the boundaries among the categories with surge slopes, low-, mid-, and high-surge populations (see text).

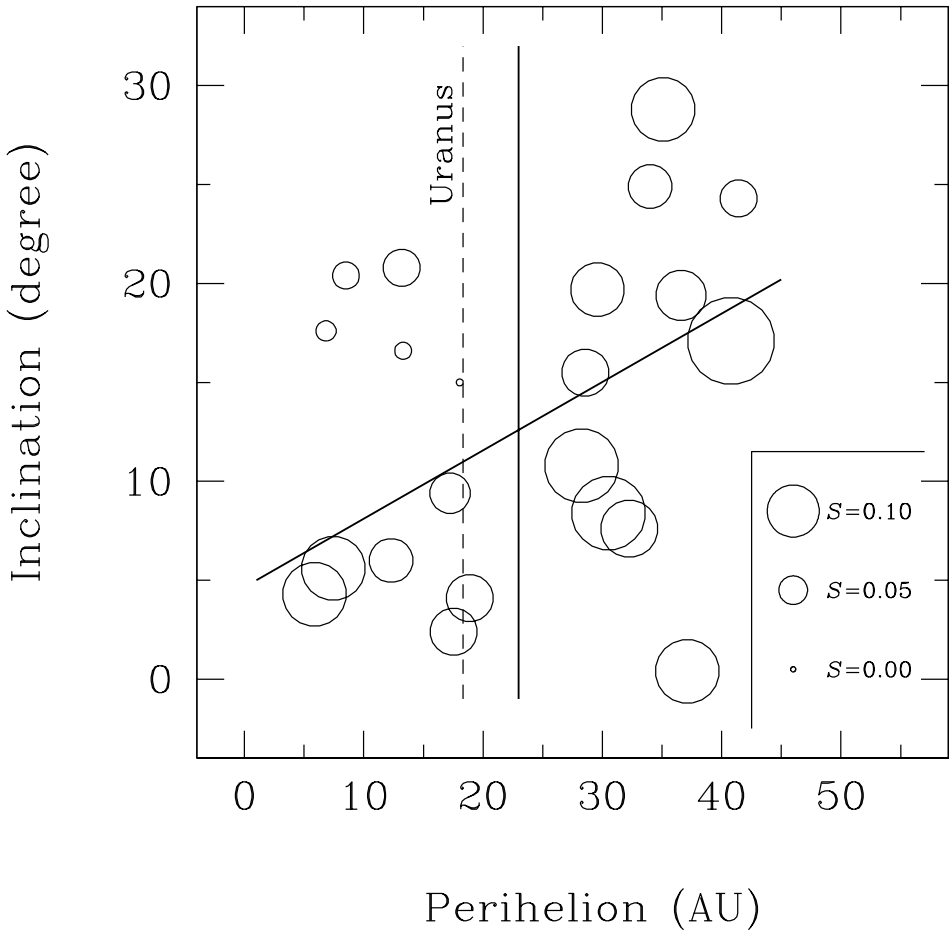

Figure 2.35: Perihelion–inclination distribution of Centaurs and TNOs. The size of circles indicate surge slope of the object. The sold lines are boundaries of the surge categories (see text). The dashed line shows the Uranus's perihelion.

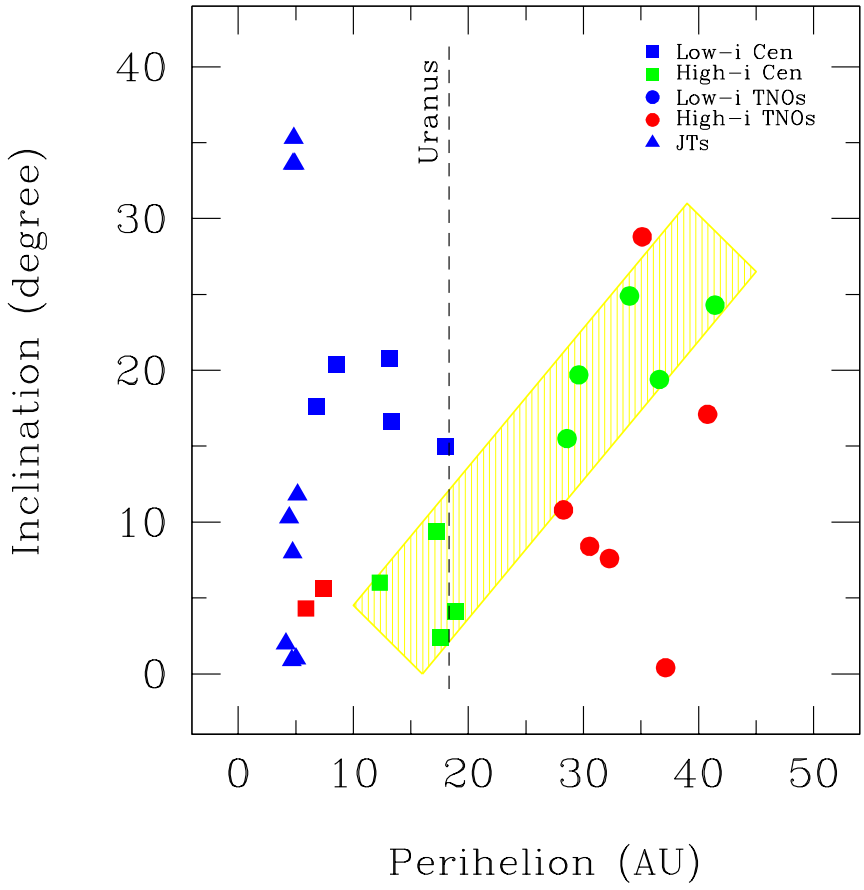

Figure 2.36: Perihelion–inclination distribution of Jovian Trojans (triangles), Centaurs (squares), and TNOs (circles). The blue, green, and red symbols represent the low-, mid-, and high-surge populations, respectively. The shaded region shows the clump area of the mid-surge objects. The dashed line shows the Uranus's perihelion.